

Spring 2013

# Experimental evaluation of a mixer-ejector hydrokinetic turbine at two open-water test sites and in a tow tank

Matthew Rowell

*University of New Hampshire, Durham*

Follow this and additional works at: <https://scholars.unh.edu/thesis>

---

## Recommended Citation

Rowell, Matthew, "Experimental evaluation of a mixer-ejector hydrokinetic turbine at two open-water test sites and in a tow tank" (2013). *Master's Theses and Capstones*. 776.  
<https://scholars.unh.edu/thesis/776>

This Thesis is brought to you for free and open access by the Student Scholarship at University of New Hampshire Scholars' Repository. It has been accepted for inclusion in Master's Theses and Capstones by an authorized administrator of University of New Hampshire Scholars' Repository. For more information, please contact [nicole.hentz@unh.edu](mailto:nicole.hentz@unh.edu).

**EXPERIMENTAL EVALUATION OF A MIXER-EJECTOR HYDROKINETIC  
TURBINE AT TWO OPEN-WATER TEST SITES AND IN A TOW TANK**

**BY**

**MATTHEW ROWELL**

**BSME, Clarkson University, 2003**

**THESIS**

**Submitted to the University of New Hampshire**

**in Partial Fulfillment of**

**the Requirements for the Degree of**

**Master of Science**

**in**

**Mechanical Engineering**

**May, 2013**

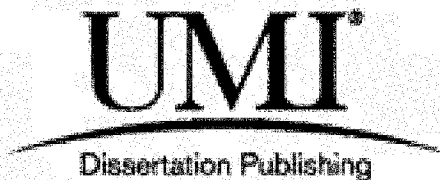
UMI Number: 1523778

All rights reserved

INFORMATION TO ALL USERS

The quality of this reproduction is dependent upon the quality of the copy submitted.

In the unlikely event that the author did not send a complete manuscript and there are missing pages, these will be noted. Also, if material had to be removed, a note will indicate the deletion.



UMI 1523778

Published by ProQuest LLC 2013. Copyright in the Dissertation held by the Author.

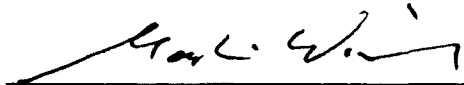
Microform Edition © ProQuest LLC.

All rights reserved. This work is protected against unauthorized copying under Title 17, United States Code.



ProQuest LLC  
789 East Eisenhower Parkway  
P.O. Box 1346  
Ann Arbor, MI 48106-1346

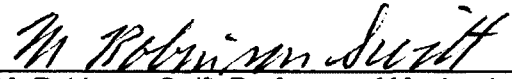
This thesis has been examined and approved.



Thesis Director, Martin M. Wosnik, Assistant  
Professor of Mechanical Engineering



Kenneth C. Baldwin, Professor of Mechanical  
Engineering and Ocean Engineering and  
Marine Sciences



M. Robinson Swift, Professor of Mechanical  
Engineering and Ocean Engineering



M. Werle, Founder and Senior Scientist  
FloDesign Wind Turbine Corp. (External  
Examiner)

22 Apr '13  
Date

## **Acknowledgments**

Hard work is made light by many hands. To everyone who contributed, financially or otherwise, to the successful performance of the open water testing I owe a great gratitude.

Special thanks to Dr. Martin Wosnik for tirelessly advising me and being fully willing to get his hands dirty. Thanks to FloDesign Wind Turbine Corp. and to the US Department of Energy, Water Power Program, for funding the project under an SBIR phase 2 grant. Thanks are due in particular to Jeff King, Jason Barnes, Dane Mealey, and Christian Gudmand for being a great team to work with. Thanks to Dr. Ken Baldwin and the rest of the faculty of Ocean Engineering for providing the necessary resources and guidance that was needed to accomplish this project. Thanks also to Dave Shay and the Marine Department for their trust and willingness to help from start to finish.

Thanks to my fellow students; Peter Bachant, Nathaniel Dufresne, Toby Dewhurst, Jeff Byrne, Steve Collister and Ivaylo Nedyalkov for all the help along the way. Lastly, a special thanks to my wife, Kathleen, for her unwavering support.

## Table of Contents

Acknowledgments .....	iii
Table of Contents .....	iv
List of tables .....	vi
List of Figures .....	vii
Abstract .....	xi
1 Introduction.....	1
1.1 History of Tidal Current Energy Conversion .....	3
1.2 Current State of Hydrokinetic Technology .....	4
1.3 Focus of Research .....	7
2 Fluid Kinetic Energy Conversion .....	9
2.1 One-Dimensional Momentum Theory.....	9
2.2 Increased Energy Conversion Techniques - Applying a Shroud .....	14
3 MEHT Testing Preparations .....	20
3.1 UNH-CORE Tidal Energy Test Site Tidal Current Analysis .....	20
3.2 Tidal Energy Test Platform Renovations .....	30
3.3 Tidal Energy Test Platform Instrumentation .....	33
3.4 Instrumentation Mounting Designs .....	38
4 Mixer-Ejector Hydrokinetic Turbine Testing.....	41
4.1 MEHT Testing Goals .....	42
4.2 Tow Testing.....	43
4.3 Deployments at the UNH-CORE Tidal Energy Test Site .....	45
4.4 Deployments at Muskeget Channel.....	60
4.5 Testing in the UNH Tow Tank .....	78
5 Materials Testing .....	96
5.1 Overview .....	96
5.2 Introduction to Corrosion .....	97
5.3 Introduction to Biofouling.....	99
5.4 Materials Testing Procedure.....	102
5.5 Materials Testing Results .....	105
5.6 Conclusions for Materials Corrosion and Biofouling Study .....	118
6 Project Summary and Conclusions .....	119
References .....	121
Appendix A .....	125

A.1 Detailed Renovations of UNH-CORE Tidal Energy Test Platform V.1....	125
A.2 Detailed Instrumentation on the UNH-CORE Tidal Energy Test Platform 137	
A.3 Detailed Instrumentation Mounting .....	144
A.4 Selected Test Platform Drawings .....	154
Appendix B .....	161
B.1 Safety Procedures for Open Water Testing .....	161

## List of tables

Table 1. Amplitude and phase values for tidal constituents used in Simply Currents predictions. Phase values obtained using single time origin with local standard time used for analysis and prediction (Boon, 2004b).....	26
Table 2. Deployment specifics and average nominal turbine performance at the UNH Tidal Energy Test Site. Note: power coefficient calculated using rotor area. ....	49
Table 3. Deployment specifics and average nominal turbine performance at the Muskeget Channel Test Site. Note: power coefficient calculated using rotor area. ....	68
Table 4. Inlet flow turbulence intensities for all MEHT tests. ....	74
Table 5. Tow tank MEHT testing tasks. ....	83
Table 6. Material selection for corrosion and biofouling study. ....	96
Table 7. Coupon deployment and recovery timeline.....	103
Table 8. Chemical cleaning instructions. (Taken from ASTM G1.03) .....	104
Table 9. Average mass loss and apparent corrosion rate for each material and coating.....	106
Table 10. Comparison of the four steel samples. ....	107
Table 11. Comparison of bare material to ePaint coatings after one year of submersion.....	109



## List of Figures

Figure 1. Examples of the four categories of hydrokinetic turbine research (clockwise from top left): axial, cross flow, ducted and oscillating. (Verdant, Ocean Renewable Power Company, Free Flow Power, Stingray) .....	4
Figure 2. FloDesign's Mixer-Ejector Hydrokinetic Turbine (MEHT). ( <i>Courtesy of FloDesign</i> ) .....	7
Figure 3. Representative control volume. After Manwell et al. (2009) .....	9
Figure 4. Power coefficient as a function of axial induction factor for an ideal horizontal axis turbine.....	13
Figure 5. Ideal flow through a shrouded turbine. (Taken from Hansen, 2008)....	14
Figure 6. Representative control volume. Adapted from Werle & Presz (2008).	16
Figure 7. Tide height variation over the course of a month (Taken from Boon, 2004a). .....	22
Figure 8. Pictorial example of the moon's effect on the tide when orbiting outside of earth's equatorial plane (Taken from Boon, 2004a).....	24
Figure 9. Combined effects of the three major varying components that influence tidal height over the course of one month (Taken from Boon, 2004a). .....	24
Figure 10. Current predictions and measured velocities for tests at the UNH-CORE Tidal Energy Test Site. NOAA predictions not available for 16 May.....	29
Figure 11. Streamlined rotating tripod, support structure and gantry crane on UNH-CORE's hydrokinetic turbine test platform v.1. ....	31
Figure 12. Rendering of UNH-CORE Tidal Energy Test Platform v1 with MEHT installed on tripod deployment frame. ....	32
Figure 13. Front view of test platform with depths of submerged instrumentation. ....	34
Figure 14. Hydrokinetic turbine test platform side view. ....	34
Figure 15. Tidal Energy Test Platform with MEHT at UNH-CORE Tidal Energy Test Site. ....	37
Figure 16. Test platform readied for testing in Muskeget Channel. ....	37
Figure 17. Video stills comparing GoPro Hero 2 (left) and SeaView (right). ....	38

Figure 18. Open-water tidal energy test sites in New England, UNH-CORE (NH) and Muskeget Channel (MA). .....	42
Figure 19. Enhanced twin bridled mooring configuration schematic (top) and view from test platform (bottom) at UNH-CORE Tidal Energy Test Site.....	48
Figure 20. Total mooring load on May 16 <sup>th</sup> (top) and May 17 <sup>th</sup> (bottom) at UNH Test Site. ....	51
Figure 21. Current velocity recorded on Vector ADV during testing at the UNH Tidal Energy Test Site. ....	52
Figure 22. Measured drag and calculated drag on May 17 <sup>th</sup> based on platform drag area of 0.62 m <sup>2</sup> .....	54
Figure 23. Normalized wake velocities at peak tidal flow at the UNH Tidal Energy Test Site. ....	56
Figure 24. Turbulence intensity in the wake of the MEHT. ....	59
Figure 25. Chart of Muskeget Channel with tidal energy resource outlined ( <a href="http://www.mrec.umassd.edu">www.mrec.umassd.edu</a> ).....	61
Figure 26. Test platform mooring configuration used for Muskeget Channel deployments(Dewhurst, 2013).....	65
Figure 27. Total platform mooring load at Muskeget Channel. ....	70
Figure 28. Tidal current velocity from MEHT testing at Muskeget Channel. ....	71
Figure 29. Calculated drag load based on drag area and tidal current compared to measure drag load.....	73
Figure 30. Wake velocities in Muskeget Channel.....	75
Figure 31. Tidal current (top right) mooring load (top left) and analytical model mooring load results (bottom) at Muskeget Channel on July 16, 2012 (Sea State 2+). ....	77
Figure 32. Installing the tow frame to the carriage at the UNH Tow and Wave Tank. ....	79
Figure 33. MEHT Mounted in UNH tow tank hydrokinetic turbine test frame.....	80
Figure 34. MEHT configuration in UNH tow tank for free stream ADV measurements.....	81
Figure 35. Tow tank wake traversing rig at 4D downstream.....	82

Figure 36. Tow tank wake profiles. ....	84
Figure 37. All tow tank wake profiles. ....	85
Figure 38. Half wake X, Y, Z velocity at 0.167 shroud diameters downstream. .	86
Figure 39. Full wake X, Y, Z velocity at 2 diameters downstream. ....	86
Figure 40. Wake comparison of MEHT Rotor-only operating at optimal tip speed ratio between May 16 <sup>th</sup> (UNH Test Site) and July 19 <sup>th</sup> (Muskeget Channel) at 2D (top), 4D (middle) and 6D (bottom) downstream. ....	89
Figure 41. Wake comparison of MEHT Stator-Rotor operating at optimal tip speed ratio between May 15 <sup>th</sup> (UNH Test Site) and tow tank at 2D (top) and 4D (bottom) downstream.....	90
Figure 42. MEHT yawed drag, rotor loaded v. rotor unloaded.....	91
Figure 43. Drag coefficients for yawed rotor loaded turbine. ....	93
Figure 44. MEHT with rudder.....	94
Figure 45. Yaw torque with and without rudder. ....	94
Figure 46. Coupon geometry. ....	102
Figure 47. Coupon test frame, 1 of 4, prior to seawater submersion.....	103
Figure 48. Panel “A” coupon mass over 1 year measured initially and quarterly thereafter. ....	106
Figure 49. Comparison of EN plated steel (left) to untreated steel (right) after one year of submerged exposure (from panel A). ....	110
Figure 50. Bare aluminum (left) and anodized aluminum (right) after one year of submerged exposure (from panel A). ....	111
Figure 51. Stainless steel coupons after one year of exposure (Panels A through D from left to right). ....	111
Figure 52. Panel A coupons after recovery, prior to cleaning, in July (top), October (middle) and January (bottom). ....	113
Figure 53. Panel A coupon biomass accumulation without sediment to show growth accumulation over each quarter.....	114
Figure 54. Compounding effects of biomass accumulation by comparison of panel A (cleaned quarterly) to undisturbed panels C in October and D in January. ....	115

Figure 55. Initial recovery of panel C (October) compared to initial recovery of panel D (January) showing natural reduction in biomass in colder months. ....	116
Figure 56. Biomass accumulation per panel for each recovery. (Scale changed per plot for clarity).....	117
Figure 57. UNH-CORE Tidal Energy Test Platform v1 prior to modifications. ...	125
Figure 58. UNH-CORE Tidal Energy Test Platform v1 and support vessel after modifications.....	126
Figure 59. Turbine deployment structure.....	127
Figure 60. Clasp to lock the turbine and frame in the deployed position. ....	128
Figure 61. Hoist mounted on gantry crane. ....	129
Figure 62. Aft platform model. ....	130
Figure 63. Pontoon stringer layout post overhaul. ....	132
Figure 64. Platform after overhaul prior to launch.....	136
Figure 65 NREL instrumentation enclosure and Hemisphere GPS. ....	141
Figure 66 Camera mounting locations for MEHT monitoring during testing. ...	143
Figure 67. Version 1 of the traversing ADV sting design. ....	144
Figure 68. Rotating streamlined foil prepared for deployment. ....	145
Figure 69. The version 2 ADV sting mounting design.....	146
Figure 70. Version 2 ADV traversing assembly. ....	147
Figure 71 Stream wise rail and traversing mechanism cantilevered off the stern of the test platform. ....	149
Figure 72. ADCP mount on bow of test platform. ....	151
Figure 73. Vector mounted to bow of test platform.....	152
Figure 74 Vector and other instruments mounted to the bow of the test platform. ....	153

Abstract

EXPERIMENTAL EVALUATION OF MIXER-EJECTOR HYDROKINETIC  
TURBINE AT TWO OPEN-WATER TEST SITES AND IN A TOW TANK

by

Matthew Rowell

University of New Hampshire, May, 2013

For marine hydrokinetic energy to become viable it is essential to develop energy conversion devices that extract energy with high efficiency, and to field-test them in an environment similar to the one in which they are designed to eventually operate. FloDesign Inc., with FloDesign Wind Turbine Corp., developed a Mixer-Ejector Hydrokinetic Turbine (MEHT) that encloses the turbine in a specially designed shroud to increase mass flow through the turbine rotor.

A scaled version of this turbine was evaluated experimentally at two open-water tidal energy test sites, and in a tow tank. State-of-the-art instrumentation was used to measure free stream and wake velocities, turbine power extraction, test platform loadings and platform motion induced by sea state. The MEHT was able to generate power from tidal currents over a wide range of conditions, with low-velocity start-up. The decay of the wake velocity deficit was found to improve with increasing free stream turbulence.

## 1 Introduction

The consumption of primary energy in the United States (US) has climbed consistently, with periodic relatively minor dips, since 1950 reaching approximately 100 quadrillion BTU (quad) per year ( $\approx 10$  kW average consumption of primary energy per capita) in 2011 (United States Department of Energy (DOE), 2012). Despite the fact that between 2009 and 2011 the contribution from renewable energy grew by 1.4 quad in the US, fossil fuels still account for close to 82% of the primary energy consumption. (DOE, 2012). The projected date of depletion of fossil fuels is highly debated, but both sides agree that they are a finite resource (McKay, 2009). In addition to the security of supply, there is scientific concern that the release of carbon dioxide from burning fossil fuels is changing the environment. For some developed nations, including the US, the long term trend of increasing dependence on foreign supply has the potential to lead to political instabilities (McKay, 2009) (DOE, 2012) (Chambers, 2011). These reasons, among others, are motivating engineers and scientists to advance renewable energy conversion technologies.

Of the approximately 100 quad of primary energy consumed in the US in 2011, 40 quad was dedicated to electrical energy production (DOE, 2012). Due to conversion losses, plant use and transmission and distribution losses, the net generation of electrical energy was approximately one third of this, or 4,100 terawatt-hours (TWh) ( $\approx 1.5$  kW average consumption of *electrical* power per capita) (DOE, 2012). Electricity generated from wind contributed 120 TWh in 2011, up from 17.8 TWh in 2005, and 5.6 TWh in 2000. There is no contribution

from ocean wave energy converters (OWEC) or tidal in stream energy converters (TISEC) yet because they have not been developed and installed at grid scale within the US. First pilot-scale projects in the US (100s of kW) are about to be connected to the grid, e.g. Verdant Power (East River, New York) and Ocean Renewable Power Company (Cobscook Bay, Maine) (FERC, 2012) (ORPC, 2012).

With an estimated 400 terawatt-hours per year (TWh/yr) available in the US to be harnessed from tidal current and waves combined it can be expected that the technology will advance so that these devices will contribute to the US supply (Bedard *et.al*, 2007). A recent study (Haas et al. 2011) generated a database of tidal energy resources on the US coasts.

Five select tidal current sites in the US are estimated to have an available resource of 6.6 TWh/yr (Bedard *et.al*, 2007). Tidal in-stream energy conversion devices convert the kinetic energy of tide induced currents into usable, mainly electric, energy. Like some other renewable energy resources (e.g. wind and solar), tidal current energy is intermittent, yet unlike most others, it is quite predictable based on an understanding of the celestial gravitational effects on the earth's oceans (Bedard *et.al*, 2007) (Boon, 2004a). The following study is an investigation into the performance of one particular in-stream hydrokinetic energy converting technology at two tidal energy test sites and in a tow tank, and ancillary measurements of the tidal energy resource, device wake, mooring loads, etc.

## **1.1 History of Tidal Current Energy Conversion**

The conversion of the kinetic energy in moving water into mechanical work can be dated to a ten-volume Roman engineering treatise by Vitruvius in the Augustan Age (31 BC to AD 14) where water wheels are described as being used for milling operations (Hardisty, 2009). Three main varieties of turbines were developed and used through the classical age: the Norse, the undershot, and the overshot water wheel (Hansen, 2007). The complexity and efficiency of the turbines improved with time and by the 12<sup>th</sup> century the tidal barrage and impoundment concepts were developed to increase the available net head by damming rivers or tidal basins (Hansen, 2007). These devices evolved into the hydroelectric stations that are used to this day which now account for 35% of the renewable energy produced in the US (DOE, 2012). Damming rivers has received negative attention due to environmental impacts on the surrounding land and fisheries which advocates suggest can be circumvented by in-stream hydrokinetic devices (Cada *et al.*, 2007).

The ongoing research in hydrokinetic energy conversion technologies falls under four main categories of turbines: axial, cross flow, flow augmented and oscillating. Axial devices have their axis of rotation parallel to the flow, whereas the cross flow devices have their axis of rotation perpendicular to the flow. Flow augmented devices utilize a shroud or duct to increase the mass flow across a rotor and can be implemented on either cross flow or axial devices. The oscillating devices typically do not have a rotating component but rather use hydrofoils, cylinders or other shapes that move up and down, or side to side, in



an oncoming flow, either via actuation of a control surface (hydrofoil) or the asymmetric shedding of vortices. Power is typically extracted from oscillating devices by operating a hydraulic pump or linear generator.

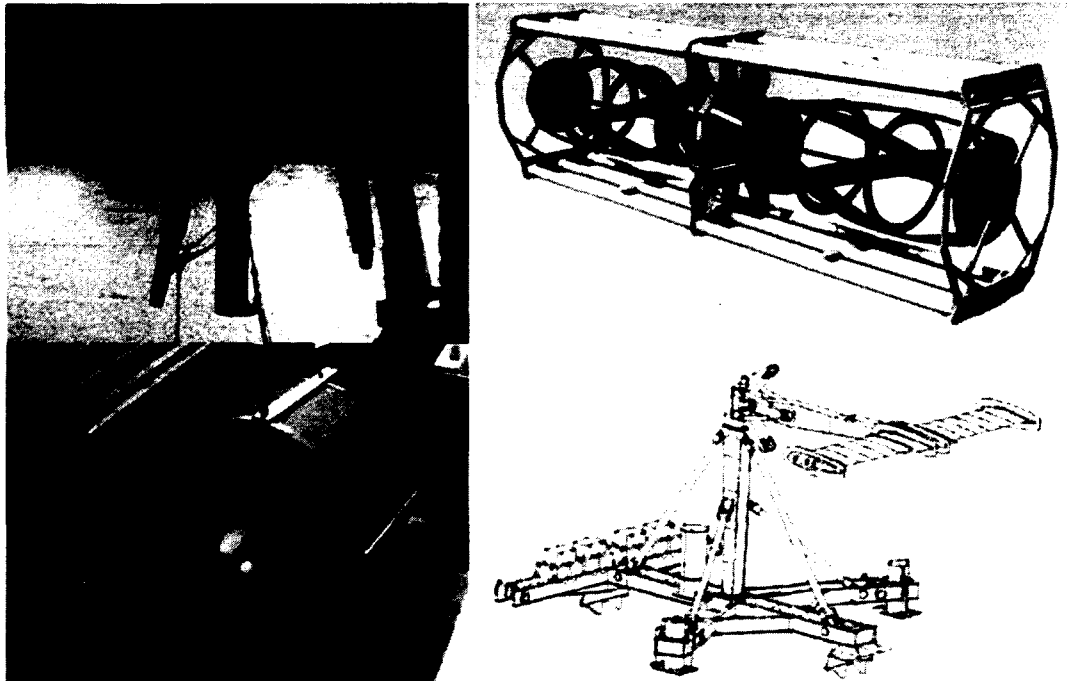


**Figure 1. Examples of the four categories of hydrokinetic turbine research (clockwise from top left): axial, cross flow, ducted and oscillating. (Verdant, Ocean Renewable Power Company, Free Flow Power, Stingray)**

## **1.2 Current State of Hydrokinetic Technology**

The power available from flowing fluid is proportional to the water velocity cubed. Therefore, sites with relatively high velocity flows are most desirable for development based strictly on power density. For a site to be considered a prime location for development it can be expected to have a minimum average power density of  $1\text{kW/m}^2$  which roughly correlates to peak tidal velocities of approximately 3 m/s, or 6 knots (Bedard *et al.* 2006) (Polagye *et al.* 2010). There are several such sites in the US that meet this requirement in Maine, New York,

Washington, California and Alaska (Bedard, 2007). Worldwide there are many more locations that meet these criteria in Canada, Ireland, Scotland, Korea, Australia, New Zealand and more (Hardisty, 2009). Some sites that are at the forefront of development with hardware in the water are Marine Current Turbine's (MCT) SeaGen installation in the Strangford Lough in Ireland, Ocean Renewable Power Company's (ORPC) projected installation of cross flow turbines in Cobscook Bay, ME, Verdant Power's installation of an array of turbines in the East River in NY, and Korea Ocean Research and Development Institute's (KORDI) installation of Gorlov Helical Turbines in Uldulmok Strait.

As is the case in wind turbine development, the majority of designers are focused on axial devices. These turbines have rotors with predominantly lift-driven blades that turn the linear flow of water into rotary motion of a shaft. Of the projects listed above, SeaGen uses a two bladed pitch-controlled rotor design, and Verdant uses a 3 bladed fixed-pitch, passively yawing rotor design. Complexities of design enhancement lie in blade shape design, material choices, reducing gear box frictional losses, mechanical to electrical energy conversion, installation methods (e.g. bottom-mounted or moored) and more.

The design of cross flow turbines originated from the Darrieus wind turbines first developed and patented in 1931, with a shape reminiscent of egg beaters (Darrieus, 1931). Cross-flow axis turbines can either be positioned vertically or horizontally in a tidal flow. ORPC's device being installed in Cobscook Bay is an example of a horizontal axis cross flow turbine. An advantage of this design is that no yawing mechanism is needed because any

flow perpendicular to the turbine axis will induce lift causing rotation. This is especially valuable in tidal flows due to the reversal of flow approximately every 6 hours.

Several developers, including FloDesign, have devised flow augmenting designs to try to increase the incident power over a given cross sectional area. Free Flow Power developed a fully shrouded axial device whereas FloDesign shrouded the blades and focused on downstream wake mixing enhancements.

Lastly, the oscillating devices are receiving somewhat less attention but the designs are still practical for some applications. The Stingray is an example of such device that uses a single foil that changes angle as it oscillates up and down. As the angle of the blade changes, so too does the angle of attack of the incident flow resulting in the lift force alternating direction. Other alternatives (e.g. VIVACE by Vortex Hydro Energy) utilize the natural asymmetric shedding of vortices over cylinders in cross-flow to induce oscillatory motion. Such motion can be used to drive a pump that pressurizes a fluid to run a generator, or to serve other applications.

### 1.3 Focus of Research

FloDesign Inc. in collaboration with FloDesign Wind Turbine Corp., Turbo Solutions, Alden Research Laboratories (Alden), and the University of New Hampshire (UNH) under a Small Business Innovation Research (SBIR) Phase II grant from the Department of Energy (DOE),

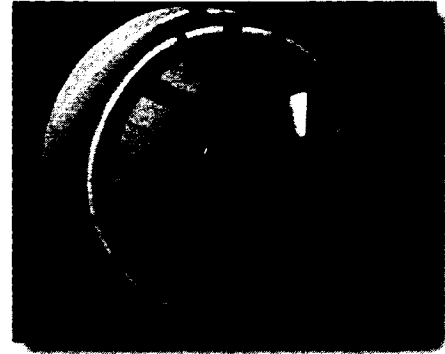


**Figure 2. FloDesign's Mixer-Ejector Hydrokinetic Turbine (MEHT). (Courtesy of FloDesign)**

designed and tested a Mixer-Ejector Hydrokinetic Turbine (MEHT). Prior to delivery of the prototype to UNH, FloDesign designed and built the turbine, designed, built and calibrated the generator, and tested the turbine in a flume at Alden. The initial test plan proposed shake-down testing in the UNH tow tank prior to the open-water deployments, with wake measurements and a study of the effects of inlet turbulence and off axis inlet flow. Due to the turbine testing time line, and tow tank renovation at UNH, this phase of testing was conducted after testing at the two tidal energy test sites. Therefore, testing at UNH commenced with open water tow testing using UNH-CORE's 35 foot hydrokinetic test platform towed by a 22 foot UNH-owned Eastern workboat. This phase of testing involved instrumentation shakedown and a functionality check of the newly installed turbine deployment mechanism. Following tow testing, the platform was transported to the UNH-CORE Tidal Energy Test Site, a sheltered site at a narrows in Great Bay Estuary in the Piscataqua River at the General Sullivan Bridge (GSB). Testing at this location involved mooring the platform with

the turbine deployed for single flood tidal events while measuring inlet velocity, turbine performance, turbine wake, and other parameters. Three tests at this location were accomplished over the course of one week. The last phase of testing was a deployment at an open water test site in Muskeget Channel between Martha's Vineyard and Nantucket in Massachusetts. The test platform and the turbine were transported to Massachusetts and a larger work vessel was contracted by the Massachusetts Marine Renewable Energy Center (MREC) for a week long test. With deployments subject to wind and waves, three single tidal cycle deployments were accomplished at this site during one week.

This thesis reports on the work performed at UNH in connection with the scale model testing of the FloDesign Mixer-Ejector Hydrokinetic Turbine. Some site analysis was performed prior to deploying at the UNH-CORE Tidal Energy Test Site, and significant work was required to make the test platform capable of meeting the testing requirements, including the design and fabrication of a turbine deployment mechanism and instrumentation mounts. Inflow and wake velocity data were collected with different instruments and analyzed. Lastly, in parallel to the turbine testing program, a materials study was performed over the course of 12 months at the UNH Pier (New Castle, NH) to assist in material and coating selection for the next stage of development for this hydrokinetic turbine.

## 2 Fluid Kinetic Energy Conversion

To understand the principles of augmented, ducted hydrokinetic turbines some principles of un-ducted systems must be presented. An appropriate starting point for theoretical analysis is one-dimensional momentum theory, or actuator disc theory, developed by Albert Betz in 1919 (Betz 1920, Manwell *et al.*, 2009; Hansen, 2008).

### 2.1 One-Dimensional Momentum Theory

One-dimensional momentum theory requires that the rotor of an in-stream device be approximated as an infinitesimally thin actuator disc that creates a discontinuity of pressure inside a control volume as shown in Figure 3 (Manwell *et al.*, 2009).

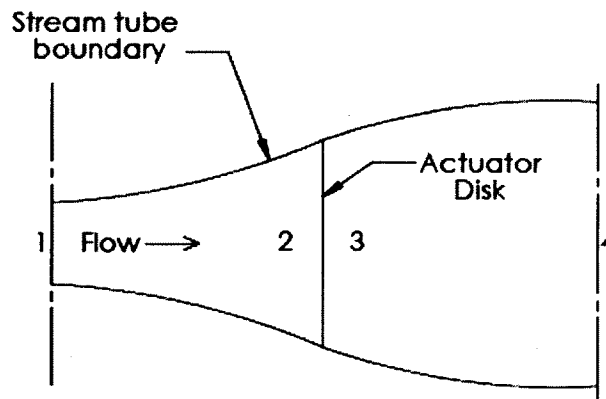


Figure 3. Representative control volume. After Manwell *et al.* (2009)

A streamtube is conceptually a collection of streamlines which allow no fluid to cross the boundary and the fluid properties are assumed constant along the cross section within those boundaries (Panton, 2005). This definition allows the application of conservation of mass and momentum at different locations

within the streamtube. Assuming a steady, incompressible flow, the thrust on the turbine, or actuator disc,  $F_T$ , is equal to the change in momentum of the stream between the upstream (1) and downstream (4) boundaries of the streamtube.

$$F_T = U_1(\rho A_1 U_1) - U_4(\rho A_4 U_4), \quad (2.1)$$

Note that the integral of the pressure acting on the control volume shown in Figure 3 also has a small contribution to the force balance in the streamwise direction (Hansen, 2008), which is neglected here. Sorensen/Mikkelsen report that the neglected force could be as large as 5% of the thrust force (Sorensen, 2011).

By further applying the conservation of mass,

$$\dot{m} = \rho A_1 U_1 = \rho A_4 U_4 \quad (2.2)$$

equation (2.1) can be rearranged to

$$F_T = \dot{m}(U_1 - U_4). \quad (2.3)$$

The change in momentum of the stream is wholly attributed to the discontinuity of pressure imparted by the actuator disc. The pressure change across the disc can be found by applying Bernoulli's equation to the volumes upstream and downstream of the actuator disc within the streamtube. Bernoulli's equation is derived from the inviscid Navier-Stokes equations (Euler Equations) and can be applied to any streamline where flow is steady, incompressible and inviscid (e.g. between any cross sections of the streamtube, but not across the actuator disc) (Panton, 2005). Applying Bernoulli's equation provides

$$P_1 + \frac{1}{2}\rho U_1^2 = P_2 + \frac{1}{2}\rho U_2^2 \quad (2.4)$$

and

$$P_3 + \frac{1}{2}\rho U_3^2 = P_4 + \frac{1}{2}\rho U_4^2. \quad (2.5)$$

By solving for and subtracting  $P_3$  from  $P_2$ , assuming static downstream pressure returns to free stream pressure and recognizing that  $U_2$  equals  $U_3$ , the following relationship can be obtained.

$$P_2 - P_3 = \frac{1}{2}\rho(U_1^2 - U_4^2) \quad (2.6)$$

A new expression for the thrust force can be written as the change of pressure at the rotor plane

$$F_T = A_2(P_2 - P_3) \quad (2.7)$$

and combined with equation (2.6) and equated to (2.3),

$$F_T = \frac{1}{2}\rho A_2(U_1^2 - U_4^2) = \dot{m}(U_1 - U_4). \quad (2.8)$$

By defining the axial induction factor as the fractional decrease of velocity between the free stream and the actuator ( $a = \frac{U_1 - U_2}{U_1}$ ) the velocity at the actuator can be solved

$$U_2 = U_1(1 - a). \quad (2.9)$$

Solving for the wake velocity from  $U_2 = \frac{U_1 + U_4}{2}$  and the axial induction factor provides

$$U_4 = U_1(1 - 2a). \quad (2.10)$$

The power out of the system ( $P_w$ ) will be the thrust force times the velocity of the fluid at the point of power extraction, written as:

$$P_w = F_T * U_2 = \frac{1}{2}\rho A_2(U_1^2 - U_4^2)U_2 \quad (2.11)$$

By substituting the solutions for  $U_2$  and  $U_4$ , the power can be written in terms of free stream velocity ( $U$ ) and the axial induction factor ( $a$ ) as:



$$P_w = \frac{1}{2} \rho A_2 U_2^3 4a(1-a)^2 \quad (2.12)$$

The power coefficient is a non-dimensional term determined by dividing the power extracted by the maximum available power based on free stream velocity, the result is shown in Figure 4.

$$C_p = \frac{\frac{1}{2} \rho A_2 U_2^3 4a(1-a)^2}{\frac{1}{2} \rho A_2 U_2^3} = 4a(1-a)^2 \quad (2.13)$$

The maximum value for the coefficient of power is found by setting the derivative with respect to the axial induction factor equal to zero and then substituting that value back into the expression.

$$C_p = 4a^3 - 8a^2 + 4a \quad (2.14)$$

$$\frac{dC_p}{da} = 12a^2 - 16a + 4 \quad (2.15)$$

The values of  $a$  for which the power coefficient has a maximum are found from the roots of the resulting quadratic equation shown in equation 2.15. They are 1, corresponding to a stalled disc condition, and 1/3. Therefore, the value of the axial induction factor for which  $C_p$  reaches a maximum is 1/3, which, when substituted back into the  $C_p$  equation, yields:

$$C_p = \frac{4}{3} \left(1 - \frac{1}{3}\right)^2 = \frac{16}{27} = 0.593. \quad (2.16)$$

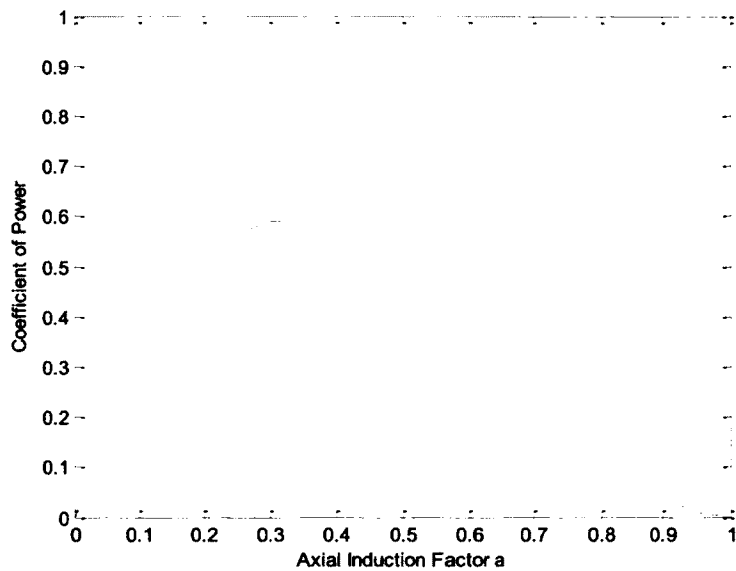


**Figure 4. Power coefficient as a function of axial induction factor for an ideal horizontal axis turbine.**

This application of first principles to a simple system shows that an optimal turbine is limited to extracting 59.3% of the energy available in a free stream flow and is referred to as the Betz limit (Manwell et al., 2009). Note that this limit was also independently derived by Lanchester around the same time (Bergey, 1979). Other factors such as wake rotation, tip losses and friction will continue to limit the amount of power available for extraction in the form of electrical energy (Hansen, 2008).

This implied limit to power extraction has inspired engineers to try building devices to reach the limit, and also try to find situations where the limit may not apply. In 2008, Hansen published a straightforward justification for ducting a turbine to increase power yield.

## 2.2 Increased Energy Conversion Techniques - Applying a Shroud

A proposed mechanism for enhancing turbine performance by funneling flow and reducing tip losses is to shroud the rotor with a foil shaped duct. With the cross section of the shroud in the shape of an airfoil, the generated cylindrical lift induces a ring vortex at the entrance of the turbine. The greater the lift, the more fluid will be drawn into the turbine limited by boundary layer separation along the wall of the diffuser. (Hansen, 2008).

### 2.2.1 Ducted Turbines: Velocity Augmentation Factor (Hansen, 2008)

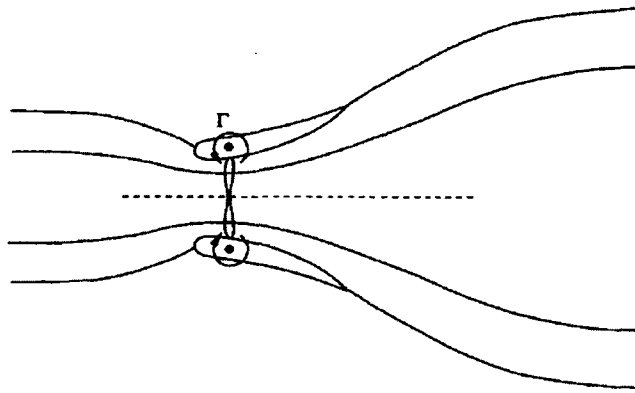


Figure 5. Ideal flow through a shrouded turbine. (Taken from Hansen, 2008)

Figure 5 is a stream tube for the suggested ducted device with a cross sectional view of the shroud embodying the rotor intended to force the free stream flow into the duct and to accelerate it through the area of the rotor plane. After the rotor extracts the energy the moving fluid it is then diffused to the free stream flow downstream of the rotor. As stated earlier, the coefficient of power is the ratio of power out to power available in the free stream.

$$C_{p,d} = \frac{P_{W_{out}}}{P_{W_{avail}}} = \frac{P_{W_{out}}}{\frac{1}{2}\rho U_0^3 A} \quad (2.17)$$

By defining  $U_2$  as the axial velocity at the rotor plane,  $P_{out}$  in terms of thrust (T) and local velocity ( $U_2$ ) is

$$C_{p,d} = \frac{P_{W_{out}}}{\frac{1}{2}\rho U_0^3 A} = \frac{T * U_2}{\frac{1}{2}\rho U_0^2 \frac{U_0}{U_2} U_2 A} = C_T \varepsilon \quad (2.18)$$

where  $\varepsilon$  is introduced as the velocity augmentation factor ( $U_2/U_0$ ) and  $C_T$  is the coefficient of thrust for the ducted turbine,

$$C_T = \frac{T}{\frac{1}{2}\rho U_0^2 A} \quad (2.19)$$

For an ideal bare turbine the following is true (Hansen, 2008),

$$C_{p,b} = C_T(1 - a) \quad (2.20)$$

where  $a$  is the previously defined axial induction factor.

The ratio of power coefficients of a ducted turbine to a bare turbine is

$$\frac{C_{p,d}}{C_{p,b}} = \frac{\varepsilon}{(1 - a)} \quad (2.21)$$

The mass flow rate through ducted and bare turbines, respectively is

$$\dot{m}_d = \rho A U_2 \quad (2.22)$$

$$\dot{m}_b = \rho A U_0 (1 - a). \quad (2.23)$$

Dividing both mass flow rate equations by  $\rho A V_0$  will result in the mass flow rate ratio equal to the power coefficient ratio:

$$\frac{C_{p,d}}{C_{p,b}} = \frac{\dot{m}_d}{\dot{m}_b} \quad (2.24)$$

Therefore, if the shroud can effectively increase the mass flow rate across the rotor the power will increase proportionally. Several challenges exist in maximizing mass flow rate through a duct, one of which being able to maintain the boundary layer attachment along the length of the shroud (Gilbert, 1983).

### 2.2.2 Ducted Turbine: Shroud Coefficient (Werle and Presz, 2008)

An approach similar to the Betz derivation can be applied to a ducted turbine in a manner that implies the Betz limit may not apply to such devices. The following is re-derived from Werle and Presz, 2008.

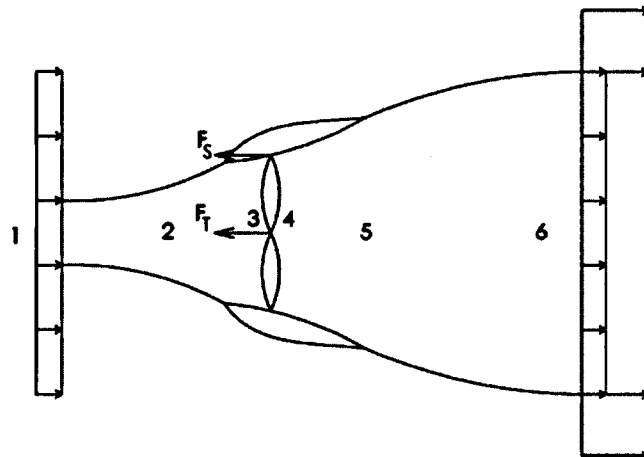


Figure 6. Representative control volume. Adapted from Werle & Presz (2008)

Figure 6 is the stream tube where location 1 has free stream conditions, 2 is just prior to shroud entrance, 3 is upstream of the actuator disc used to simulate the turbine rotor, 4 is just downstream of the actuator disc, 5 is the duct exit and 6 is far downstream. The thrust force is the force that is imparted on the actuator in the case of a turbine, or the force that is exerted onto the fluid in the case of a propeller.

$$F_t = A_3(P_3 - P_4) \quad (2.25)$$

The shroud force is an axial force that occurs on the shroud as the result of expanding or contraction streamlines caused by the propeller's interaction with the fluid. It is defined as

$$F_s = F_t C_s \quad (2.26)$$

where  $C_s$  is an experimentally found, design specific shroud coefficient. Summing the axial forces

$$\sum F_x = F_t + F_s = F_t(1 + C_s) = (1 + C_s)(P_3 - P_4)A_3 \quad (2.27)$$

Applying the conservation of linear momentum to the control volume, the total axial force is equal to the rate of change of momentum of the air stream,

$$(1 + C_s)(P_3 - P_4)A_3 = \rho A_3 U_3 (U_1 - U_6) \quad (2.28)$$

The pressure change across the rotor plane can be solved using Bernoulli's equation. Bernoulli's equation is obtained by integrating the Euler equations (the Navier-Stokes equation neglecting viscous terms) between two points along a streamline, thus it represents conservation of mechanical energy. For steady state and incompressible flow, equating the energy on either side of the rotor plane produces

$$P_1 + \frac{1}{2}\rho U_1^2 = P_3 + \frac{1}{2}\rho U_3^2 \quad (2.29)$$

$$P_4 + \frac{1}{2}\rho U_4^2 = P_6 + \frac{1}{2}\rho U_6^2 \quad (2.30)$$

Since the area does not change across the rotor plane the conservation of mass dictates that the extraction (or insertion) of energy is by pressure change only thus,  $u_3 = u_4$ . Since  $P_6$  was chosen to be far downstream it will be assumed

that the pressure has returned to free stream thus  $P_1 = P_6$ . Now 2.29 and 2.30 can be solved to

$$P_3 - P_4 = \frac{1}{2}\rho(U_1^2 - U_6^2) \quad (2.31)$$

Substituting 2.31 into 2.28

$$\frac{1}{2}\rho A_3(1 + C_s)(U_1^2 - U_6^2) = \rho A_3 U_3(U_1 - U_6) \quad (2.32)$$

solving for  $u_3$

$$U_3 = \frac{1}{2}(1 + C_s)(U_1 + U_6) \quad (2.33)$$

Now an expression for the power transfer at the rotor plane can be expressed as

$$P_W = F_t U_3 = U_3 A_3 (P_3 - P_4) = U_3 \frac{1}{2} \rho A_3 (U_1^2 - U_6^2) \quad (2.34)$$

Substituting in 2.33 into 2.34

$$P_W = \frac{1}{4} \rho A_3 (1 + C_s) (U_1^3 + U_6 U_1^2 - U_1 U_6^2 - U_6^3) \quad (2.35)$$

Differentiating P with respect to the downstream velocity and setting equal to zero results in the (physical) solution

$$U_6 = \frac{1}{3} U_1 \quad (2.36)$$

Substituting the maximum downstream velocity back into the power equation yields:

$$P_{W_{max}} = \frac{16}{27} (1 + C_s) \frac{1}{2} \rho A_3 U_1^3. \quad (2.37)$$

Therefore the maximum coefficient of power is

$$C_{P_{max}} = \frac{16}{27} (1 + C_s) \quad (2.38)$$

It is worthy to note that without a shroud the shroud coefficient will equal zero and the maximum power coefficient will equal the previously derived 59%. This derivation explains why there is interest in exploring the use of shrouded devices. Werle and Presz (2009) extended the analysis of Werle and Presz (2008) to low-speed power extraction systems that employ both a shroud and an ejector. The design of the MEHT is based on Werle and Presz (2009).

Lastly, it can be argued that the power available should be calculated from the shroud diameter rather than the rotor diameter since the device can theoretically divert the flow from the larger area to the smaller rotor area. Doing so would result in a ratio of areas in the final maximum power coefficient result.



### **3 MEHT Testing Preparations**

While FloDesign was fabricating and testing their turbine in the spring of 2011 a significant amount of time was spent at UNH-CORE preparing for the deployments. First, data collected by the National Ocean Service (NOS) of the National Oceanographic and Atmospheric Administration (NOAA) were used to predict tidal current velocities throughout the tidal cycle at the UNH-CORE General Sullivan Bridge test site. NOAA only publishes maximum current predictions, not the ramp-up and ramp-down, which are important for tidal turbine deployments. Then the UNH-CORE Tidal Energy Test Platform v1, a 35 foot (10.7m) long, 10 foot (3.0m) wide pontoon boat dedicated to MHK turbine testing, was completely renovated, and a new turbine deployment mechanism, instrumentation mounts and wake traversing mechanism were installed.

#### **3.1 UNH-CORE Tidal Energy Test Site Tidal Current Analysis**

From July through September 2007 NOAA/NOS conducted a survey of the tidal currents in the Piscataqua River, including at the UNH-CORE Tidal Energy Test Site at General Sullivan Bridge (Davis, 2007). Data were collected with a bottom deployed Acoustic Doppler Current Profiler (ADCP) at the UNH test site. After collecting and analyzing the data, NOAA published the predicted maximum ebb and flood velocities as well as the time associated with them and the time of slack water. The predictions and the raw data are available on their website in the public domain (<http://co-ops.nos.noaa.gov/>).

Many factors contribute to the tidal current velocities including celestial effects imparting gravitational forces, as well as geographic and bathymetric

factors. Therefore, the curve of velocity versus time connecting the maximum flood and ebb tidal current velocities is rarely smooth and purely sinusoidal (Boon, 2004a). The MEHT test plan included tests during ramp up and at peak velocity so it was important to know beforehand the rate of change of velocity and the length of time available for testing at peak flow conditions. Determining this curve is made possible by applying a harmonic analysis method of least squares (HAMELS) to the raw ADCP data collected at the test site to determine and apply the driving celestial harmonic constituents.

### 3.1.1 Overview of Tides and Currents

Tides are driven by celestial gravitational interactions with earth, and currents in coastal regions are in large part driven by those tides. The moon accounts for approximately two thirds of the tide forcing, while the sun accounts for approximately the other one third (Boon, 2004a). Meteorological effects also play an important role in tides and tidal currents, but are far more difficult to predict, especially far into the future (Boon, 2004a).

The gravitational force between celestial bodies is given by

$$F = G \frac{M_1 M_2}{R^2} \quad (3.1)$$

where G is the gravitational constant, M refers to the masses of each body, and R is the distance between the two bodies. The gravitational forces from all influencing celestial bodies yields resultant tractive forces on the oceans that act parallel to the surface of the ocean, and are responsible for the movement of the water as the celestial bodies move in relation to one another.

Given that there can be several compounding forces that lead to the resultant tractive force and thus the motion of the tide, the tidal height changes with several factors (Boon, 2004a). The most pronounced of these changes occurs with differing sun-moon relations. When the sun, earth, and moon are all aligned, the gravitational forces are added which yield tides of greater range, and are called spring tides. When the sun, earth and moon are aligned such that the moon and sun form a 90 degree angle with the Earth, tides of lesser range are formed named neap tides. The sequence of these two tides of varying heights is called the spring-neap cycle.

The next most influential cause of variation in tidal height has to do with the elliptic nature of orbits within the solar system. As the earth rotates around the sun, there are times when it is closer to the sun, at the midpoint of the ellipse, and times when it is further, at the tips of the ellipse. The same applies for the

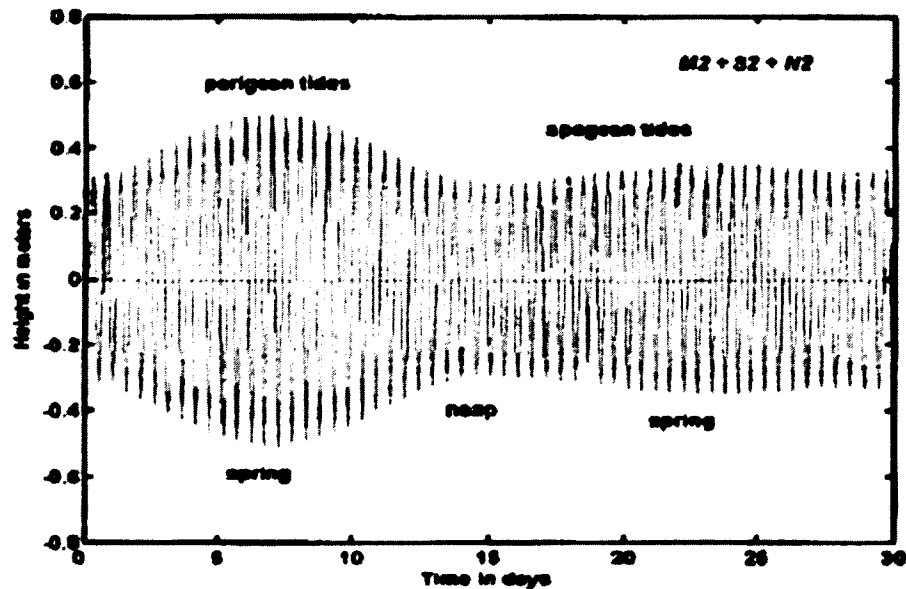


Figure 7. Tide height variation over the course of a month (Taken from Boon, 2004a).

moon's orbit around the earth and from equation (3.1) it can be seen that the gravitational force will change with the square of the distance between the bodies. When the moon is at its closest point of approach, and when the force is greatest, earth experiences the perigean tide. Conversely, when the moon is furthest from the earth, the tractive forces are their least, and the earth experiences the apogean tide. The combination of the spring-neap cycle and the perigean-apogean cycle result in a tidal height plot like the one shown in Figure 7.

Not only does the moon rotate around the earth in an elliptical pattern, but it also changes elevation (inclination) with respect to earth's equator (i.e. it does not continuously orbit around the earth's equatorial plane). When the moon is on the same plane as the earth's equator, it is called an equatorial tide, and when the moon is at the maximum declination, it is called the tropic tide. Figure 8 illustrates this component and Figure 9 is an example of what a tidal height plot might look like with all factors combined.

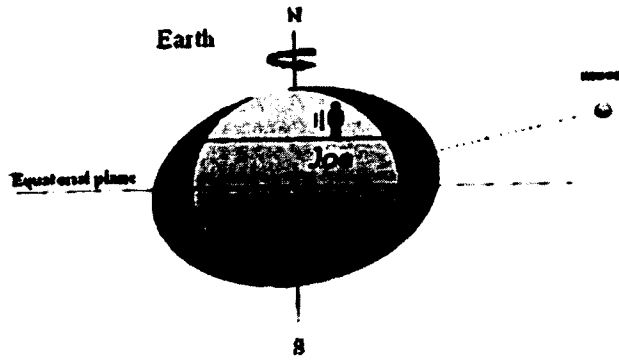


Figure 8. Pictorial example of the moon's effect on the tide when orbiting outside of earth's equatorial plane (Taken from Boon, 2004a).

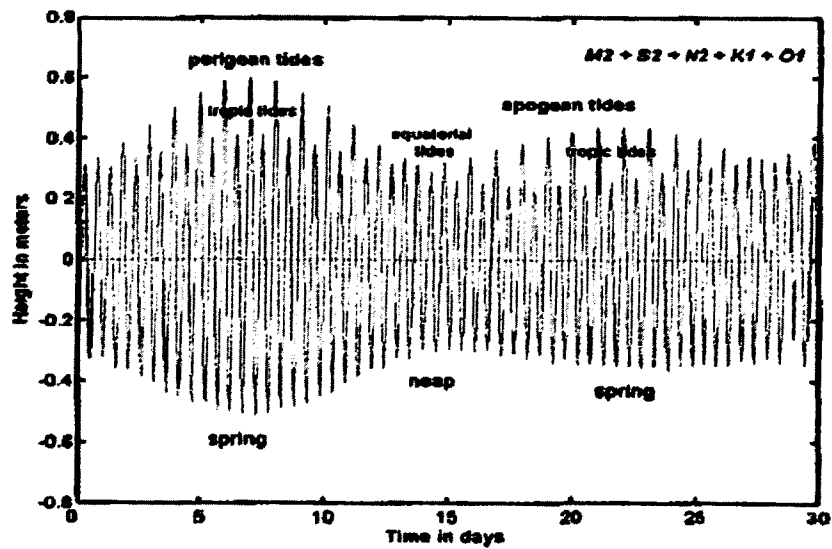


Figure 9. Combined effects of the three major varying components that influence tidal height over the course of one month (Taken from Boon, 2004a).

### 3.1.2 Overview of Harmonic Constituents

It is understood that the tidal height is variable, and now it will be shown that it is predictable. Intuitively, the tidal height over the course of a day is very similar to the motion of a pendulum swinging on a clock. It can therefore be treated as harmonic in nature and can be broken down into the several independent harmonics, called constituents. Tidal currents are driven by tidal height differences, and they, too, are harmonic in nature and can be broken down into independent harmonics, or constituents. Each harmonic constituent will have a frequency ( $\omega$ ), amplitude ( $R$ ) and phase ( $\varphi$ ) and will change with time ( $t$ ). These attributes are combined and each constituent summed in the form of the following equation with  $h_o$  being the mean water velocity.

$$h(t) = h_o + \sum_{j=1}^m R_j \cos(\omega_j t - \varphi_j) \quad (3.2)$$

Each harmonic constituent follows the naming convention of a letter, or series of letters, followed by a number. The most influential constituent is M2, in which the M is to represent the main lunar aspect and the 2 represents the fact that it is semidiurnal, which means it occurs twice daily. The S2 represents the main solar semidiurnal tidal harmonic constituent.

From a collection of raw data from a tidal site over a time period of approximately one month the harmonic constituents can be calculated and then combined in the equation above to enable the prediction of the celestial effects on the tides for the future.

### 3.1.3 Tidal Current Predictions

The process of calculating the harmonic constituents from the raw data was performed using a Matlab code named *Simply Currents* that follows the Harmonic Analysis Method of Least Squares (HAMELS) (Boon, 2004b).

The General Sullivan Bridge ADCP data collected by NOAA in 2007 was imported into an Excel spreadsheet and 29 days were isolated. The 29 days of data was then imported into the analysis portion of the *Simply Currents* Matlab code. An iterative solution to the dominant harmonic constituents was determined and verified by comparing a three day tidal current prediction based on those constituents to three days of the actual recorded tidal current data. The solutions were then imported into a prediction portion of the *Simply Currents* code in which the user is able to select a calendar date or range to generate a plot of the current predictions. The amplitude and phase results for constituents used for prediction are provided in Table 1.

**Table 1. Amplitude and phase values for tidal constituents used in *Simply Currents* predictions. Phase values obtained using single time origin. Local standard time used for analysis and prediction (Boon, 2004b).**

	Constituent					
	O1	K1	N2	M2	S2	L2
Amplitude	0.211	0.213	0.756	4.288	0.693	0.324
Phase	15.01	80.80	148.41	239.91	340.33	256.67

	M4	M6	MU2	2MN6	2MS6	2MK3
Amplitude	0.218	0.503	0.229	0.262	0.250	0.129
Phase	25.23	183.87	309.36	99.54	284.87	207.58

#### 3.1.4 Current Prediction Results

The current predictions provided by the *Simply Currents* code are compared to the predictions provided by NOAA and to the data collected by the Vector ADV on the bow of the test platform. The Vector ADV that was installed at the bow of the test platform during deployments to monitor the tidal energy resource (i.e. tidal currents) was collecting data at 32 Hz. The *Simply Currents* tide prediction code produces a data point every 12 minutes. Therefore, the ADV data was averaged over 12 minute intervals, centered on the *Simply Currents* prediction times, to provide an equal number of data points per plot. The NOAA predictions only provide times and values for peak and slack current so they are easily added as data points during plotting.

The resulting plots comparing the predictions and the actual measured velocity for three days of testing on flood tides (15, 16 and 17 May 2012) at the UNH CORE Tidal Energy Test Site are shown Figure 10. Predicting tidal height is far more accurate than tidal current (e.g. Polagye et.al 2010). Given the complexity, these results are very promising. The slope of the velocity at ramp up for all days is very close to the predicted, and all measured peak velocity values are within half a knot of the predicted value. The slack times agree very closely on the 15<sup>th</sup> and can be inferred to match on the 17<sup>th</sup>. The tide ramped up somewhat quicker on the 17<sup>th</sup> than predicted but did not reach the predicted peak velocity. The velocity then remained steady around three knots for about two hours, but remained slightly below the NOAA prediction throughout the remainder of the (measured) cycle. Two things should be kept in mind: First, the



tidal flow at the site is turbulent and dynamic making prediction very difficult. Second, Figure 10 is a plot of only three tidal cycles, and many more would have to be measured and analyzed to be able to calculate a statistically significant uncertainty in current velocity predictions.

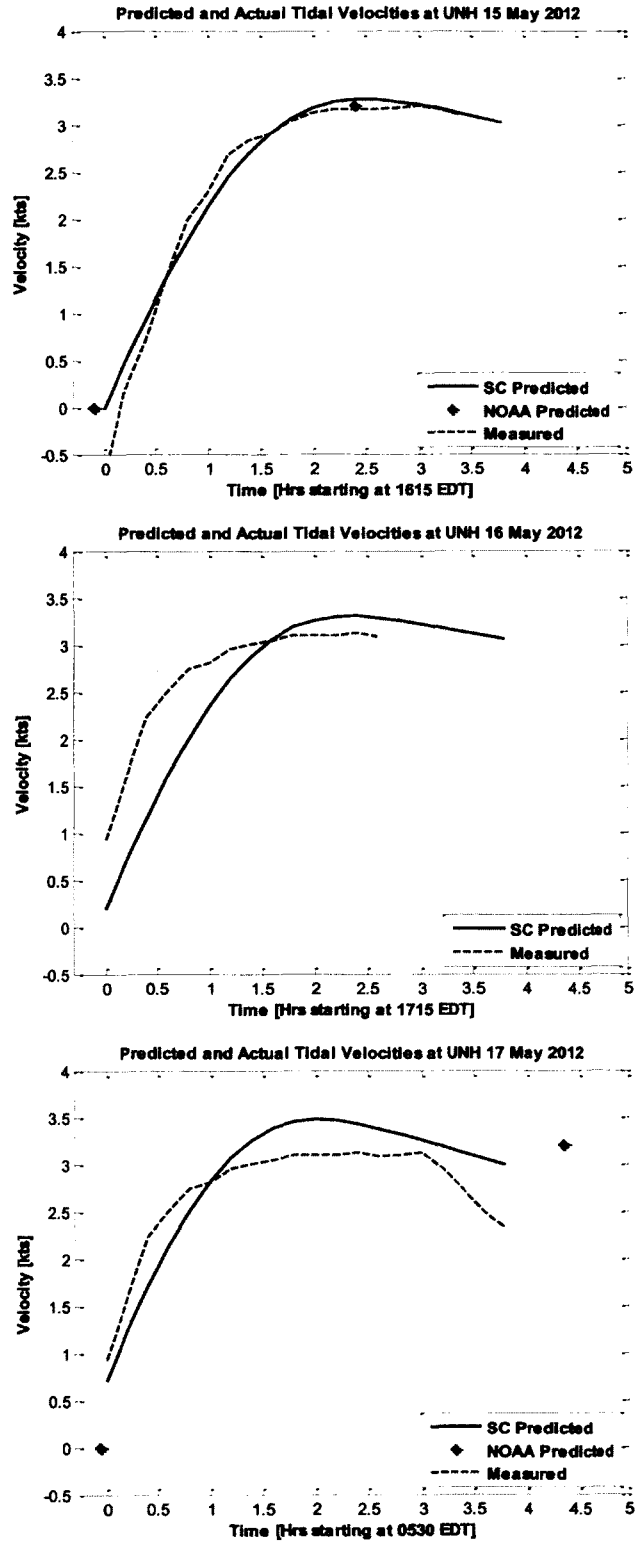
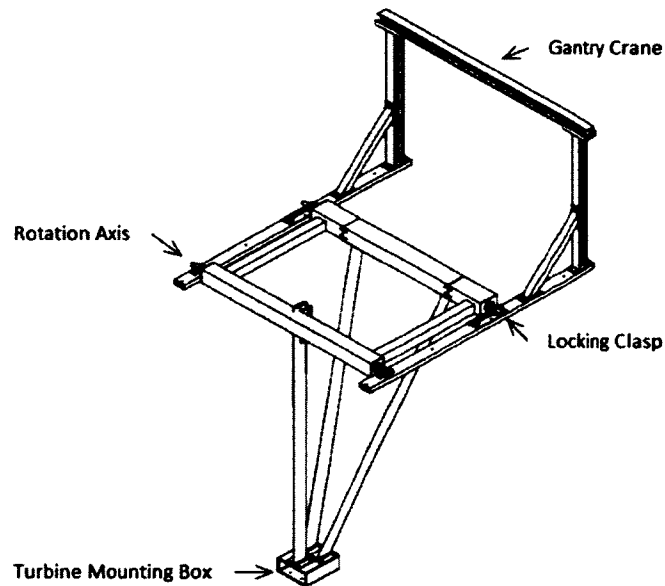


Figure 10. Current predictions and measured velocities for tests at the UNH-CORE Tidal Energy Test Site. NOAA predictions not available for 16 May.

Each prediction method will have subtle differences for each tide and neither will be able to fully account for all factors that drive the tide. Some predictions will be more aligned, and some further off, and it is unlikely that both will match the actual velocity and times exactly. Thus both NOAA and *Simply Currents* predictions serve well as a resource to plan for work on the water and a factor of safety is required on both sides of the time and velocity predictions. Lastly, the motivation to apply the World Currents predictions was to build an understanding for how the tide ramps up, knowing that a smooth sine wave connecting the NOAA predicted points would be inappropriate. In this example, the predicted curve is far closer to the measured velocity than a sine wave connecting the two NOAA data points would be. Subtle differences aside, both methods of prediction are extremely valuable for research purposes.

### **3.2 Tidal Energy Test Platform Renovations**

The UNH-CORE Tidal Energy Test Platform v1 is a 35 ft (10.7m) long, 10 ft (3.0m) wide pontoon boat dedicated to Marine Hydrokinetic (MHK) turbine testing. For this project, the platform was completely renovated, and a new turbine deployment mechanism, instrumentation mounts and wake traversing mechanism were installed. The deployment frame consisted of a generic turbine mounting box at the end of a 9 ft (2.7m) custom hydrofoil tripod frame attached to a topside box beam frame. The box beam frame can rotate around its forward member via a shaft attached to flanged split bearings mounted on a load distributing beam, and is locked in place at the aft member via custom locking clasps. This system enabled rapid and safe turbine deployment and extraction at



**Figure 11. Streamlined rotating tripod, support structure and gantry crane on UNH-CORE's hydrokinetic turbine test platform v.1.**

the test site. A fixed gantry crane with a 2000 lbf (8900N) capacity hoist was used to rotate the tripod turbine frame. Figure 11 is a rendering of the assembled turbine deployment mechanism, fabrication drawings are provided in Appendix A.4.

To allow wake measurements at various locations downstream of the turbine while deployed, all stringers connecting the pontoons aft of the moon pool were removed and replaced with an elevated platform that rigidly connects the pontoons at the stern, but leaves the deck level open to allow full stream-wise positioning of a traversing system. The new aft pontoon coupling, made from 6061-T6 aluminum box beam with gusseted corners, was analyzed for seaworthiness with FEA simulations under different loading and wave scenarios.

Two different types of decking were installed: A fiberglass reinforced polymer grated decking (ThruFlow) was selected for the forward half of the platform, to allow reduction of shock loading and dissipation of energy from a wave strike. The aft half of the platform was covered with marine plywood. The grated decking does not provide the same structural support as the 3/4" marine plywood; this was offset by increasing the number of stringers. A removable plywood working platform was installed over the moon pool. All materials were adequately prepared, primed, painted and/or sealed for the marine environment. A rendering of the renovated UNH-CORE Tidal Energy Test Platform v1 is shown in Figure 12.

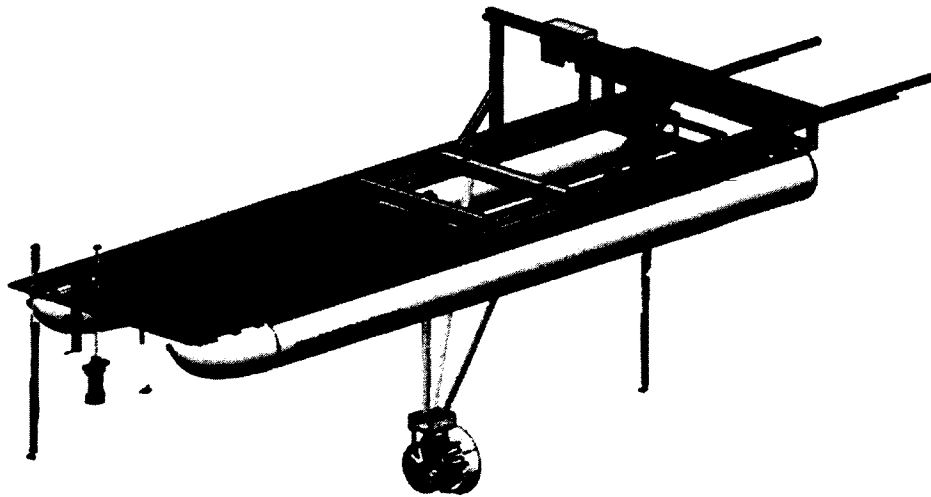


**Figure 12. Rendering of UNH-CORE Tidal Energy Test Platform v1 with MEHT installed on tripod deployment frame.**

### **3.3 Tidal Energy Test Platform Instrumentation**

The instrument load out on the test platform quite possibly made it the most valuable pontoon boat in the Atlantic. The majority of the instrumentation was provided by UNH, and additional instrumentation was provided by FloDesign, the National Renewable Energy Laboratory (NREL) of the US Department of Energy and RDI Teledyne. Figure 13 shows a front view of the test platform with an overview of most of the installed instrumentation with respective deployment depths. Figure 14 shows a side view of the test platform with the streamwise positioning of forward instrumentation, turbine and wake measurements, respectively.

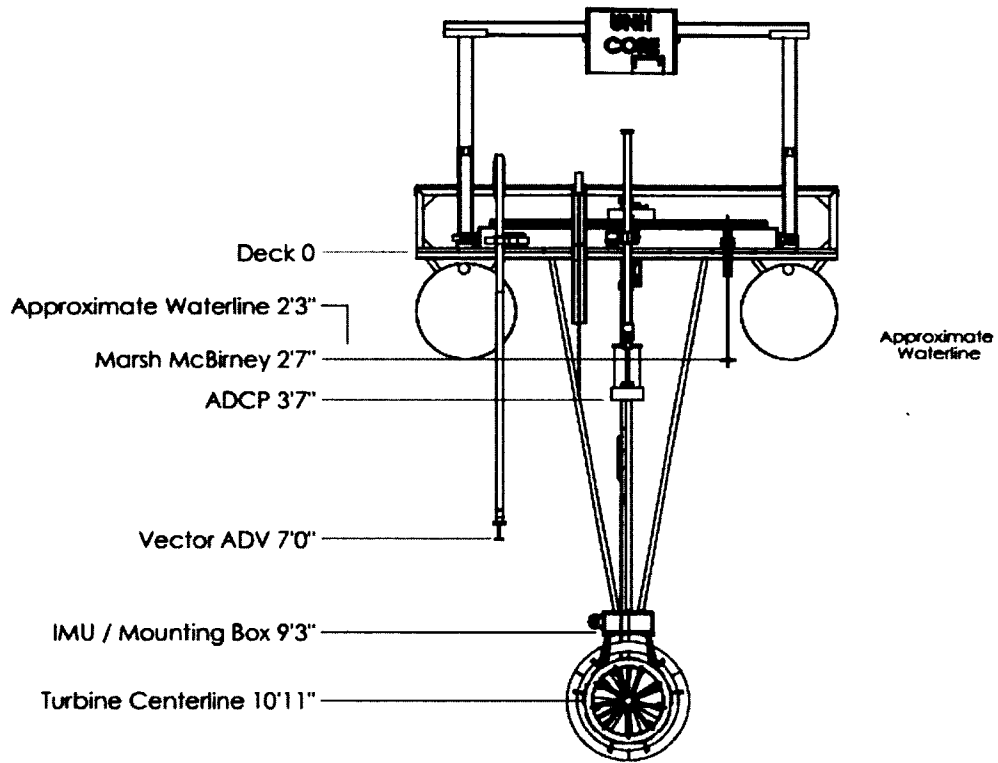


Figure 13. Front view of test platform with depths of submerged instrumentation.

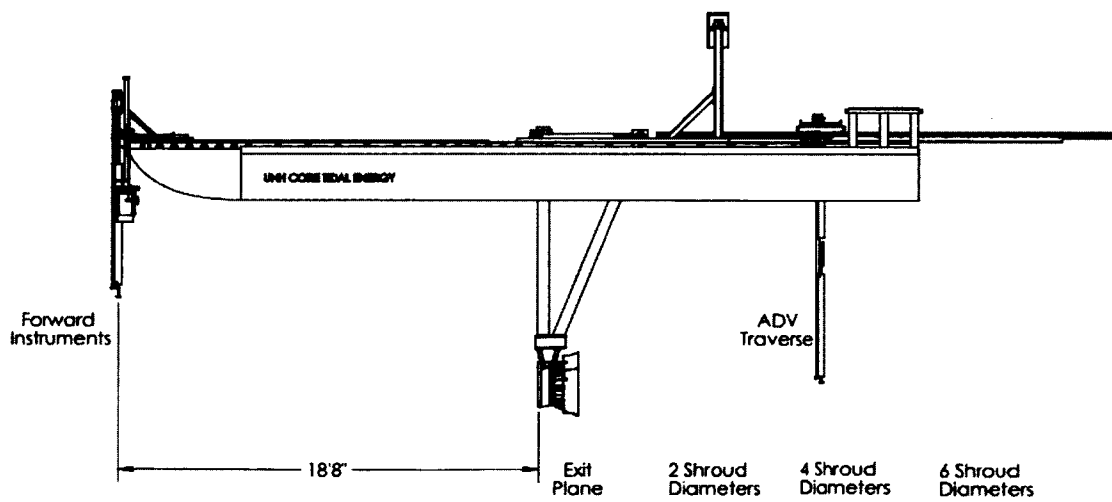


Figure 14. Hydrokinetic turbine test platform side view.

Two Acoustic Doppler Velocimeters (ADV) were used, a Nortek Vectrino (UNH) with a maximum sample rate of 200Hz and a Nortek Vector (NREL) with a maximum sample rate of 32 Hz. The Vector was installed on the starboard bow with the probe head approximately 5 feet (1.5m) below the water line.

Salinity was measured with a refractometer. For deployments reported here, salinity at the UNH-CORE site was measured at 22 parts per thousand (ppt) and for Muskeget Channel it was 33 ppt (+/- 0.5 ppt). An ADCP was mounted just below the waterline centered off the bow of the platform to monitor tidal energy resource. For the UNH-CORE test site deployments, a new RDI Sentinel V (on loan from RDI) was used, for the Muskeget Channel deployments, an RDI Sentinel Workhorse 1200 kHz (UNH) was used. An electromagnetic flow meter (Marsh-McBirney Flo-Mate 2000, UNH) was installed off the port bow of the test platform as a backup velocity measurement and real-time verification of ADV output. An Ocean Sensor Systems, Inc. wave staff OSSI-010-002E (UNH) was mounted off the bow to the starboard of centerline. A Teledyne DMS-05 Inertial Measurement Unit (IMU) and 3 Meggitt Model 745 accelerometers (all NREL) were installed on the turbine mounting box. Two 20,000 lb load cells and swivels (NREL) were used to measure mooring loads, and a Hemisphere V101 GPS Heading Unit (NREL) was used for position measurements. The IMU, accelerometers, load cell and GPS were recorded to a National Instruments (NI) Compact RIO installed in a waterproof box with an independent NI-GPS unit for timing (all NREL). All other instruments were recorded to a CF-53 ToughBook laptop computer. The data obtained with the wave staff were used in combination



with the Teledyne DMS IMU to assess platform motion, for details see Dewhurst 2013 and Dewhurst et al. 2013.

Turbine power takeoff and performance evaluation were performed by FloDesign with their own equipment in a weatherproof enclosure. The 3-phase AC output from the permanent magnet rim generator was monitored with a WT 3000 Yokogawa power analyzer, then converted to DC in a 3-phase bridge rectifier. The power was dissipated in a 5kW DC Kepco electronic load bank, which also provided a signal for the Yokogawa power analyzer.

SeaView and GoPro video systems were used to monitor the turbine and its environs during the deployments. The SeaView cameras (3x) streamed live video through a DVR which enabled virtually unlimited continuous recording as well as real time monitoring. GoPro cameras (2x) provide much higher resolution video but are not viewable in real time and are limited by battery life.

Two inverter generators were used on board the test platform, one Honda EU2000 2kW dedicated to the turbine deployment hoist and one EU 1000 1kW dedicated to instrumentation, data acquisition systems and computers.

Figure 15 shows the test platform deployed on a flood tide at the UNH-CORE Tidal Energy Test Site in Great Bay Estuary. Figure 16 shows the test platform shortly after deployment in Muskeget Channel, with instruments being readied for testing. Figure 17 shows samples of video stills from the turbine under operation, from a GoPro Hero 2 and SeaView camera mounted on a short stinging upstream and above the turbine.



**Figure 15. Tidal Energy Test Platform with MEHT at UNH-CORE Tidal Energy Test Site.**

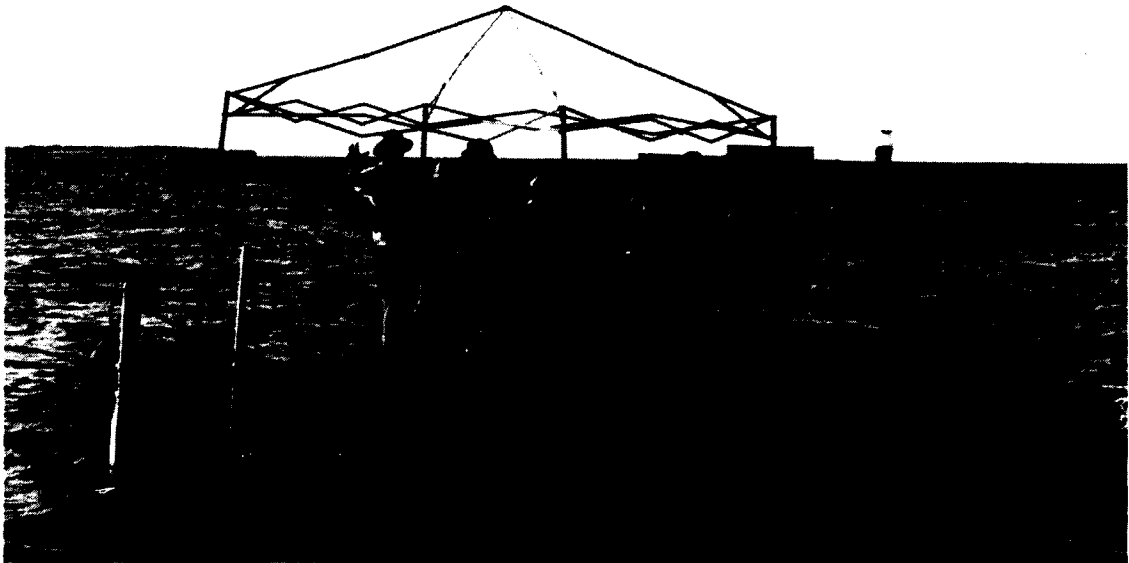


**Figure 16. Test platform readied for testing in Muskeget Channel.**

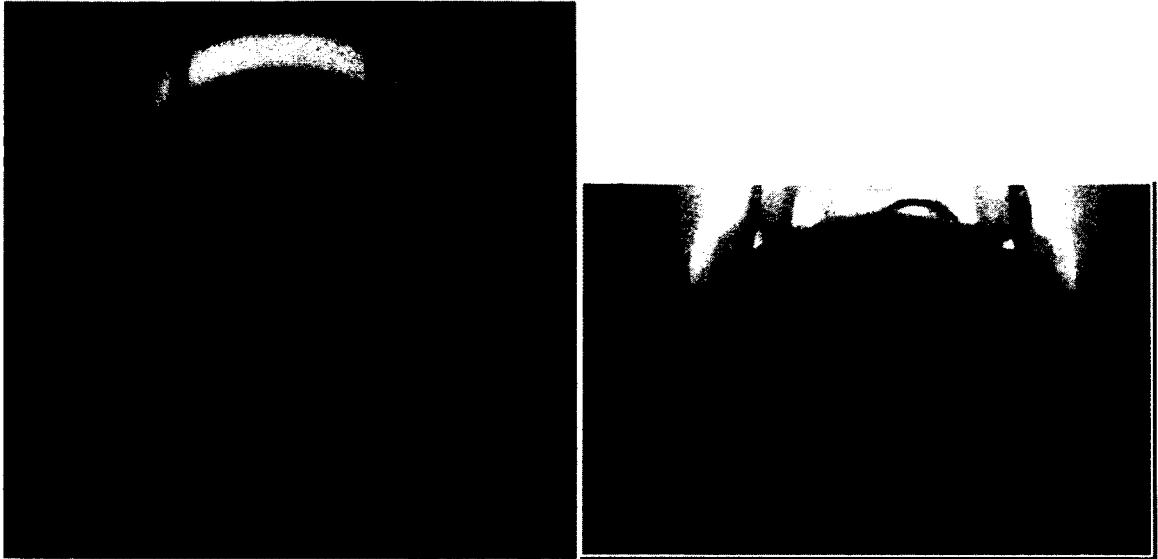


**Figure 17. Video stills of submerged MEHT comparing GoPro Hero 2 (left) and SeaView (right).**

Details of the instrumentation used on the UNH-CORE Tidal Energy Test Platform v1 are given on Appendix A4.

### **3.4 Instrumentation Mounting Designs**

A traversing system was designed to position an Acoustic Doppler Velocimeter (ADV) in two dimensions, cross stream and streamwise, to facilitate measuring the turbine wake in detail. Separate mounts were designed for both an upstream ADV and Acoustic Doppler Current Profiler (ADCP) to measure the incoming tidal energy resource. These instruments did not require mobility, but the mounts were designed with the goal of being able to rapidly deploy and extract the instruments.

#### **3.4.1 ADV Traverse**

The Vectrino was installed on a traversing mechanism that allowed manual streamwise motion and automated cross-stream positioning. Its probe

head was installed so that the measurement volume was at the depth of the of the turbine centerline, approximately 9 feet (2.7m) below the waterline.

Prior to designing the equipment to position the ADV an understanding of what measurements would be necessary was needed. With traversing capability, cross-stream or vertical velocity profiles could be measured. It was decided to measure the wake profiles in the cross-stream direction to obtain a better understanding of the decay of the velocity deficit and to avoid the additional complication of the vertical velocity gradients in an open channel flow. Furthermore, it was decided that a collection of measurements at intervals on the order of two inches would be adequate to profile the wake. Lastly, from flume testing at Alden Labs held by FloDesign, it was shown that the wake was not yet fully restored to free stream flow at 8 shroud diameters downstream of the exit plane of the turbine. Therefore, it was desirable for the traversing system to be able to measure the wake to at least 8 diameters downstream.

For accurate comparison of wake profiles at different downstream locations the traverses had to be performed at approximately constant tidal current velocity. Based on tidal current predictions (c.f. Section 3.1), the goal was to complete a set of traverses in approximately 30 minutes. A cross-stream spacing of measurement locations of two inch was chosen, therefore the traversing system with 60 inch cross-stream travel allowed for data collection at 31 locations. Cross stream traversing speed was set at 1 inch per second. Therefore, one additional minute would be needed for probe positioning in the cross stream axis for each profile. The goal for the deployment at the UNH-

CORE Tidal Energy Test Site was to measure the turbine wake at two, four, six and eight shroud diameters downstream of the turbine exit. Allowing 2 minutes to reposition the traverse to each streamwise position limited sample time to 10 seconds, or 2000 data points at each probe position. In an effort to obtain better statistical averages for wake measurements during the deployment in Muskeget Channel one downstream location, 8D, was eliminated, and sample time was increased to 15 seconds at each probe position.

### 3.4.2 ADV Mounts

Various mounts and stings for the two ADVs were tried. A sting using a schedule 40 aluminum pipe with a foil-shaped streamlining fairing that was mounted so it could rotate to align itself with the flow was found to work best and cause the least instrument motion in a tidal environment.

A Velmex Bislid was used to position the Vectrino ADV in the cross stream direction, and a 60 inch (1.5m) traversing distance was the maximum possible due to the pontoon spacing. The ADV sting mounted to a support frame in such a way that the drag loading was transmitted to Accuride linear bearings on a traversing carriage, not the Bislid. The stream-wise positioning of the traversing system was performed manually utilizing linear bearings on t-slotted extruded rails. The total stream-wise travel was 20 feet (6.1m), and required that the traversing rails be cantilevered off the stern by 7 feet (2.1m).

Details of the instrumentation mounting designs are given in Appendix A5.

#### **4 Mixer-Ejector Hydrokinetic Turbine Testing**

Numerical modeling and testing in laboratory facilities at smaller scale are standard practice as part of the marine hydrokinetic (MHK) device “scale-up” process, eventually leading to open-water testing (still at scale) as a device developer advances through “Technology Readiness Levels” (TRL) (DOE 2010a). Testing in the natural environment removes laboratory problems such as low Reynolds number or blockage effects, but introduces many other complexities including uncontrollable inlet flow (mean and turbulence), off axis flows and fluctuating apparent velocities due to platform motion as a function of wave climate.

Dedicated open-water tidal energy test sites have great value, since different technologies can be tested in the same, well-understood environment. New England has a long history of ocean-related research and development, and significant MHK research and testing infrastructure is already available or presently being developed. A consortium of academic institutions and industry, the New England Marine Renewable Energy Consortium (NE-MREC), provides a complete set of facilities and open-water test sites for the testing needs defined by the Department of Energy (DOE) for MHK technology development in the Technology Readiness Level (TRL) bands 1-9, with TRL 9 being grid-connected deployment of a full scale device: The Center for Ocean Renewable Energy at UNH operates a sheltered “nursery” tidal energy test site for MHK turbines up to 4m diameter in Great Bay Estuary, NH. The University of Massachusetts-Dartmouth (UMassD) is developing a full-scale test site in Muskeget Channel,

MA. The locations of the two sites are shown in Figure 18. In addition to the MHK test sites utilized and described here, the University of Washington is pursuing a tidal energy test site in Puget Sound off Nodule Point (e.g., Thompson et al. 2012) and Florida Atlantic University is developing an ocean current test site off the East Coast of Florida (e.g., Hanson et al. 2010).

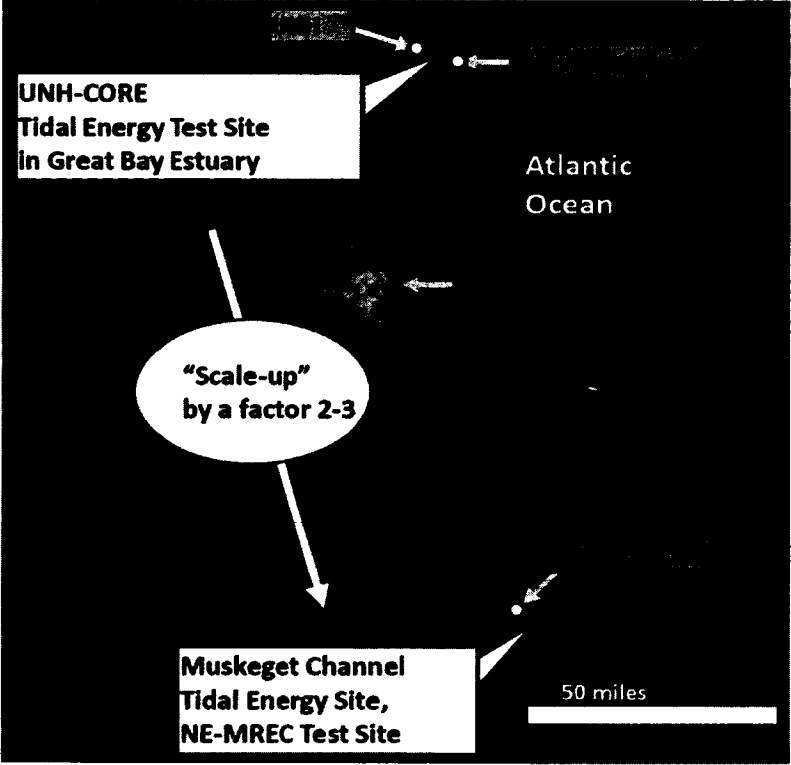


Figure 18. Open-water tidal energy test sites in New England, UNH-CORE (NH) and Muskeget Channel (MA).

**4.1 MEHT Testing Goals**

Prior to testing at UNH the MEHT underwent laboratory bench testing at FloDesign as well as flume testing at Alden Research Laboratories (Alden). The purpose of testing the turbine at the UNH-CORE Tidal Energy Test Site was to gain insight into its performance in a natural environment. Laboratory testing does not truly reflect the natural environment. For instance, the cross section of

the flume at Alden measured 8 ft x 8 ft so the blockage of the 34.7" diameter turbine was about 12% and the turbine performance was influenced by wall and free surface effects. These effects were estimated and corrections were made; however, the result for turbine performance was still an approximation. Testing in the natural environment removes such approximations but introduces a host of other complexities including uncontrollable inlet flow (mean and turbulence), off axis flows and fluctuating apparent velocities due to platform motion as a function of wave climate. Developing an understanding of, and comparing turbine performance in light of these factors is necessary in deciding future design.

Specific MEHT testing goals included; determining rotor cut-in velocity, measuring the power coefficient, measuring the velocity deficit and subsequent decay in the wake, determining yaw torque in off-axis flows and observing any change in these factors for two turbine models, stator-rotor and rotor only.

#### **4.2 Tow Testing**

Tow testing of the MEHT installed on the test platform was performed on two occasions, both serving as a shakedown for equipment prior to a tidal cycle deployment at the UNH Test Site. The first tow test was performed in Portsmouth Harbor off the UNH pier facilities in New Castle in April of 2012. The second test was performed in the Piscataqua River in Little Bay near Great Bay Marina in May of 2012.

The April tow testing was the first time the MEHT was mounted on the test platform and included a functional check of the newly designed turbine deployment mechanism. The platform was towed into Portsmouth Harbor with



the Galen J, the University's 22 foot Eastern work boat. Once in the harbor, the platform and vessel were allowed to drift and the turbine deployed. Once it was confirmed that all systems were operating as expected the turbine was towed at idle while power was extracted and monitored by FloDesign. Speed was incrementally increased to 4 knots while monitoring all mounting and power takeoff systems.

The April testing proved the functionality of the turbine deployment mechanism and overall integrity of the renovated test platform. The Galen J was found to be an adequate work vessel in the relatively benign environment of the sheltered channel. The power take-off and monitoring equipment and associated weather proofing was found to be adequate by FloDesign. Video footage from a camera facing the turbine inlet proved functionality of the system. Though an overall success, there were lessons learned for both the UNH and FloDesign teams and the following month was used to make necessary changes for the scheduled deployments at the UNH Test Site.

The May tow testing primarily served as a test run for the newly installed Acoustic Doppler Velocimeter (ADV) wake traversing mechanism. In preparation for the tide cycle testing at the UNH Test Site, a berth at the Great Bay Marina was rented due to its close proximity to the test site and the tow testing was conducted in Little Bay in the Piscataqua River near the marina. The same procedure was followed as in April, but power data was not recorded and instead efforts were focused on measuring and marking downstream distances for wake

traversing and refining the code for the BiSlide stepper motor driver. The following day was the first tidal cycle test at the UNH Test Site.

#### **4.3 Deployments at the UNH-CORE Tidal Energy Test Site**

The Great Bay Estuary (GBE) system is a tidally driven estuary that is one of the most energetic on the East Coast of the United States. The GBE is well studied and surveyed (1976, 2007) and has been modeled numerically to understand its dynamics and circulation. The first order dynamics of this system and tidal analysis results were discussed by Swift and Brown (1983), more recent numerical modeling was reported by Erturk et al. (2002) and Bilgili et al. (2005). The UNH-CORE Tidal Energy Test Site at the General Sullivan Bridge (GSB) is located in a constricted area in the estuary, with easy access from nearby marinas or the two local UNH marine facilities. The site has the fastest tidal current velocities in the estuary with maximum currents at over 5 knots (2.6 m/s), and typically greater than 4 knots (2.1 m/s), and hence it is an excellent site for testing tidal energy conversion devices. The test site has a minimum depth of 8 m (26 ft) at LLW and can be used for turbines up to 4 m (13 ft) in diameter. A 35-ft x 10 ft (10.7m x 3.0m) test platform has been used since 2008, and a larger 64 ft x 34 ft (19.5m x 10.4m) test platform with a modular turbine deployment system was designed to accommodate larger turbines (Byrne, 2013). Funding for the larger test platform was secured, and the mooring and acoustic monitoring systems are currently undergoing an environmental assessment through the DOE. The UNH-CORE Tidal Energy Test Site is well suited to support open-water MHK testing through DOE TRL 7.

#### 4.3.1 Logistics

Of the many logistics involved in open-water testing of a tidal turbine, vessel acquisition and manning was critical. The Galen J, a 22 foot Eastern berthed at the UNH Pier was dedicated to test platform transport and had to remain tied to the platform at all times during testing in the event of an emergency. To assist in mooring the platform and transporting people, it was determined that another boat would be necessary. An 18 foot Eastern from Jackson Estuarine Laboratory was dedicated to untethered support to the test platform. Both Jackson Lab and the New Castle pier facilities are an hour tow from the UNH-CORE test site at General Sullivan Bridge, so a marina slip was rented from Great Bay Marine that served as the staging area for the testing.

#### 4.3.2 Mooring Plan

The mooring design evolved to a bridled configuration between two bridge abutments with the intention to have the test platform centered in the first bay to the east of the shipping channel. The mooring options were complicated by the fact that the new Route 4/16 bridge was under construction at the time. UNH personnel met with the NH Department of Transportation (DOT) and Cianbro, the bridge construction company, to coordinate securing mooring lines to existing bridge infrastructure. As a result, deployments were limited to the flooding tide and involved tying lines to two of the older General Sullivan bridge abutments.

A 5/8<sup>th</sup> inch 3 strand polypropylene line was chosen for the mooring line due to its cost, strength and buoyancy. Two 25 foot semi-permanent mooring lines were installed a week prior to testing to the top of the two GSB abutments

east of the shipping channel. A loop was tied to the free end to allow for a quick connection of another long section of mooring line upon arrival for testing. A mooring float was tied to the free end to provide visibility and enable rapid recovery. This process was performed on two bridge abutments spaced 200 feet apart.

Two other sections of 150 feet of 5/8<sup>th</sup> inch 3 strand polypropylene line, with a loop on each end, were cut and coiled. To moor the test platform the Galen J would position it near the testing location during slack water at low tide. The other support vessel would attach one 150 foot line to a line on a bridge abutment and run it back to the platform. The line would be secured to the test platform in line with one of the load cells. The support vessel would then repeat the process with the other line. The tidal currents on the flood tide are not perfectly aligned with the bridge abutments; hence this design with mooring lines of equal length resulted in one mooring line, the starboard one, taking the load with the port one laying slack in the water. The design was improved by installing a bridle on the test platform, and forming a bridle with the 150 foot mooring lines. Connecting the bridles with a shackle allowed the platform to position itself evenly distributing the mooring load. The bridle to bridle configuration schematic and view from the bow of the test platform is shown in Figure 19.

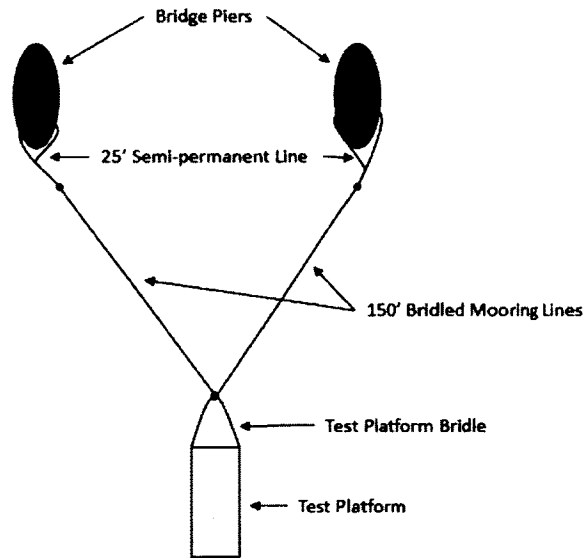


**Figure 19. Enhanced twin bridled mooring configuration schematic (top) and view from test platform (bottom) at UNH-CORE Tidal Energy Test Site.**

#### **4.3.3 UNH-CORE Tidal Energy Test Site Testing Timeline**

The May testing dates were established approximately one month in advance. On May 11<sup>th</sup> the semi-permanent mooring lines were installed around the bridge abutments at the test site. On May 14<sup>th</sup> the platform was towed up the river to Great Bay Marina to meet FloDesign. The turbine and instrumentation

were installed on the 14<sup>th</sup> in time for an afternoon tow test to verify equipment functionality. Due to mooring line configuration, it was only possible to test on the flooding tide so the platform had to be moored during slack low water. Testing was limited to daylight hours due to safety concerns. The platform was moored for the first test on May 15<sup>th</sup> at approximately 4:15pm. The following day's low tide slack was at 5:15pm which resulted in the test finishing near dusk. Therefore, there was a quick turnaround after testing on the evening of the 16<sup>th</sup> in order to be out for the morning flood at 5:30am on the 17<sup>th</sup>. Following the test on the morning of the 17<sup>th</sup> the platform was transported with the ebb tide to the UNH pier in New Castle to break down the instrumentation and conclude the deployments at the UNH-CORE test site. Table 2 is a snapshot of deployment specifics showing average nominal turbine performance during wake traversing for each day of testing at the UNH Tidal Energy Test Site.

**Table 2. Deployment specifics and average nominal turbine performance at the UNH Tidal Energy Test Site. Note: power coefficient calculated using rotor area.**

Date	Slack Time	Model	Peak Velocity [kts]	Mean Rotor Power [W]	$C_p$
15-May	4:15 PM	Stator-Rotor	3.2	499	1.14
16-May	5:15 PM	Rotor Only	3.2	413	0.96
17-May	5:30 AM	Rotor Only	3.1	396	0.95

#### 4.3.4 Data Collection and Results

Prior to testing, drag loading estimates were made to justify to the Department of Transportation that the added loads due to mooring forces are insignificant in comparison to the forces on the bridge abutments during

maximum flow conditions, or king tide. The load cells in line with the mooring lines confirmed that actual mooring loads were quite low. The result of the mooring force measurements are shown in Figure 20. The load cells were sampled at 50Hz, a calibration/conversion factor was provided to convert units of mV/V to pounds force for each load cell. The geometry of the mooring lines was taken into account and the load cell values were added and averaged over one minute for Figure 20. Mooring load results from May 15<sup>th</sup> are unavailable.

Free stream velocity measurements were collected at 32 Hz and averaged over one minute in the streamwise direction to yield Figure 21. The time when wake profiles were measured are marked on the free stream velocity plots.

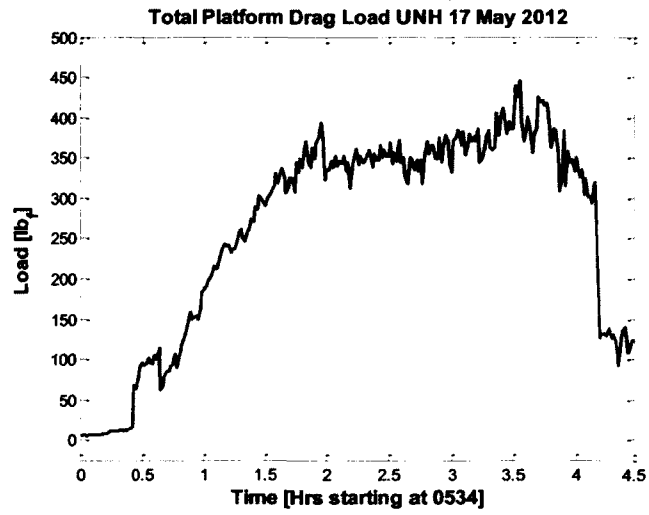
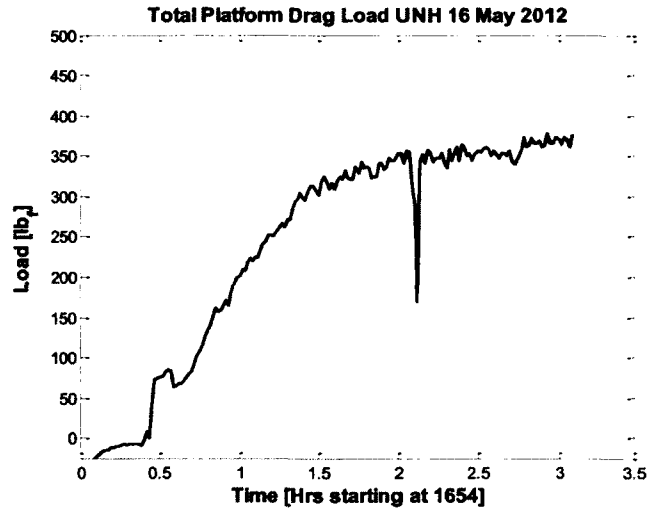


**Figure 20. Total mooring load on May 16<sup>th</sup> (top) and May 17<sup>th</sup> (bottom) at UNH Test Site.**



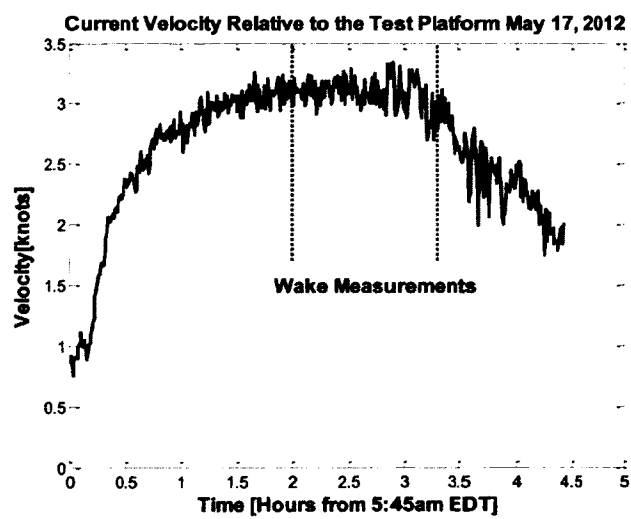
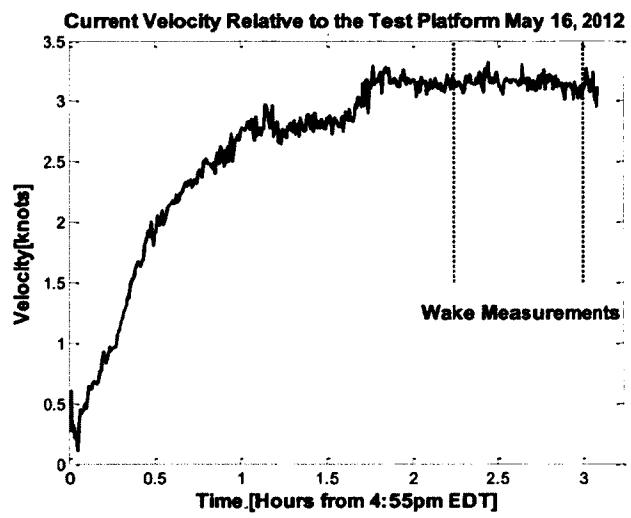
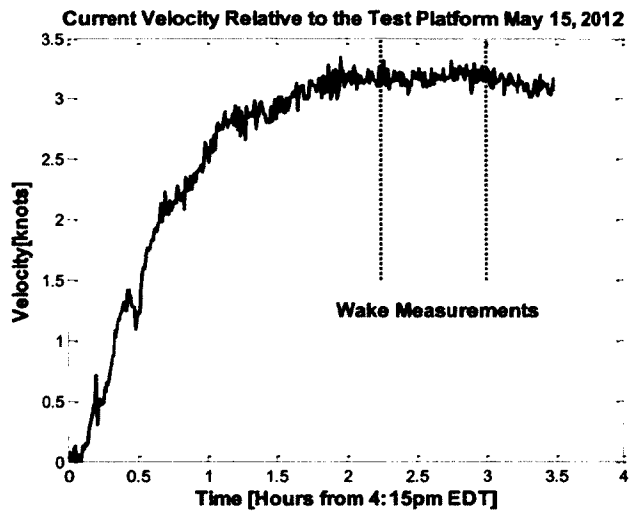


**Figure 21. Current velocity recorded on Vector ADV during testing at the UNH Tidal Energy Test Site.**

Around peak conditions on May 15 (corresponding to the wake measurement period) the mean power extracted was 499 W, resulting in a power coefficient based on rotor diameter of 1.14 as seen in Table 2. Note that the derivation of power extraction from first principles bases the modified power coefficient for shrouded devices on rotor diameter, however, it has been suggested that the largest diameter of the device should be used. Note that only nominal power values are presented here. For more details on turbine performance c.f. FloDesign's final report to the US Department of Energy (2013).

Drag area is defined as the product of drag coefficient and frontal area. The frontal area of the MEHT is known and the drag (=thrust) coefficient of the MEHT was measured in tow tank testing at 1 m/s. The drag coefficient was assumed to be constant for the operating range of the MEHT, since at 1 m/s the Reynolds number based on shroud diameter

$$Re = \frac{uD}{\nu} \quad (4.1)$$

where  $u$  is mean velocity,  $D$  is the shroud diameter, and  $\nu$  is the kinematic viscosity of water, was already  $Re_D = 9 \times 10^5$ . The time at which the tidal current velocity reached 1 m/s was determined from ADV data. The total drag load at that time was determined from the load cell data. The drag area of the MEHT can be subtracted from the total drag area to determine the drag area of the test platform (plus Galen J tied up to it). The drag with respect to tidal current velocity can be calculated using the drag area of the turbine, drag area of the test platform and free stream velocity from

$$F_D = [(C_D A)_T + (C_D A)_P] \frac{1}{2} \rho u^2 \quad (4.2)$$

where  $(C_D A)_T$  is the drag area of the MEHT,  $(C_D A)_P$  is the drag area of the test platform and  $u$  is free stream velocity.

The measured total drag on May 17<sup>th</sup> at 1.5 m/s was 336lb<sub>f</sub>. Using a turbine drag coefficient of 1 (c.f. section 4.5.4) and frontal area of 0.61m<sup>2</sup> the drag area of the test platform was found to be 0.62m<sup>2</sup>. The calculated total drag load from equation (4.2) is compared to measured drag in Figure 22. The agreement between measured load and calculated load suggest that 0.62m<sup>2</sup> is an appropriate drag area to use for future test platform mooring design in which the Galen J is used as the support vessel.

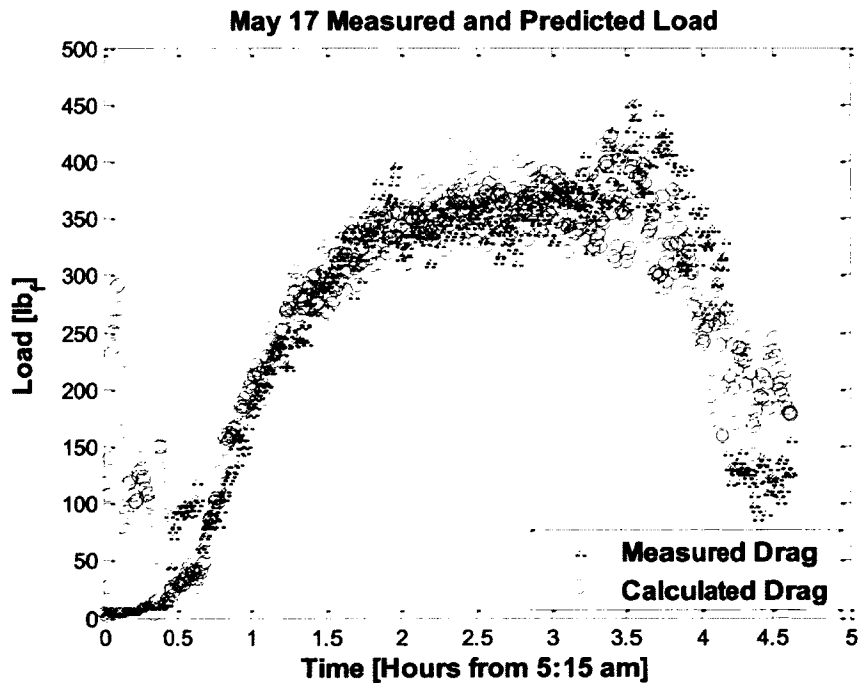
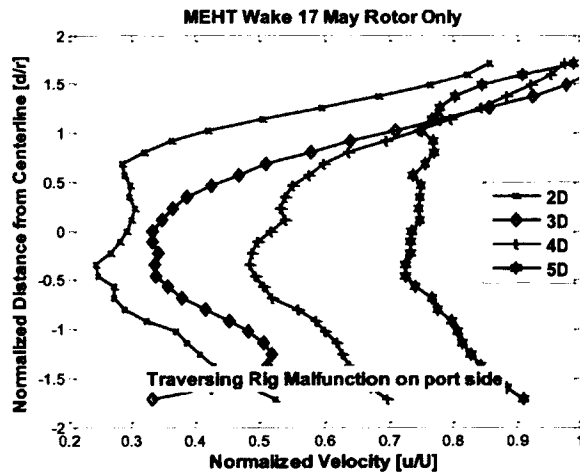
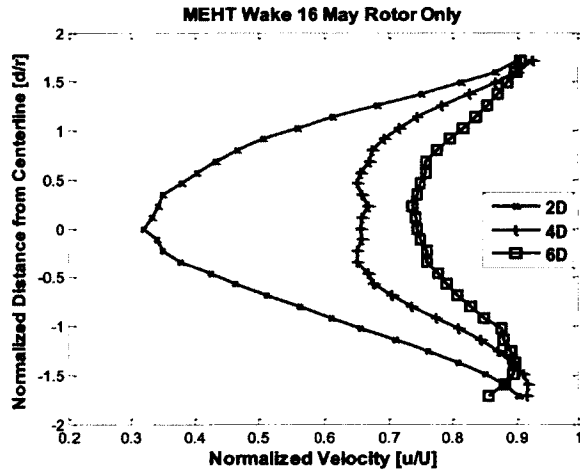
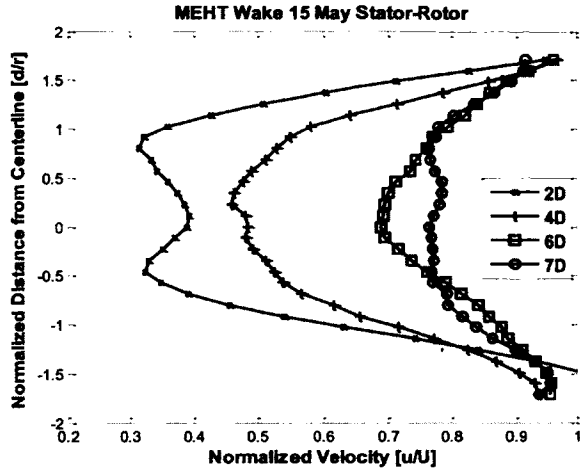


Figure 22. Measured drag and calculated drag on May 17<sup>th</sup> based on platform drag area of 0.62 m<sup>2</sup>.

The most challenging measurements in this series of testing were the velocity deficit and turbulence measurements in the wake of the turbine, which were attempted for the first time during these deployments at the UNH test site. The measurements were successful, but not without problems. Examples included higher than anticipated friction on the wake traversing rig, and motion of the submerged hydrofoil-shaped sting from lift forces due to three-dimensional flow.

Valuable data were collected from the testing, despite the challenges. Figure 23 shows the normalized wake velocities for each day ranging from 2 to 7 diameters downstream. The ADV was sequentially positioned at 31 cross stream locations by a stepper motor connected to a lead screw and recorded either 10 or 15 seconds of data at each location. It was then manually moved to the next downstream location to repeat the cross stream traverse. The data at each location are isolated and averaged to form one data point at each cross stream location. Each data point is normalized by the free stream velocity corresponding to the time at which the wake data was recorded. The cross stream position is normalized by the shroud radius of the turbine where negative values are to port and positive values are to starboard. Each wake profile is smoothed using a third order polynomial Savitsky-Golay smoothing filter with a frame size of 11 (Savitsky & Golay, 1964).



**Figure 23. Normalized wake velocities at peak tidal flow at the UNH Tidal Energy Test Site.**

The stator-rotor model of the MEHT was tested on May 15<sup>th</sup> and the stator-only model was tested on May 16<sup>th</sup> and 17<sup>th</sup>. At 2 diameters downstream a small higher-velocity region at the center of the wake due to the hollow center body of the turbine can be identified in the data from May 15<sup>th</sup>. That effect is reduced quickly and hardly distinguishable at 4 diameters downstream. This effect cannot be distinguished as clearly at 2 diameters downstream on the 16<sup>th</sup> or the 17<sup>th</sup>, suggesting that the higher velocity region due the hollow center body is mixed out more quickly with the rotor-only model of the MEHT. For each day of testing the wake velocity deficit decay is apparent and comparable. By 7 diameters downstream the velocity is restored to approximately 80% of the free stream velocity. There is a clear influence on the port side on May 17<sup>th</sup> that is explained by wear on the traversing mechanism. Specifically, during departure from testing on the 16<sup>th</sup> the platform went broadside to the current creating significant lift on the NACA 0020 airfoil sting which damaged the mechanism sufficiently to cause reduced performance/positioning accuracy on the port side in the system.

Though only 10 or 15 seconds of data were recorded at each location, the high sample rate of the ADV enables the observation of the turbulence intensity in the wake. Turbulence intensity is the ratio of the standard deviation of the fluctuating component of the velocity divided by the mean flow (Panton, 2005). Turbulence imposes a cyclical load on the turbine parts in addition to the steady load. Cyclical, or fatigue loading of MHK turbines can produce progressive damage that will ultimately lead to structural failure. Fatigue loading is difficult to

characterize accurately, but it is generally agreed that it is correlated to turbulence intensity; therefore this is an important quantity for turbine developers. Commercial computational fluid dynamic (CFD) codes, which are used frequently for turbine design, also require a turbulence intensity input when analyzing fluid interactions.

The streamwise component of velocity can be separated into a mean and fluctuation component by Reynolds decomposition.

$$u = \bar{u} + u' \quad (4.1)$$

The turbulence intensity is the standard deviation of the fluctuating component divided by the mean.

$$TI = \frac{\sqrt{\frac{\sum_{n=1}^N (u - \bar{u})^2}{N}}}{\bar{u}} \quad (4.2)$$

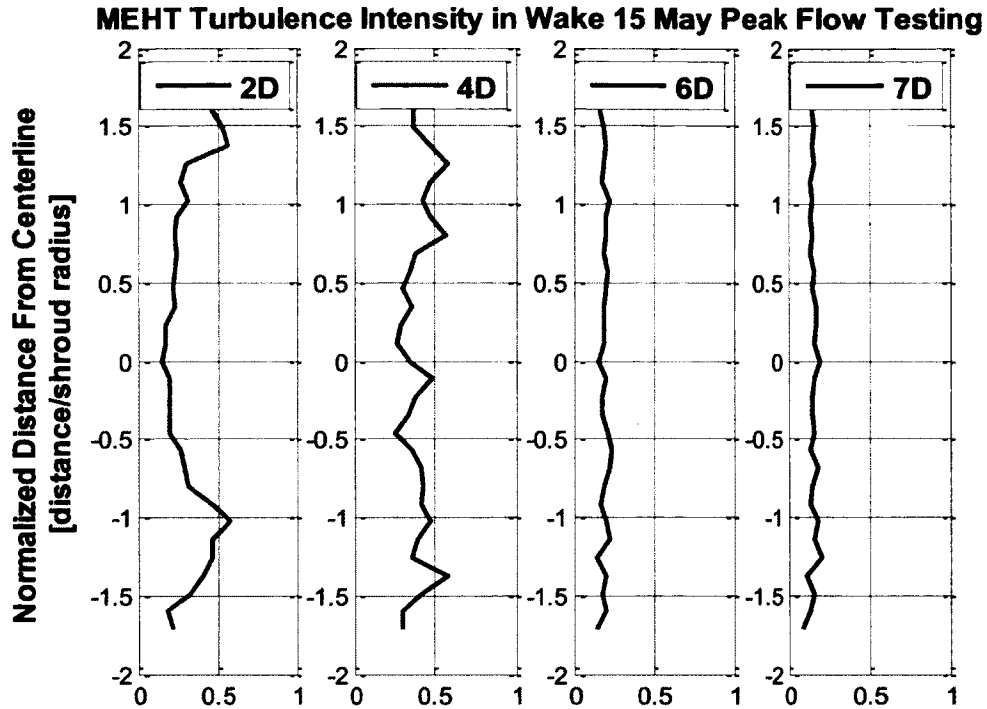


Figure 24. Turbulence intensity in the wake of the MEHT.

Figure 24 shows the streamwise turbulence intensity at each traverse location for each downstream position for May 15<sup>th</sup> normalized by centerline velocity. Close to the turbine outlet it can be seen that the turbulence intensity peaks over 50% in the wake of the ejector/ring-wing shroud, whereas by 7 diameters downstream the turbulence intensity is half that value. The Vector data during this traversing period is isolated and the turbulence intensity over the duration of the wake measurements was calculated to be 7%. Therefore, the flow at 7 diameters downstream is still approximately twice as turbulent as the inlet flow. Comparable studies with acoustic instrumentation in tidal energy sites have found free stream turbulence intensities in the vicinity of 10% (Thomson et al., 2012).



#### 4.3.5 Concluding Remarks

Testing the MEHT at the UNH-CORE Tidal Energy Test Site marked the first successful externally-funded turbine deployment at the site, after previous research deployments funded by the University of New Hampshire. The first true test of the redesigned UNH test platform was a success, and the MEHT performance met expectations. In particular, the velocity deficit decay profiles of the wake were similar to previously collected data by FloDesign in flume testing. A distinct difference in wake velocity profiles at 2 diameters downstream was discovered between the stator-rotor and rotor only models with respect to the stators effect on velocity behind the hollow center body. Turbulence across the wake was measured and compared to free stream turbulence. The drag area of the test platform was determined and verified, and the tidal current predictions were verified. Perhaps most importantly, experience was gained so that a safe, effective approach was applied to open water testing at Muskeget Channel in July 2012.

#### 4.4 Deployments at Muskeget Channel

Muskeget Channel is the north-south channel between the islands of Martha's Vineyard and Nantucket, MA, connecting Nantucket Sound to the North with the Atlantic Ocean to the South. The Town of Edgartown, MA holds a Federal Energy Regulatory Committee (FERC) Preliminary Permit to explore generating electricity from tidal currents with a pilot project of up to 5 MW capacity. In parallel the Marine Renewable Energy Center (MREC) of UMassD is establishing an MHK test facility. While a satellite view shows open water on the

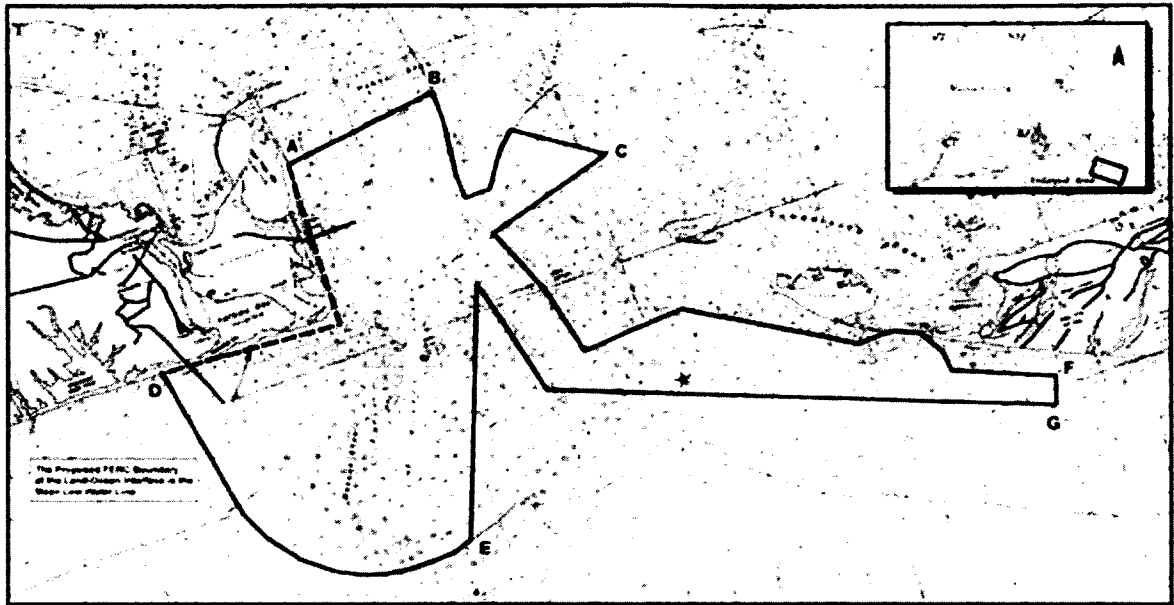


**Figure 25. Chart of Muskeget Channel with tidal energy resource outlined ([www.mrec.umassd.edu](http://www.mrec.umassd.edu)).**

order of 10 nautical miles between the two islands, detailed bathymetry reveals mostly shallows with a comparatively narrow, deep channel near Martha's Vineyard-Chappaquiddick between Wasque Shoal and Mutton Shoal which has the highest tidal current velocities and is shown in Figure 25. This area was recently studied by Howes et al. (2009, 2011) for its suitability as a tidal energy site and environmental effects. With depths up to 50 m (164 ft) and tidal currents up to 2.5 m/s this site is suitable for full-scale MHK device testing, which can be conducted either by deploying from fixed bottom mounted structures with power and data connections (similar to the European Marine Energy Centre), or from floating platforms. The technical feasibility of different turbine deployment concepts was investigated by UNH-CORE in a two-year study resulting in a conceptual design for the facility (Dewhurst 2013). Once grid-connected, the

Muskeget Channel test site will support open-water MHK testing through DOE TRL 9.

#### 4.4.1 Logistics

The week-long deployment of the MEHT with the UNH Tidal Energy Test Platform at the Muskeget Channel tidal energy test site in July 2012 was funded by MREC. After careful planning, the mobilization began on July 12, 2012 with the Galen J towing the test platform to the public boat ramp at Peirce Island in Portsmouth, NH for transfer to a trailer for haul to Fairhaven Shipyard in Fairhaven, MA. FloDesign loaded the turbine, power analyzer and load bank to the deck of the platform at Fairhaven prior to launch. The platform remained in a slip in Fairhaven overnight.

The following morning, July 13<sup>th</sup>, the platform was relocated to a public pier for a press conference organized by MREC. During this event the R/V First Light arrived from its homeport in Hull, MA. All remaining gear was loaded and the test platform readied for tow to Edgartown Harbor, about a 6 hour tow, the following day.

The R/V First Light and UNH-CORE test platform shared a mooring in Edgartown Harbor at the mouth of the entrance. Transfer of equipment and personnel to and from land was accomplished either by dinghy provided by the First Light, or by driving the vessel to the public wharf

#### 4.4.2 Testing Timeline

The National Ocean and Atmospheric Administration (NOAA) publishes tidal current predictions for Muskeget Channel as times of slack water and

maximum currents with magnitude of maximum currents, similar to how they are published for the UNH-CORE Test Site. Based on those predictions the earliest slack water near sunrise was preferred to deploy during daylight hours and to avoid the typically occurring afternoon winds and associated surface chop.

The weather upon arrival was conducive to testing so the mooring deployment and testing began on the 15<sup>th</sup> of July. The 16<sup>th</sup> also proved to be a good test day, though in the afternoon the wind and waves picked up approaching the prescribed sea state limit of three per the Douglas Sea Scale. After two days of open water testing some of the equipment on the platform needed modification and repair so Tuesday the 17<sup>th</sup> was an in port work day. Wednesday morning was too rough to deploy, and the afternoon threatened thunderstorms. Even with a 2 hour tow between the test site and the harbor it was decided that the slim possibility of good testing conditions outweighed the risk of storms, and Wednesday afternoon and Thursday morning two deployments were attempted but aborted due to sea state. Thursday afternoon calmed down and proved to be the best testing conditions of the week.

The mooring was recovered the morning of Friday the 20<sup>th</sup> of July. Most of the equipment was offloaded into trucks and the platform was towed back to Fairhaven Shipyard late Friday morning, arriving in the afternoon. One UNH engineer stayed in MA to coordinate hauling the test platform the following Monday. The platform was hauled back to Peirce Island where it was met with the Galen J for tow back to the UNH pier facilities. The remaining equipment was removed from the platform at the UNH pier.

#### 4.4.3 Mooring Design

Several mooring designs were considered and modeled. The load the turbine and platform would exert on the mooring at the maximum predicted flow and sea state conditions was calculated, and simulated in wave tank test using a Froude-scaled 1:9 model (Dewhurst, 2013). At Muskeget Channel the platform was moored on a single-point mooring, set on July 15 in approximately 70 ft (21m) (the exact depth varied depending on exact position of the test platform) of water just north of the channel markers and Northwest of Mutton Shoal. The mooring was recovered after testing was concluded on July 20. The bridle from the platform attached to 100 ft (30m) of 1" mooring line to a 3 ft (1m) surface float, then connected to 280 ft (85m) of 1 in mooring line to a half shot (45 ft) of ¾ inch chain to a 500 lb (227kg) Danforth embedment anchor. A schematic of the mooring design is shown in Figure 26. The MEHT was deployed in Muskeget Channel on July 15, 16 and 19, 2012. Testing on July 15 was during ebb tide with maximum currents of 2.8 kts (1.4m/s) and sea state 2-3. Testing on July 16 was during ebb tide with maximum currents of 2.8 kts (1.4m/s) and sea state 3. The next successful deployment was on July 19 during flood tide with maximum currents of 3.6 kts (1.9m/s) and sea state 1-2. Modeling and tank testing indicated that the test platform should not be deployed in sea states higher than three on the Douglas Sea Scale.

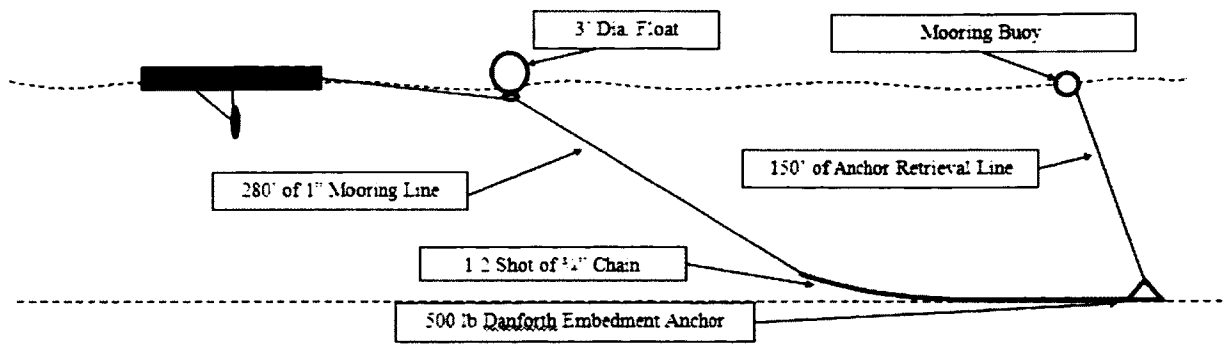


**Figure 26. Test platform mooring configuration used for Muskeget Channel deployments(Dewhurst, 2013)**

An alternative mooring scheme that was used during testing in Muskeget Channel in 2011, conducted by MREC and the Massachusetts Maritime Academy, was to keep the platform in tow behind the support vessel and anchoring the support vessel. This option was not further considered to eliminate any effects the wake of the vessel would have on the turbine inflow. The length of mooring lines and buoyancy of the mooring ball were carefully considered to minimize the influence on the inlet flow in the chosen mooring configuration, shown in Figure 26.

#### 4.4.4 Deployment and Recovery Process

For a typical deployment, the harbor departure time was set by the test window, beginning with slack water, plus setup and transit time. For the transit, the platform would be in tow behind the R/V First Light. Upon arrival at the test site the platform would be tied alongside the R/V First Light so people could board and transfer equipment. With the platform on the hip, the captain and mate would recover the floats attached to the end of the mooring line and pass it to the crew on the platform to secure it to the platform bridle. Once the platform was

tied to the mooring the First Light would cast off and take station nearby, either fulfilling other duties regarding a seakeeping study (c.f. Dewhurst 2013), or idling or anchoring. The support vessel stayed within sight of the test platform at all times and communications between the two vessels were maintained by handheld VHF marine radios.

Once on site and independent from the support vessel the ride on board the test platform was generally smooth and tolerable. For the first deployment only four people were on the test platform, two from FloDesign and two from UNH. For the second and third deployments, one additional person from UNH was on the platform to help with setup and measurement tasks. By the third deployment, the total time to perform mooring, instrumentation installation and setup, and turbine preparation and deployment was reduced to about 30 minutes. It was essential to deploy the deep draft instruments while at slack water, otherwise drag loadings made it impossible to install them in the mounts. For this reason the wake-traversing ADV was not deployed on the first day of testing.

The first half hour after mooring, while still near slack water, was a period of intense activity of people installing and readying for testing all the equipment and instrumentation. The general responsibilities were as follows: FloDesign engineers started the generators, inspected the turbine, started the power quality analyzer and load bank and verified wireless connectivity with the laptop and functionality of the software. UNH engineers would connect all flow measurement instruments to the data acquisition laptop, then deploy and test the Vector ADV,

ADCP, wave staff, and Marsh McBirney. Concurrently the wake-traversing ADV would be lowered into place and the traversing system and controller checked for connectivity and functionality. All NREL equipment in its waterproof enclosure would start recording as soon as power was supplied to the CompactRIO, but the GPS needed to be checked to ensure it acquired a signal to accurately assign a timestamp to the data. FloDesign and UNH shared the responsibility to set up the video systems, both the live feed from the SeaView cameras as well as the high definition GoPro cameras. Once all systems were verified as functional the turbine was lowered into the water. Ideally this still occurred near slack water, but even if the tidal current ramp-up had begun, the deployment could proceed. During turbine deployment the weight of the turbine times its moment arm around the deployment frame axis (the front box beam) is balanced by the fluid dynamic drag on the turbine times its moment arm. Therefore beyond a certain point in the ramp-up of tidal currents, this particular turbine would not fully descend into the locking position under its own weight. The one time this was encountered, the added weight of one person on each side of the deployment frame was sufficient to lower it all the way and lock it in deployment position.

Tasks at the end of a deployment occurred in the opposite order of deployment. The turbine would be extracted, and instrumentation would be shut down and removed from the water. All gear transiting to port on the R/V First Light would be packaged and upon signal the First Light would tie up alongside. Equipment and personnel would transfer to the First Light, the mooring line would be cast off from the test platform and the platform cast off to be towed behind the



support vessel. In the first two deployments, the increasing sea state made this task quite difficult, mainly due to the relative motion between the work platform and the support vessel. Higher sea states also made it more difficult to handle the platform during the tow back to port, especially with all the instrumentation mounts on the bow. On one occasion in sea state 3, the tow line snagged one of the instrument mounts and destroyed it.

#### 4.4.5 Data Collection and Results

Muskeget Channel was the most dynamic testing environment in this series of testing. Performing measurements proved far more difficult than in the laboratory or at the UNH-CORE Test Site. Table 3 is a snapshot of deployment specifics showing average nominal turbine performance during peak tidal current for each day of testing at the Muskeget Channel Test Site.

Measured platform drag loads were consistent with the ones measured during deployments at the UNH-CORE Test Site. The one minute averaged load cell data is shown in Figure 27. Note that on July 19<sup>th</sup> the dips are due to the anchor dragging. (On July 19<sup>th</sup> the platform was deployed on the flood tide,

**Table 3. Deployment specifics and average nominal turbine performance at the Muskeget Channel Test Site. Note: power coefficient calculated using rotor area.**

Date	Slack Time	Model	Peak Velocity [kts]	Mean Rotor Power [W]	$C_p$
15-Jul	9:15 AM	Stator-Rotor	2.6	261	1.12
16-Jul	10:00 AM	Rotor Only	3.1	413	1.07
19-Jul	5:45 PM	Rotor Only	3.8	482	0.67

whereas on July 15 and 16 the platform was deployed on the ebb tide, c.f. discussion re. anchor fouling below). The drag load can be compared to free stream velocity data in Figure 28 to see qualitatively that the increased sea state on July 16<sup>th</sup> resulted in higher loadings despite the increased free stream velocity on July 19<sup>th</sup>. The overall mooring loads at the UNH-CORE test site at comparable current velocities were higher than at Muskeget Channel, since there the support vessel Galen J was tied up alongside the test platform.

Measured tidal current velocities at Muskeget Channel are shown in Figure 28. Tidal current ramp up was not observed on July 15<sup>th</sup>. The window when wake measurements were performed, and the point at which the MEHT rotor cuts in are shown for July 16<sup>th</sup> and 19<sup>th</sup>. The data in Figure 28 is group averaged over 30 seconds.

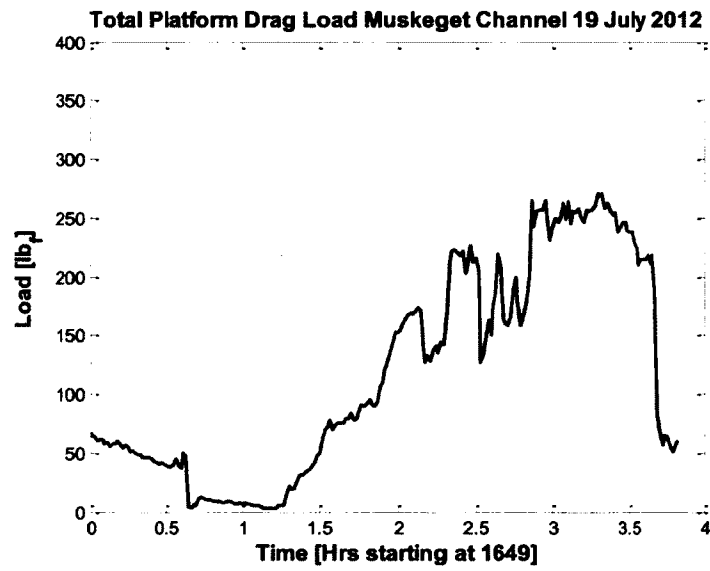
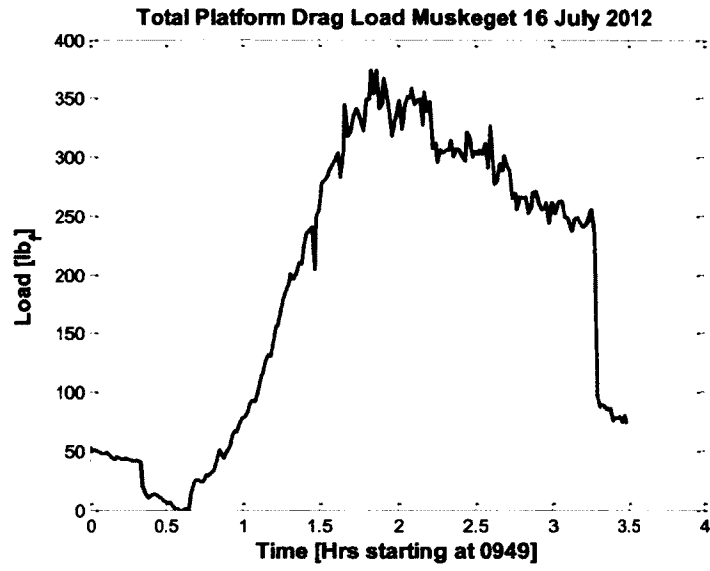


**Figure 27. Total platform mooring load at Muskeget Channel.**

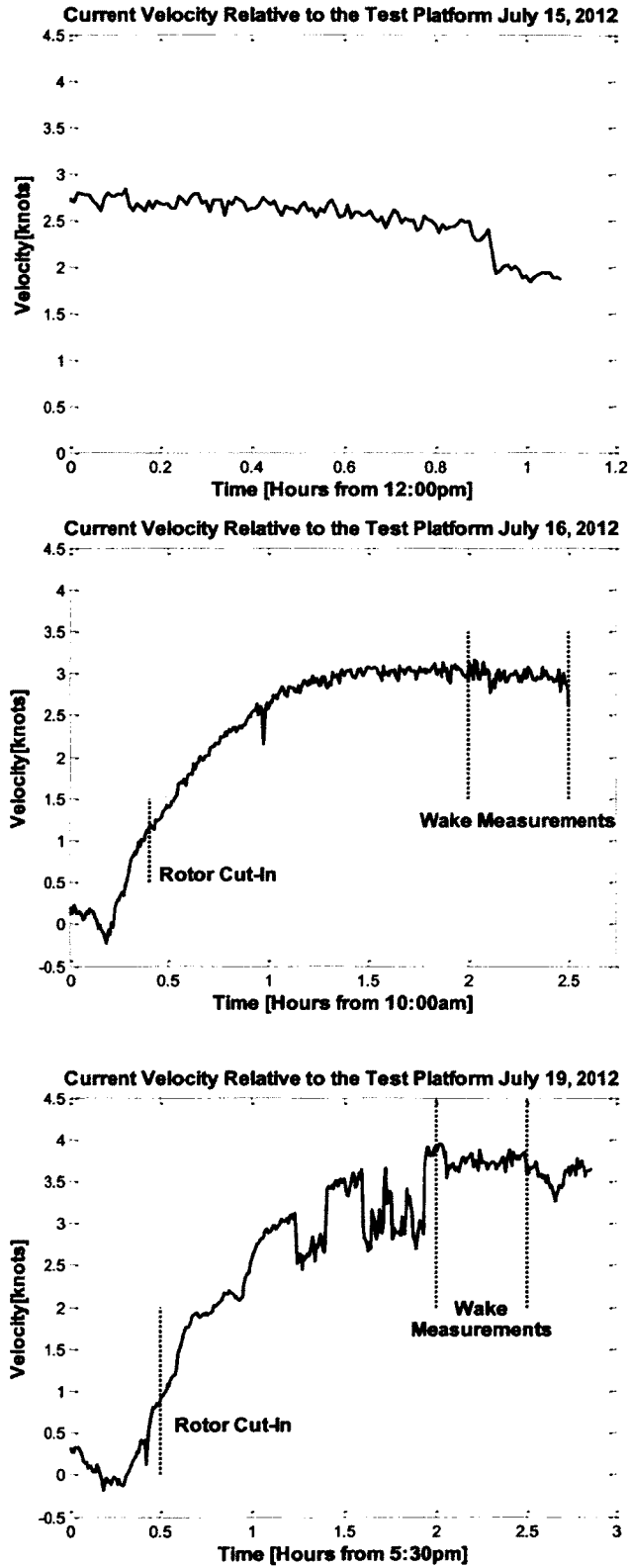
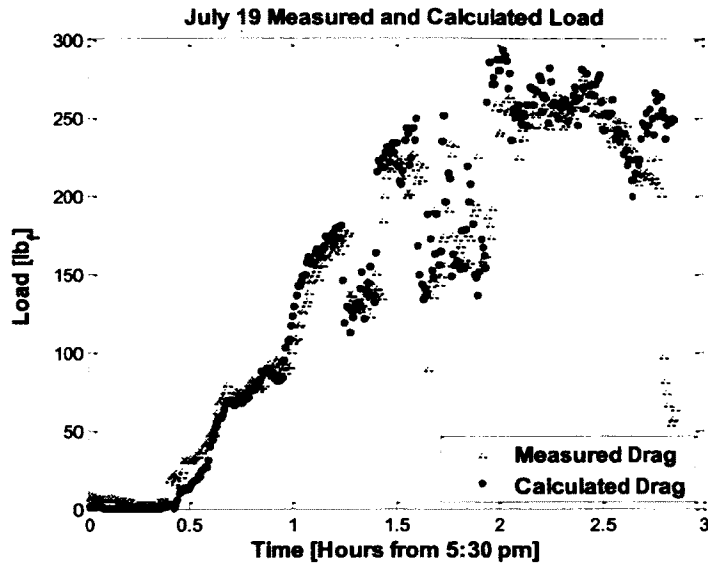


Figure 28. Tidal current velocity from MEHT testing at Muskeget Channel.

For these purposes, rotor cut-in is defined as the velocity at which a 30 second average of rotor power output is equal to 1 W or higher. Tidal energy sites with high velocities have a higher power density but are limited in number. Turbines that can extract energy at lower velocities are desirable for use at sites that have relatively low tidal currents. One knot is a low cut-in speed, but one should note that there is also comparatively little energy available for conversion at such a low velocity.

The plot of tidal current velocity on July 19<sup>th</sup> also shows the times and velocities when the anchor was dragging; they align well with the load cell data. Two main anchor dragging events occurred where the difference between measured (relative) fluid velocity and tidal current velocity was approximately one knot. The data also show that at 7:30pm the anchor set again, providing approximately one half hour of valuable testing at peak tidal current velocity.

As noted above, the drag area analysis performed with data from the UNH Test Site testing inherently included the drag from the Galen J, tied up alongside the platform. In an attempt to back out the load from the Galen J, the drag area of the test platform was calculated from the velocity and loading data collected on July 19<sup>th</sup>. The resultant drag area of the platform is  $0.005\text{m}^2$ . Therefore, the majority of the measured drag at the UNH test site was due to the Galen J support vessel. The comparison of measured drag to calculated drag for July 19<sup>th</sup> is shown in Figure 29.



**Figure 29. Calculated drag load based on drag area and tidal current compared to measure drag load.**

A half hour near peak velocity for each day was analyzed to determine the turbulence intensity of the inlet flow. Turbulence intensity is the ratio of the standard deviation of the fluctuating component of the velocity divided by the mean flow and is discussed in section 4.3.4.

The average turbulence intensity during the 30 minutes at peak velocity on July 19<sup>th</sup> was 9.6%. Qualitatively, the wind and wave environment the other two days at Muskeget Channel were significantly more active and is reflected in the results shown in Table 4. Note that this is turbulence “as seen by the turbine” or “as seen by the instrument”, in this case the Vector ADV mounted on the bow, which explains the high values on the days of significant wave action. Comparable studies with acoustic instrumentation in tidal energy sites have found turbulence intensities in the vicinity of 10% (Thomsom et al., 2012).

**Table 4. Inlet flow turbulence intensities for all MEHT tests.**

Date: Location	Turbulence Intensity
May 15: UNH	7.04%
May 16: UNH	7.40%
May 17: UNH	7.40%
July 15: Muskeget	24.15%
July 16: Muskeget	23.09%
July 19: Muskeget	9.64%

The increased turbulence intensity in Muskeget Channel may be responsible for a more rapid MEHT wake velocity deficit decay. Wake velocity data was not measured on July 15<sup>th</sup>, since tidal currents ramped up too quickly to safely deploy the ADV. By the time wake traversing was performed on the 16<sup>th</sup> the sea state was already too dynamic to obtain meaningful data with a platform-sting-mounted ADV. Figure 30 shows the non-dimensional wake velocities in the wake of the rotor-only model MEHT on the final day of testing, July 19<sup>th</sup>. The traversing ADV was positioned downstream of the turbine in 31 cross stream positions and 3 stream-wise positions. The probe was held at each cross stream location for 15 seconds. The data are averaged at each location to yield 31 data points across the wake of the turbine. Each data point is normalized by free stream velocity from the upstream ADV. The cross stream distance is normalized by shroud radius with negative values to port and positive values to starboard. Each wake profile is smoothed using a third order polynomial Savitsky-Golay smoothing filter with a frame size of 11 (Savitsky & Golay, 1964).

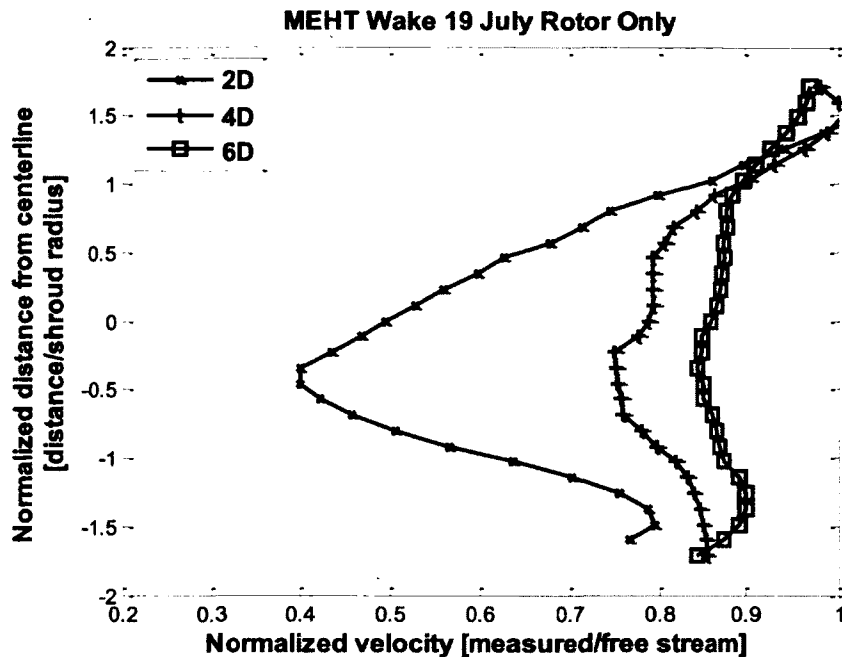


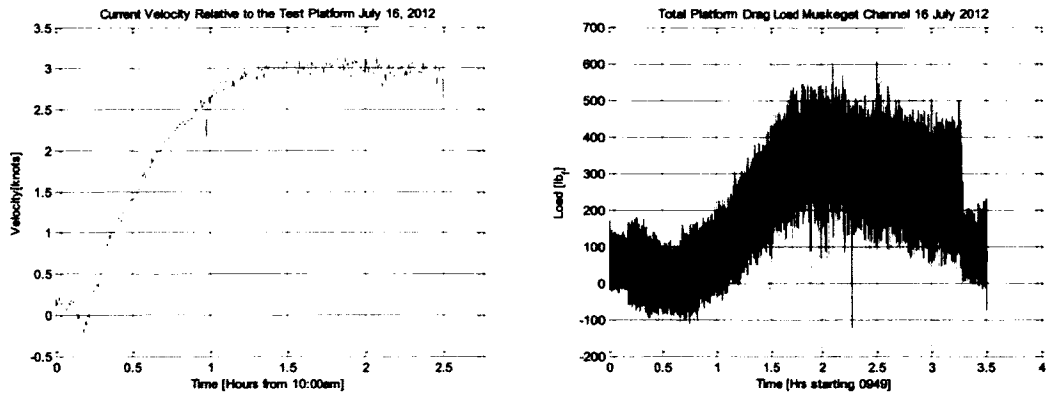
Figure 30. Wake velocities in Muskeget Channel.

The shapes of the curves in Figure 30 are as expected and comparable to previously recorded data. At 2D downstream the velocity near the centerline is 40% of free stream, compared to 30% at the UNH Test Site shown in Figure 23. At four shroud diameters downstream, nearly the entire wake has reached greater than 80% of the free stream velocity, and by 6 diameters it's in the proximity of 90% compared to 75% at the UNH Test Site. These results indicate a greater decay in velocity deficit as compared to testing at the UNH Test Site which supports the theory that greater inlet turbulence hastens wake recovery. The pronounced peak of the curve at 2D is comparable the rotor-only MEHT model tests at the UNH Test Site, shown in Figure 23.

The load cell analysis from testing at the UNH Test Site was not available in time to plan the mooring for deployments at Muskeget Channel, so the mooring was designed based on a UNH analytical model (Dewhurst, 2013). The



analytical model was built using a turbine drag coefficient of 1.3 provided by FloDesign based on high speed wind tunnel testing conducted on a comparable wind turbine design. The drag coefficients for the platform and turbine support frame were estimated based on geometry and size. The model output for sea state 1, or primarily current with no waves, was based on those approximations. The real merit in the model is in estimating loading with a free stream velocity and a wave forcing function. On July 16<sup>th</sup> the deployment was initiated at sea state 1, but during the deployment the sea state approached 3. The analytical model results provided the mean plus maximum fluctuation to represent a worst case scenario (Dewhurst, 2013). For accurate comparison of the model to the data, the load cell values are presented as recorded, without averaging, as shown in Figure 31. The free stream velocity is provided in 30 second group averages and is seen to reach greater than 3 knots at peak current. The unfiltered, raw load cell data shows loading peaks at maximum velocity of almost 600 pounds. From Figure 31 the predicted loading for a 3 knot current at sea state 2 is 570 pounds.



	Sea state 1 H=0	Sea state 2 H=1 ft (0.3 m), T=7.5 s	Sea state 3 H=2.9 ft (0.88 m) , T=7.5 s
1 kts (0.5 m/s)	55 lb (240 N)	80 lb (355 N)	150 lb (670 N)
2 kts (1 m/s)	213 lb (948 N)	290 lb (1300 N)	450 lb (2000 N)
3 kts (1.5 m/s)	490 lb (2175 N)	570 lb (2535 N)	750 lb (3345 N)
4 kts (2 m/s)	854 lb (3800 N)	975 lb (4340 N)	1210 lb (5385 N)
4.5 kts (2.25 m/s)	1005 lb (4470 N)	1220 lb (5420 N)	1470 lb (6540 N)

**Figure 31. Tidal current (top right) mooring load (top left) and analytical model mooring load results (bottom) at Muskeget Channel on July 16, 2012 (Sea State 2+).**

#### 4.4.6 Muskeget Channel Testing Conclusions

The most value from the Muskeget Channel deployments was gaining a first-hand understanding of the natural environment the turbine was deployed in. It was a major logistical achievement and all systems performed as expected. Given the success of the deployment it can be expected that MREC and the town of Edgartown will continue to research ways to implement tidal turbines at the Muskeget Channel site.

There were many lessons learned during these deployments, some should be mentioned for the benefit of future deployments: It is highly desirable to have fully time-synchronized measurements between all systems. While

setting all computer clocks to Universal Time Code (UTC) at the beginning of each deployment came close, it was not sufficient. We were able to synchronize in post-processing, e.g. by performing a cross-correlation with varying time offset between vertical velocity recorded by the Vector ADV and the change in pitch recorded by the IMU, times the distance to the Vector (moment arm), but it required significant additional effort. With the benefit of hindsight, a GPS timer with USB driver should have been purchased to synchronize computer time to GPS time for all data acquisition systems. A significant effort went into designing and fabricating instrumentation mounts that were modular and rugged. However, the many necessary field repairs and modifications resulted in time lost, and on occasion, questionable data. The design of the instrumentation mounts needs to be further improved to increase durability and simplify deployment and extraction.

#### **4.5 Testing in the UNH Tow Tank**

The tow mechanism of the tow and wave tank at the Center of Ocean Renewable Energy was renovated during the spring and summer of 2012. For this reason the FloDesign MEHT was tested in the UNH tow tank after the open water deployments, as opposed to the originally planned tow tank testing before the open water deployments. Shortly after the tank renovations were complete the MEHT was transported to Chase Ocean Engineering Laboratory (Chase). A total of eighty tows were conducted to collect drag and yaw loading data and measure inlet and wake flow velocities.

#### 4.5.1 Tow Tank Setup

The UNH tow and wave tank was originally designed and built in 1996 (c.f. Darnell, 1996, for design of original tow mechanism and carriage). It is a 36.6 m (120 ft) long, 3.66 m (12 ft) wide, 2.44 m (8 ft) deep facility. In 2012, the towing mechanism was renovated. The tow carriage, shown in Figure 32, now rides on linear bearings on 1 ¼" case-hardened Thompson Rails, driven by a toothed belt connected to an 11.9 kW Kollmorgen servo motor. It is capable of towing at speeds up to 3 m/s with a maximum acceleration of 2 m/s<sup>2</sup>. A detachable carriage frame can be attached to the main carriage at a variable distance so that instrumentation can be positioned at different locations downstream in the wake of the towed device. A flap style wave maker at one end is capable of producing waves with 1-5 second periods up to 0.4 meter wave height.

An adapter plate was fabricated (per drawing included in Appendix A.4) so

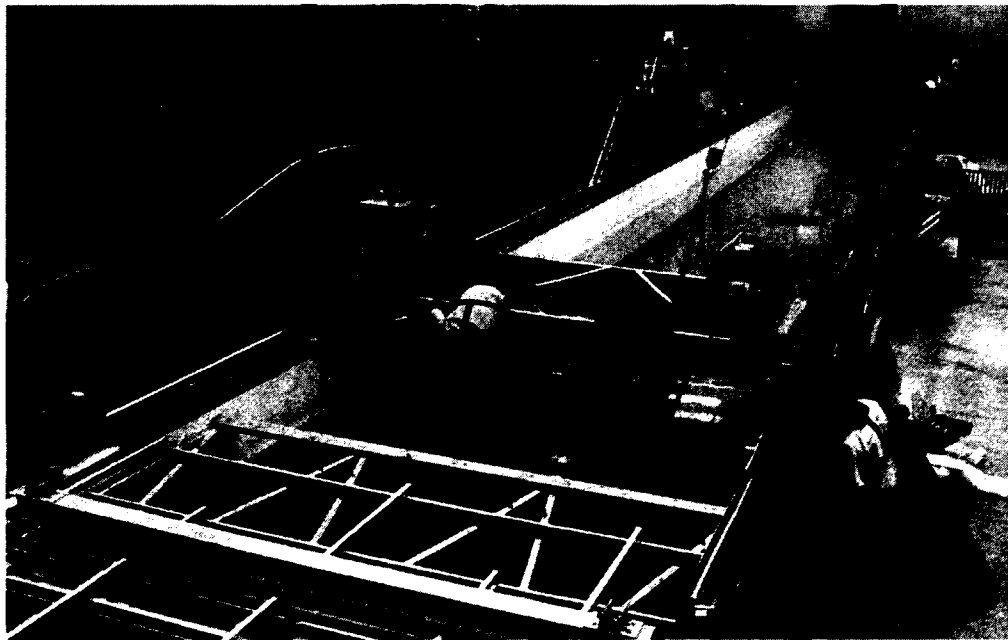


**Figure 32. Installing the tow frame to the carriage at the UNH Tow and Wave Tank.**

that the MEHT could easily mount to an existing hydrokinetic test bed. The frame of the test bed, shown with MEHT installed in Figure 33, was secured to the tow carriage at 4 points with pin fittings. The MEHT mounting adapter plate matched the bolt pattern on a shaft flange on the frame and the MEHT mounting surface. A shaft lock was installed on the vertical mounting shaft so that turbine alignment could be set while out of the water and maintained during installation in the tank. After installing the tow frame to the carriage a 3.2 kW Kollmorgen servo motor was mounted to the top of the vertical shaft and the shaft lock was removed. The original purpose of this servo motor in the turbine test bed was rotational speed control for cross-flow turbines, but it served well as a precise yaw positioning tool for the MEHT testing. Finite element analysis of the shaft that supports the turbine limited tow speeds to 1.1 m/s to avoid reaching 60% of the yield stress of the shaft. After installation, low frequency oscillations and displacements under light loading necessitated additional supports between

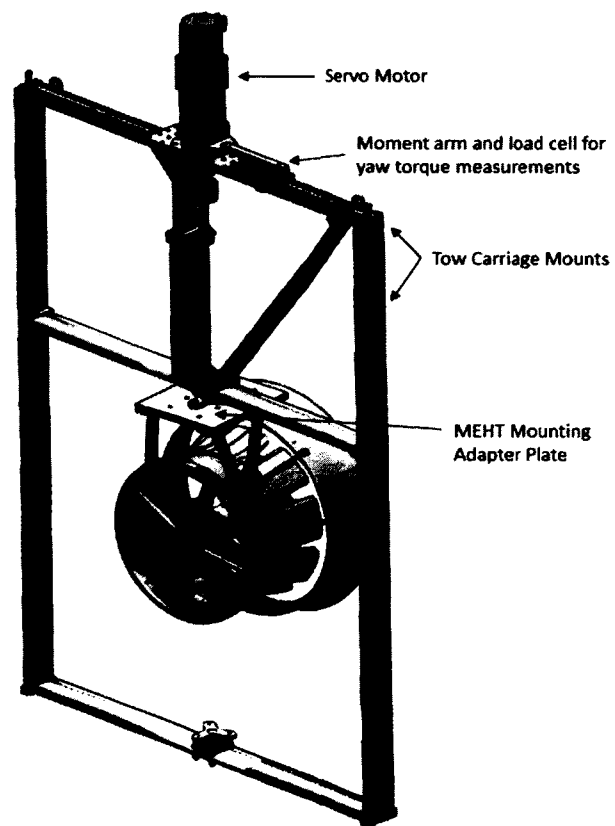


Figure 33. MEHT Mounted in UNH tow tank hydrokinetic turbine test frame.

the MEHT and the lower bearing in the frame. This modification improved stability and testing/tow speed was limited to 1 m/s.

#### 4.5.2 Tow Tank Test Plan

Following the Muskeget Channel deployments FloDesign designed and built a rudder that connects to the turbine center-body. The purpose of the rudder was to determine its potential influence on the yawing behavior of the MEHT. The test plan included collecting data on the stator-rotor model for drag, off-axis yaw loadings; and wake measurements and on the stator-rotor model with the rudder under yaw to measure its restoring forces.

The Vectrino ADV was used to measure inlet flow during the first series of runs in the configuration shown in Figure 34. The ADV was then repositioned to a BiSlide traversing system mounted to an assembly downstream of the turbine to measure wake velocities at the exit plane and 2 and 4 diameter downstream as seen in Figure 35. The BiSlide was centered on the turbine axis, so that 30 inches could be measured on either side of the turbine centerline. Two Sentran ZB3 series 500 pound load cells measured carriage drag load, location shown in Figure 34. The turbine assembly was gimbaled via a slewing

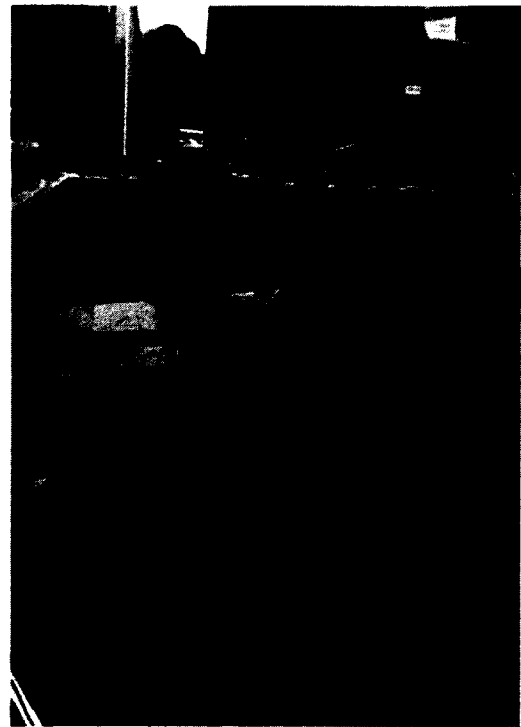


**Figure 34. MEHT configuration in UNH tow tank for free stream ADV measurements.**



**Figure 35. Tow tank wake traversing rig at 4D downstream.**

ring and a Sentran ZB3 series 200 pound load cell measured turbine yaw torque via a moment arm attached to the carriage, shown in Figure 33. FloDesign provided the load bank and power analyzer and VI to record turbine power data. A LabVIEW VI on the carriage control computer was used to record load cell data, carriage speed and position at sampling rate of 2 kHz. The LabVIEW VI also sends

a trigger to the ADV to commence recording at the beginning of each tow.

Tow tank testing was divided into 5 tasks, shown in Table 5. Each turbine model was tested initially at 0.5 m/s with no load and incrementally brought up to 1 m/s loaded. Acceleration and deceleration for all tests was set to  $0.5 \text{ m/s}^2$  to keep forces on the test bed and the turbine shroud low. The test plan was designed to minimize the number of times the turbine and wake measurement rig needed to be installed and removed from the tank. Yaw testing required rotating the turbine in 5 degree increments to plus and minus 20 degrees. Wake testing was performed only with the stator-rotor model, without rudder, to enable direct comparison to the open-water tests. The ADV was positioned at 2 and 4 shroud

**Table 5. Tow tank MEHT testing tasks.**

<b>Task</b>	<b>Description</b>
1	Shakedown - No Load
2	Shakedown - Load
3	Yaw
4	Rudder Stability - Load
5	Wake Testing

diameters downstream of the shroud exit plane with cross stream measurements taken every 4 inches. A near-wake profile was also captured at  $1/6D$ , or 0.167 shroud diameters downstream of the exit plane. The near-wake measurements started at the centerline and worked to one edge in one inch increments until the shroud was reached, and then in 2 inch increments for the remainder of the travel. Each shakedown speed, yaw position, and ADV position required an independent run. In all, 80 tows were performed.

#### 4.5.3 Tow Tank Wake Results

The tow tank wake measurements revealed several expected features and some unexpected features. Figure 36 is a plot of tow tank raw wake data at 2 and 4 shroud diameters downstream, measured in 4 inch cross-stream intervals. The unsmoothed plots are testament to the control afforded in lab testing not present in field testing. The profile shapes generally agree with prior flume and field testing. The turbine and frame blockage is approximately 10% of the tank cross-sectional area. By conservation of mass, the flow velocity will need to be greater than apparent free stream (tow) velocity on either side of the turbine frontal area to compensate for blockage. This effect is most pronounced in the 2D profile, but still apparent in the 4D profile.



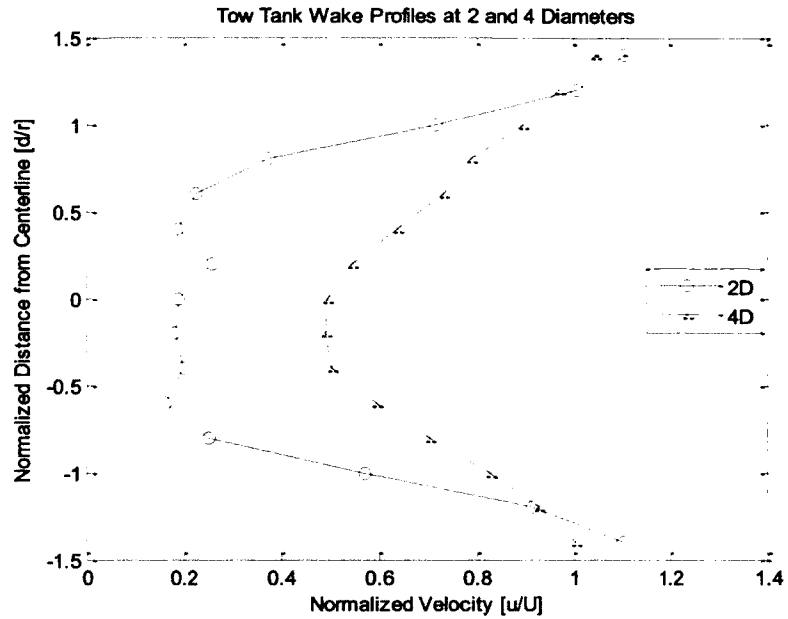


Figure 36. Tow tank wake profiles.

A phenomenon was discovered when streamwise velocity data at 0.167 diameters was plotted on top of the downstream profiles, shown in Figure 37. Only one half of the wake was captured so it can only be presumed that it would mirror in the opposite direction. The plot reveals that the streamwise velocity deficit is not yet at its maximum at the turbine exit plane and that velocity in the wake is further reduced at 2D downstream. The implication is that momentum is transferred between the exit plane and 2D downstream which is fascinating since all flow interference is upstream.

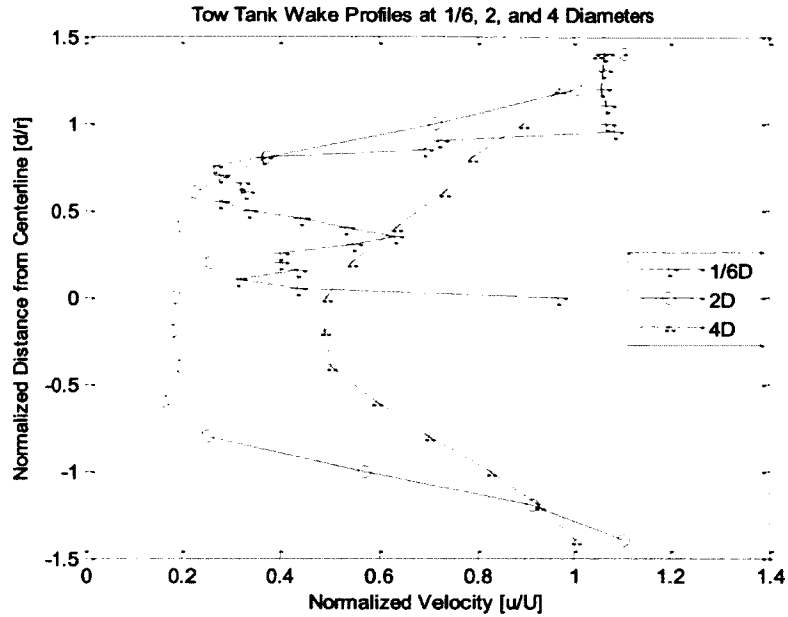


Figure 37. All tow tank wake profiles.

The momentum exchange can be explained with Figure 38 by comparing the  $x$ ,  $y$ , and  $z$  velocities between the  $x/d=0.167$  and  $x/d=2$  positions, where  $x$  is streamwise,  $y$  is cross-stream and  $z$  is vertical direction. Note that Figure 38 at  $x/D=0.167$  shows only half the wake. It can be seen that significantly more momentum is being carried in the  $y$  direction, and to some degree the  $z$  direction compared to Figure 39 which is a similar plot of the full wake at 2 diameters downstream. The profile at  $x/D=0.167$  captures the complex, three-dimensional flow coming out of the mixer and the ring-wing ejector. Further, the jet coming out of the open center body can clearly be seen, at  $x/D=0.167$  its maximum velocity is still near free stream velocity.

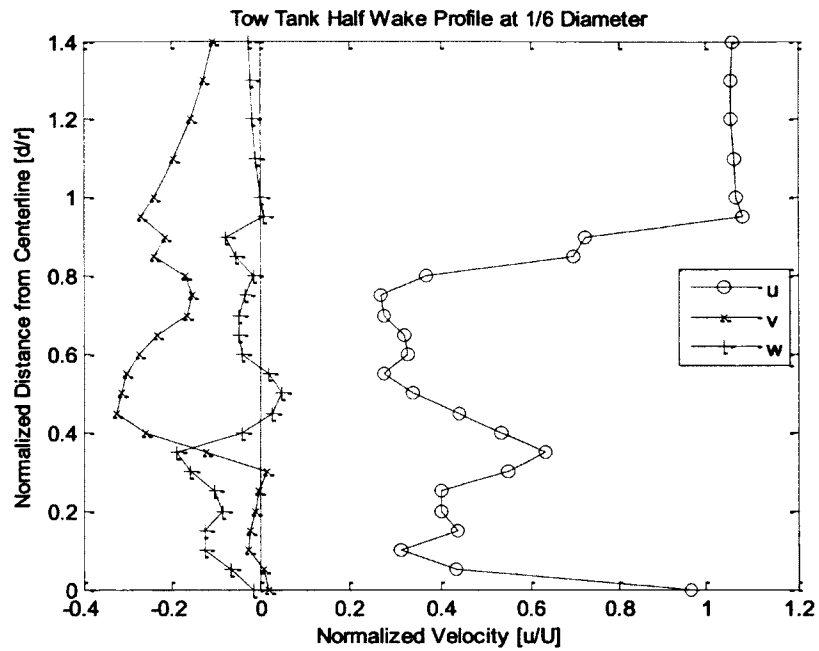


Figure 38. Half wake X, Y, Z velocity at 0.167 shroud diameters downstream.

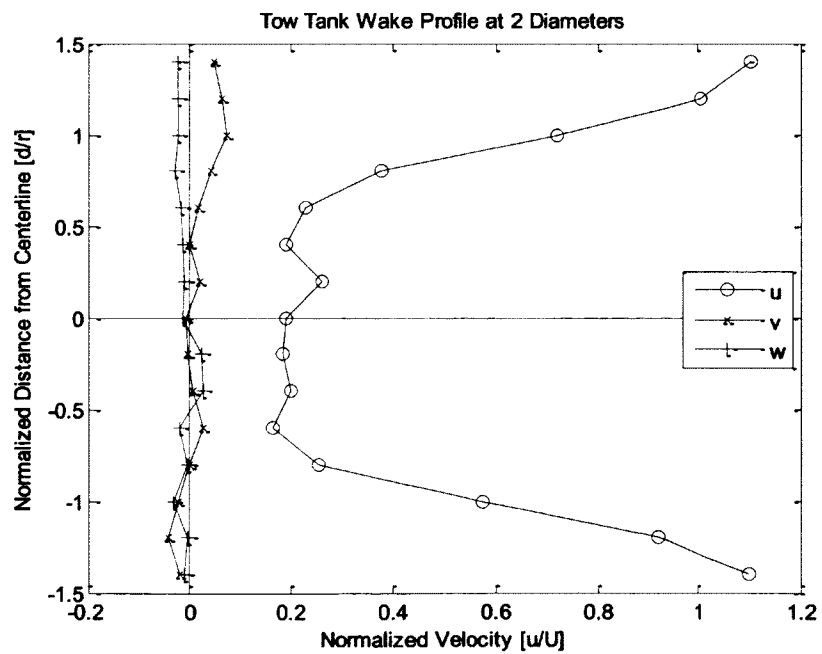


Figure 39. Full wake X, Y, Z velocity at 2 diameters downstream.

Momentum must be conserved in the wake of the turbine. Figure 38 and Figure 39 indicate that the momentum deficit in the y and z directions is transferred to momentum deficit predominantly in the streamwise (x) direction within 2 shroud diameters. It is possible that the rapid near wake lateral expansion and related pressure rise to the outlet pressure accounts for velocity slowdown in this region, similar to what happens in an un-shrouded turbine.

The turbulence intensity in the tow tank was determined by mounting the ADV to the front face of the tow carriage for the first 9 runs. The turbulence intensity was calculated from the standard deviation of the u-component of velocity filtered to remove data points outside of three standard deviations from the mean for each run. The average turbulence intensity of these runs is 7.3%. Subsequent work in the tow tank (cf. Bachant et al., 2013) found the turbulence noise floor in the vicinity of 2% and a marked improvement in the signal-to-noise ratio, from 5 to 12, with a higher concentration of seeding particles than was used for this testing. These results indicate that the measured turbulence was not a true representation of actual inlet turbulence during MEHT testing.

Wake profiles from open-water wake measurements indicated that wake velocity deficit recovered more quickly with increased free stream turbulence intensity. Figure 40 clearly shows a more rapid restoration of wake velocity for the rotor only model from the UNH test site to Muskeget Channel. Figure 41 is a comparison of the stator-rotor model between the UNH Test Site and the tow tank showing a reduced deficit at 2D at the UNH Test Site but a negligible difference further downstream (e.g. 4 shroud diameters). Taking the measured

turbulence in the tow tank as being artificially high supports the theory of an increased wake recovery with increased free stream turbulence but further research is required to quantify that correlation. For all cases the MEHT was operating at optimal tip speed ratio with respect to free stream velocity. Note that tow tank measurements are affected by blockage, whereas the open-water measurements are not.

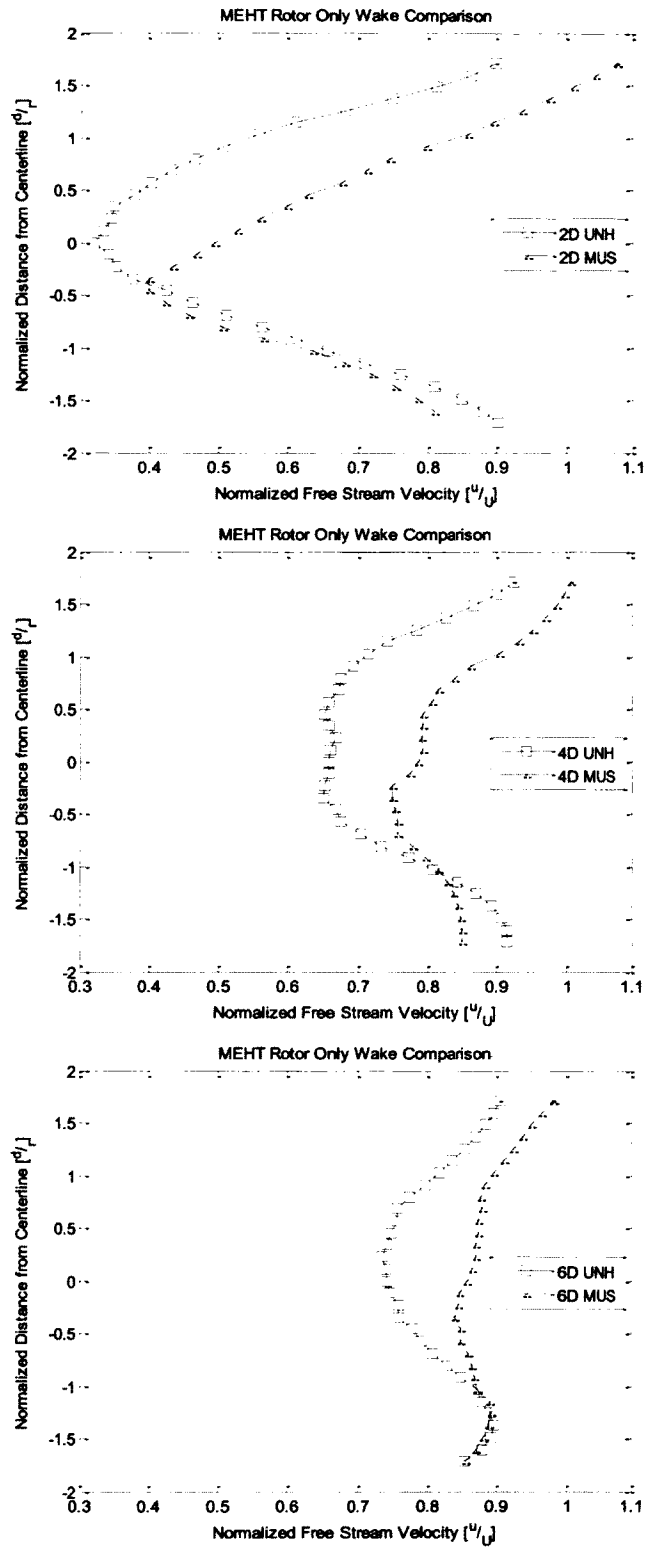
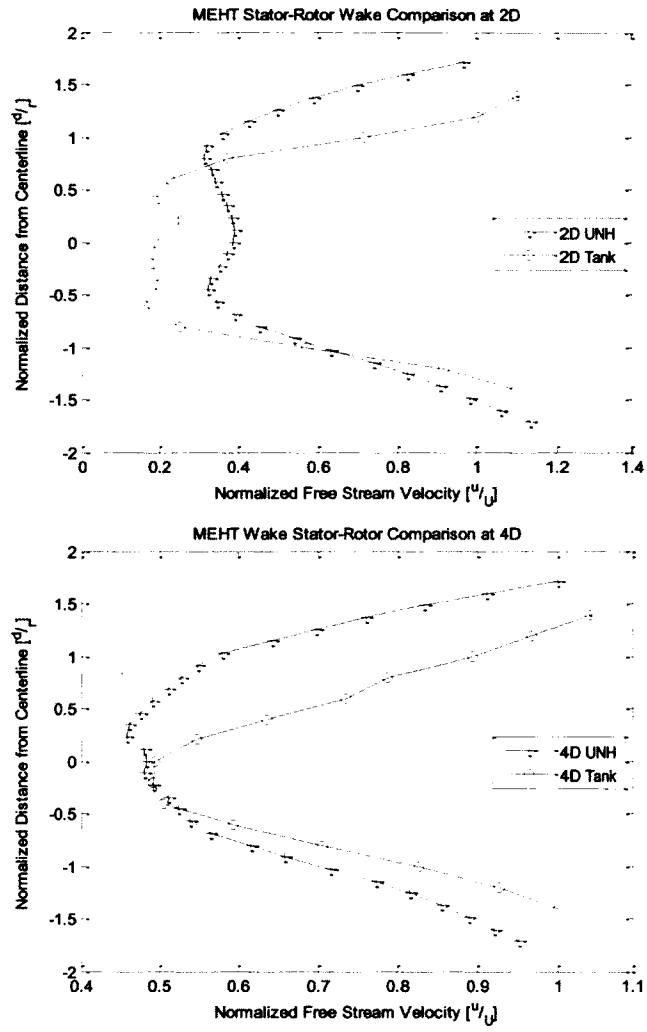


Figure 40. Wake comparison of MEHT Rotor-only operating at optimal tip speed ratio between May 16<sup>th</sup> (UNH Test Site) and July 19<sup>th</sup> (Muskeget Channel) at 2D (top), 4D (middle) and 6D (bottom) downstream.



**Figure 41. Wake comparison of MEHT Stator-Rotor operating at optimal tip speed ratio between May 15<sup>th</sup> (UNH Test Site) and tow tank at 2D (top) and 4D (bottom) downstream.**

#### 4.5.4 Tow Tank Drag and Yaw Results

The tow tank testing provided unique opportunities to measure MEHT characteristics that could not be measured during open water testing. The frame that supports the turbine is mounted on linear bearings so that the total streamwise drag can be measured. When the frame tare drag is subtracted, the turbine drag, or thrust, can be obtained. The shaft that supports the turbine has a lever arm connected to a load cell so that yaw torque can be measured for any inlet flow orientation.

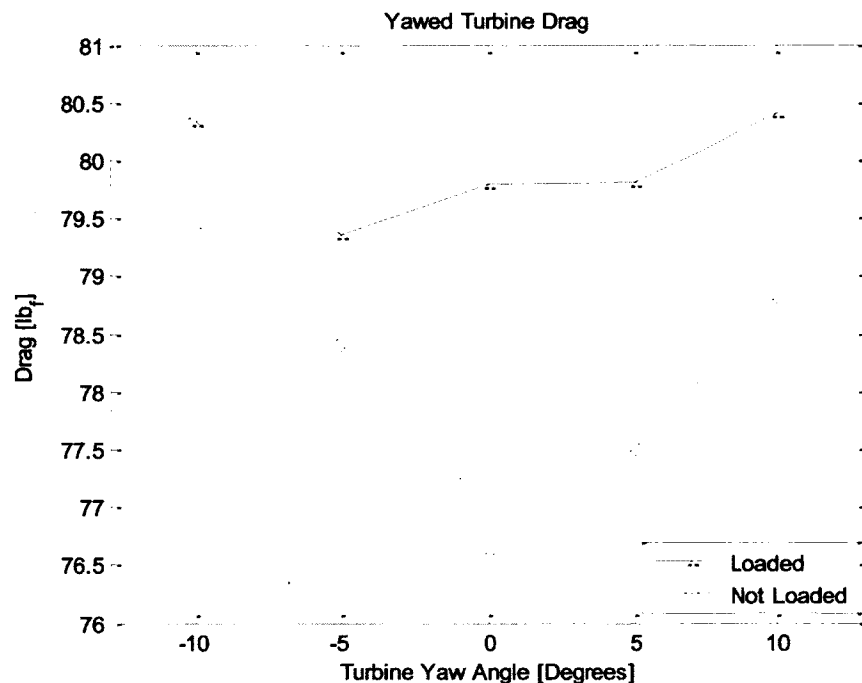


**Figure 42. MEHT yawed drag, rotor loaded v. rotor unloaded.**

The mean drag load for the turbine, both loaded and unloaded, yawed from -10 degrees (counter clockwise) to +10 degrees (clockwise) with frame tare drag removed is shown in Figure 42. The shift between the two data sets is due to the added thrust force of the rotor extracting energy from the flow. The data



shows that the axial load on the rotor is very small and that the majority of the thrust is on primary and secondary shroud, as derived by Werle and Presz (2008, 2009). The drag load also increases as the turbine is yawed, although the change in drag per yaw position is less for the loaded rotor runs than for the unloaded rotor runs. This is likely due to the combination of change in frontal area, drag coefficient and turbine efficiency. Future design processes can be simplified by lumping the change into the coefficient of drag, by finding it experimentally for the loaded turbine operating at optimal tip speed ratio at each yawed position, as shown in Figure 43. Open water and tow tank turbine support infrastructure was designed using a drag coefficient of 1.3 which was expected, and now confirmed, to be a conservative estimate compared to a measured drag coefficient of 1. This also means that the MEHT rotor could be designed a bit more aggressively to increase the turbine's overall thrust coefficient, and thereby energy extraction from the flow.

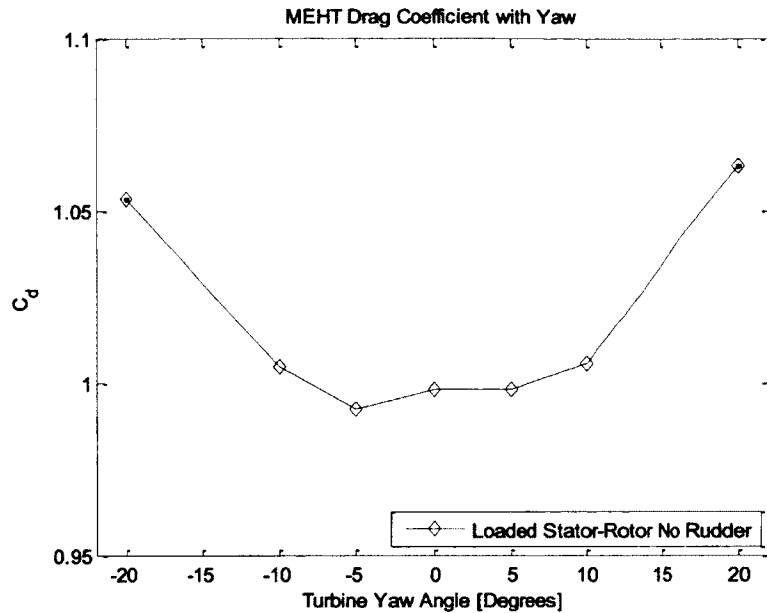


**Figure 43. Drag coefficients for yawed rotor loaded turbine.**

A motivating factor for FloDesign to pursue tow tank testing following the open water testing was the opportunity to measure the effect of a newly designed rudder shown installed on the MEHT in Figure 44. The design goal of the rudder was to eliminate the need for active yaw control. The effect of the rudder is quantified by comparing the torque exerted by the loaded stator-rotor model operating at optimal tip speed ratio yawed from -20 to +20 degrees in 5 degree increments, with and without the rudder installed. The results of this comparison are shown in Figure 45. For the case where the turbine is yawed in the clockwise direction (+) the positive torque value reflects the load acting in the counterclockwise direction. The results are linear with consistent values at each yaw position. The differences between the no-rudder and rudder yaw data are small. The implications are that the rudder was installed in a location where the turbine had already sufficiently reoriented the flow to be in line with its axis.

Should the righting moment of the turbine without the rudder be found insufficient and a rudder be necessary, it might be more appropriately placed to greater effect outside of the direct wake of the turbine.

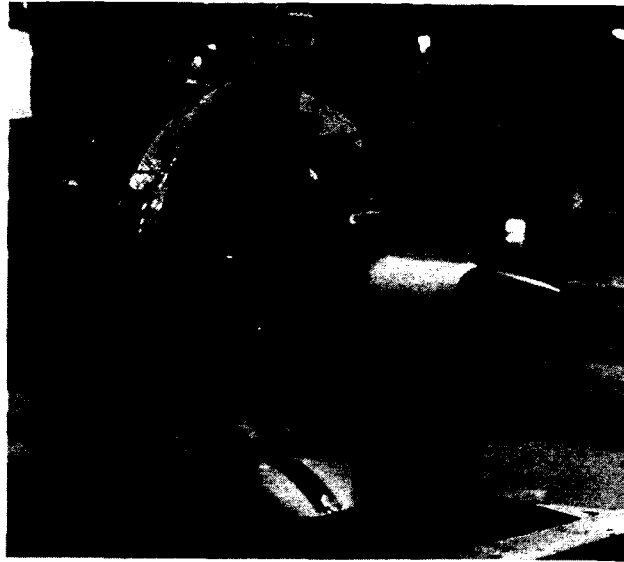


Figure 45. MEHT with rudder.

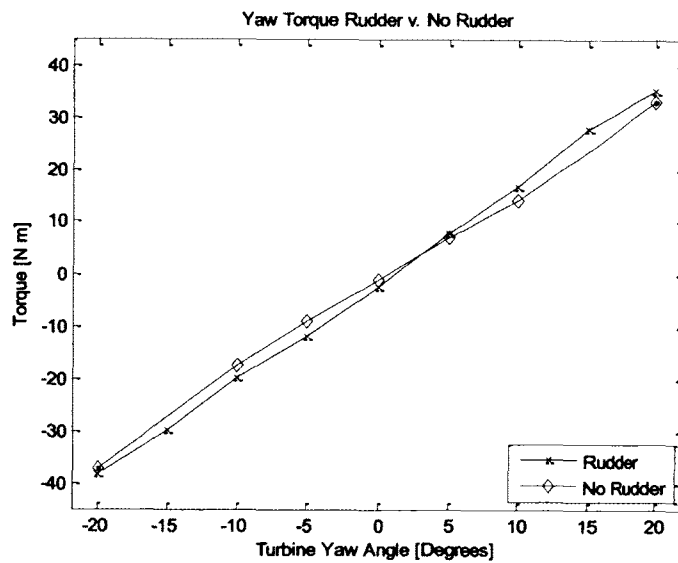


Figure 44. Yaw torque with and without rudder.

#### 4.5.5 Tow Tank Conclusions

Tow tank testing was originally planned to take place before the open-water deployments, but due to tow mechanism renovation was not performed until after the open-water deployments. Laboratory tests should come before open-water deployments, and the results from tow tank testing would have been valuable to plan for the open water tests.

Tow tank tests that were part of the original test plan, as well as additional tests, were performed. The clean wake results from the tow tank were compared to open water tests, and greater detail in the momentum transfer was discovered in the near wake. The turbine drag (thrust) coefficient was determined experimentally and differences were observed with changing yaw angle. The impact of a new MEHT rudder on yaw torque was quantified and compared to the MEHT model with no rudder. The differences were found to be very small, providing guidance for improved rudder placement in future designs. This concluded the experimental evaluation of the FloDesign MEHT at the University of New Hampshire.

## 5 Materials Testing

In parallel to the experimental evaluation of the MEHT, coupons of the materials used to build the turbine were deployed at the UNH Pier in New Castle, NH to assess corrosion and biofouling effects.

### 5.1 Overview

Corrosion is the exchange of electrons between a metal and its environment. This exchange of electrons changes the material both electrochemically and physically (McCafferty, 2010). Biofouling is the accrual of an unwanted biological community at an interface (Durr, 2010). Submerged equipment is subject to both corrosion and biofouling which can lead to detrimental effects on performance.

The UNH pier facility in New Castle N.H. enables deployment of samples of material, or coupons, and has a history of materials testing, which to date has focused on copper alloys with an emphasis on aquaculture (Drach *et. al.*, 2012) (Greene & Grizzle, 2007). The experimental evaluation of the MEHT was complemented by deploying select materials, with and without protective coatings, which are currently used in the turbine design or are candidates for inclusion in future turbine design.

The material and coating selections were chosen by FloDesign based on current and

**Table 6. Material selection for corrosion and biofouling study.**

1	Electroless Nickel (EN) plated A-36 Steel
2	Anodized 6061 Aluminum
3	316 Stainless Steel
4	6061 Aluminum
5	A-36 Steel
6	A-36 Steel - ePaint
7	EN plated A-36 Steel - ePaint
8	6061 Aluminum - ePaint
9	Hydrophobic Cast Urethane

prospective turbine component material selections. The coupons were fabricated and coated prior to delivery to UNH. Table 6 provides the material selection and treatment. Surface treatments include: electroless nickel (EN) plating, anodizing, and two selections of marine paint developed by ePaint. Four identical panels with coupons of each material were deployed for one year in Portsmouth Harbor tidal waters. An increasing number of panels was withdrawn quarterly to capture changes in corrosion rate and seasonal effects of biofouling.

## **5.2 Introduction to Corrosion**

Corrosion is the destructive attack of a metal by its reaction with the environment (McCafferty, 2010). It is an electrochemical process, meaning that the reaction is not direct, but rather it occurs through coupled half-cell reactions. This can be explained through observation of electron movement in anodic and cathodic reactions. In an anodic reaction the metal oxidizes, or transfers electrons to its environment. This transfer of charge is often accompanied by a transfer of mass. This concept is used to develop the more scientific definition of corrosion as the simultaneous transfer of mass and charge across a metal/solution interface (McCafferty, 2010). The opposite of the anodic reaction is one in which the oxidation number of a metal is reduced, meaning that electrons are gained at the site. This process is a cathodic reaction.

The link between the charge transfer and the transfer of mass is the Faraday (F), defined as the charge transfer in coulombs per the equivalent electron transfer,

$$F \equiv \frac{96,500 C}{\text{equivalent}} \quad (5.1)$$

Faraday's law states that the mass of metal corroded ( $w$ )

$$w = \frac{ItA}{nF} \quad (5.2)$$

where  $I$  is current in amps,  $t$  is time in seconds,  $A$  is the atomic weight of the metal in grams per mole and  $n$  is the number of equivalent electrons transferred per mole of metal (McCafferty, 2010).

Corrosion rate units are often expressed in terms of corrosion current density (i.e.  $\mu A/cm^2$ ) or in penetration rate (i.e. mils per year (mpy) where 1 mil = 0.001 inches). By measuring the mass loss of a corroding metal the penetration rate can be calculated from known material properties such as density and atomic weight. With a known penetration rate the corrosion current density can be calculated with the definition of the Faraday. Conversely, in special test facilities, the corrosion current can be measured and used to calculate penetration rates. For this study the mass loss was recorded and corrosion reported in terms of penetration rate in mils per year.

Corrosion can be categorized as either uniform or localized. In uniform corrosion the metal is attacked over the exposed surface area, whereas with localized corrosion the attack is focused in one location. The mechanism for both is still based on the balance of half-cell reactions as stated above, but with uniform corrosion the reaction moves along the entire surface area (McCafferty, 2010). With localized corrosion the anodic and cathodic reactions become fixed in location. The three most prevalent examples of localized corrosion include pitting, crevice corrosion, and stress corrosion cracking. For this report, uniform

corrosion will be quantified by mass loss and in most cases localized corrosion will only be qualitatively reported based on visual inspection.

### **5.3 Introduction to Biofouling**

The foundation of engineered biofouling control is rooted in the shipping industry (WHOI, 1952). Early examples include lead and copper sheathed hulls from the 18<sup>th</sup> century and developed into cuprous oxide paint and coatings (WHOI, 1952). The negative side effects of the latter on aquatic life, coupled with an increasing need for global shipping makes this field of research ripe with opportunity. The following will serve only as a cursory overview of the topic to provide justification for the biofouling aspect of the materials testing.

There are several mechanisms by which aquatic life can adhere to submerged bodies and even more factors that will influence their success. The most common process is a combination of non-vegetative, or sexual, reproduction and asexual, or dispersive, spread (Durr, 2010). Dispersive spread is a fascinating ability of some marine life to regenerate fully following fragmentation (e.g. cleaning an afflicted mooring line may exacerbate biofouling because each new fragment may potentially reattach and grow) (Durr, 2010). The mechanism of sexual reproduction is species specific and falls into one of three categories; internal fertilization, spermcasting, or broadcasting. Internal fertilization requires direct coupling of male and female, whereas spermcasting is the release of sperm into the water to fertilize eggs still retained by the female, and broadcasting is the free release of both sperm and egg (Durr, 2010). Once the egg is fertilized the process of settlement of the species and subsequent



success depends on a wide range of variables including but not limited to: temperature, presence of predators, salinity, water current velocity, available food, light for photosynthesis (species specific), available space and opportunity for reproduction. Biofouling mitigation, or prevention, depends on interrupting any step in the complicated process of aquatic reproduction.

Existing biofouling mitigation techniques are wide ranging within three primary categories; biocidal coatings, non-biocidal coatings and other alternatives. Biocidal coatings can be broken down further into contact leaching, soluble matrix, and self-polishing techniques, each of which have their own cost, effectiveness and environmental impact. Non-biocidal coatings have been commercially available since 1995 with the introduction of silicone foul release coatings (FRC) (Durr, 2010). Although considered a commercial success story, fluoropolymer FRC's are now competing with silicone-based FRC's on a performance and cost basis (Durr, 2010). Foul release coatings are most effective for applications in which high speed (greater than 30 knots) and high activity (moving greater than 50% of the time) will induce frequent dynamic loadings on the growth which, due to the low mechanical interlocking of the organism, will cause them to fall off. Other alternative forms of biofouling mitigation techniques that have been researched include: electricity, magnetism, sound, heat, radiation and automated mechanical scrubbing.

There is not yet a method of biofouling control that simultaneously meets the criteria of being highly effective, having low cost, and having low environmental impact. With developed nations trending toward tighter

environmental controls, and shipping fuel costs trending higher, the market exists for further development. Furthermore, biofouling research is still centered on the shipping, oil and gas, and aquaculture industries and has yet to fully impact the nascent marine renewable energy industry. This project is therefore a unique opportunity to apply existing biofouling control products to materials specifically intended for use in the hydrokinetic turbine industry.

A selection of novel patented biofouling prevention products from Falmouth, MA based ePaint were applied to 3 of the selected materials: steel, electroless nickel plated steel and aluminum. The “Ecominder” and “EP-2000” products were each applied to two coupons of each material. The mechanism by which the ePaint products perform can best be described by the following statement from a 2011 white paper based on a case study conducted in Connecticut.

All ePaint antifouling and foul-release coatings feature a proprietary photo-active technology unique to ePaint products. In a nutshell, this process utilizes energy from blue and green light scattered throughout the water column to combine water and dissolved oxygen generating minute levels of hydrogen peroxide around the hull. The hydrogen peroxide creates an inhospitable surface which effectively deters the settling of the hard shell-type larvae from attaching. This process also helps the paints to wear smoother surface over time, reducing friction and preventing heavy build-up of old paint. The hydrogen peroxide generated is short lived and instantaneously breaks back down to water and oxygen when washed from the hull. (ePaint, 2011)

The goal of this biofouling research is to quantify the biological growth in Portsmouth Harbor tidal waters on a variety of materials with and without biocide-free protective coatings.

#### 5.4 Materials Testing Procedure

Standard practice for materials testing in seawater is outlined in the American Society for Testing Materials (ASTM), chapter G01-03. A one-year trial with quarterly analysis was chosen to provide sufficient time for corrosion rates to stabilize and to provide insight into the seasonal effects of biofouling and effectiveness of the coatings.

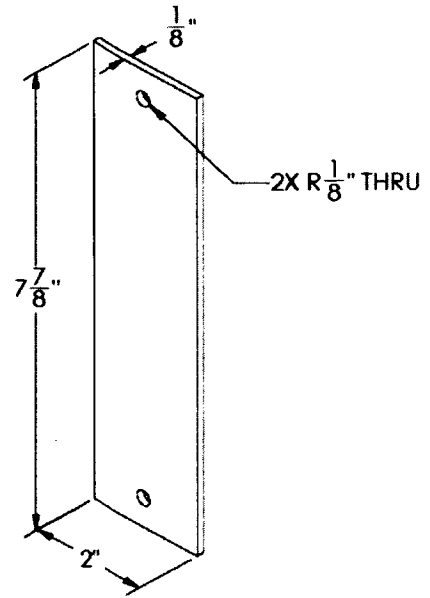
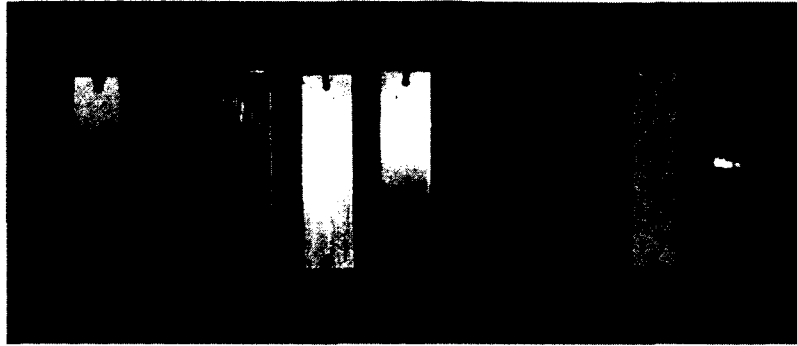


Figure 46. Coupon geometry.

FloDesign fabricated coupons according to the drawing in Figure 46. At UNH they were stamped with markings A-D, to indicate what panel they would be mounted to, and 1-9 to indicate their material per Table 6. All uncoated samples were degreased with isopropyl alcohol. The coating manufacturer, ePaint, directed that contact with any chemical would potentially destroy its performance so no chemical contact was permitted throughout the project. Each coupon was weighed, photographed, and then mounted to four identical test panels, one of which is shown in Figure 47. To minimize any undesired molecular interactions, plastic zip ties were used to secure the coupons to the test frames. The rectangular test frames were built out of 1.5 inch schedule 40 PVC pipe with 90 degree elbows glued at each corner. A one quarter inch hole was drilled in the top and bottom to allow water to fill the tube, and air to escape. This eliminated frame buoyancy and assured the frames



**Figure 47. Coupon test frame, 1 of 4, prior to seawater submersion.**

would remain submerged. The frame was coated in an anti-fouling paint to limit growth on the frame from influencing the growth on the coupons.

To accommodate quarterly analysis, the four identical panels were deployed in an arrangement that allowed sequential removal of individual panels without disturbing the panels that were intended to stay submerged. The panels were secured to an existing floating frame under the UNH pier such that the top of each panel was 18 inches below the water surface, in the photo-active zone. All four panels were deployed on January 17, 2012. Table 7 summarizes the panel recovery schedule. After removing biological growth, and cleaning and weighing the coupons at each recovery they were reattached to the panel and returned to the test site.

Each panel was photographed at the pier upon removal from the water. They were then placed in a tub of seawater for transportation to the

**Table 7. Coupon deployment and recovery timeline.**

Date	Action
17 January, 2012	All frames Deployed
24 April, 2012	Frame A recovered
26 July, 2012	Frames A & B recovered
22 October, 2012	Frames A, B & C recovered
15 January, 2013	All Frames Recovered

laboratory for analysis. For the first recovery, only corrosion cleaning and weighing was performed, from that point onward, the panels were delivered directly to Jackson Estuarine Laboratory (JEL) for biological growth removal prior to corrosion analysis and weighing.

Scientists at JEL removed each coupon from the frame and photographed prior to cleaning. Each sample was then cleaned of the biological growth. The growth from each sample was rinsed to remove sediment and weighed yielding the total washed wet weight. The growth was bagged and frozen to allow for future species classification and the coupons made available for corrosion analysis.

Corrosion analysis was performed in the Hewitt Annex materials lab on the UNH campus and once in a hood at JEL. The cleaning procedure started with light nylon bristled brushing in distilled water to remove any remaining biological remnants. Samples coated with ePaint were then dried and prepared for weighing, while uncoated coupons were cleaned in a chemical solution per

**Table 8. Chemical cleaning instructions. (Taken from ASTM G1.03)**

Material	Solution	Time	Temperature	Remarks
Aluminum and Aluminum Alloys	Nitric Acid (sp. Gr. 1.42)	1 to 5 min	20 to 25 °C	Remove extraneous deposits and bulky corrosion products to avoid reactions that may result in excessinf removal of base metal.
Iron and Steel	500 mL of Hydrochloric Acid (sp. Gr. 1.19) 3.5g hexamethylene tetramine Reagent water to make 1000mL	10 min	20 to 25 °C	Longer times may be required in certain instances
Nickel and Nickel Alloys	150 mL of hydrochloric acid (sp. Gr. 1.19) Reagent water to make 1000mL	1 to 3 min	20 to 25 °C	None
Stainless Steel	100 mL of Nitric Acid (sp. Gr. 1.42) Reagent water to make 1000mL	20 min	60 °C *	None

\*Temperature exceeds capabilities, samples allowed appropriate time at 20 to 25 °C

ASTM G01-03.

Table 8 summarizes the chemical cleaning guidance from ASTM G01-03 for the applicable materials in this study. After the prescribed time in the chemical bath the coupons were transferred to a water bath for chemical removal then removed and hot air force-dried. When dry, all coupons were weighed on the same triple beam balance (0.1g resolution). The mass loss for all panels was converted to a uniform corrosion rate expressed in the units of thickness per year:

$$\alpha = \frac{\Delta m}{\rho \cdot A} \cdot \frac{365}{K} \quad (5.3)$$

where  $\Delta m$  is the mass loss in grams of the specimen,  $\rho$  is the specimen density in  $\text{g/cm}^3$ ,  $A$  is the initial surface area of the specimen in  $\text{cm}^2$  and  $K$  is the exposure duration in days. For all except the very last removal and cleaning, the coupons were then re-connected to the test frame and returned to the test site.

## **5.5 Materials Testing Results**

### **5.5.1 Quantitative Corrosion Results**

The mass of coupons from panel A, which were weighed initially and every quarter thereafter, is shown in Figure 48.

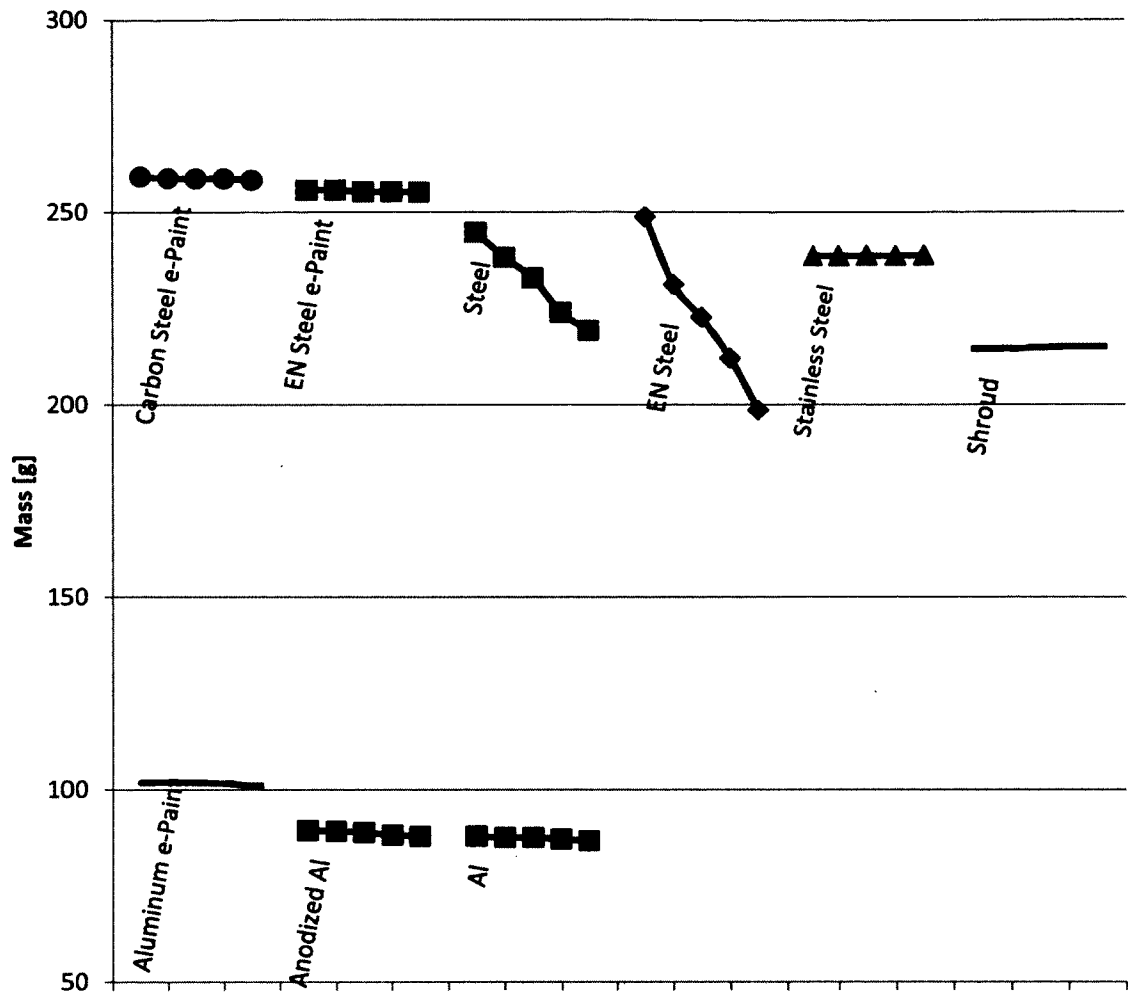


Figure 48. Panel “A” coupon mass over 1 year measured initially and quarterly thereafter.

Table 9. Average mass loss and apparent corrosion rate for each material and coating.

Material	Average Mass Loss [%]	Average Apparent Corrosion Rate [mpy]
EN Steel	20.2	74.8
Anodized Al	0.9	3.4
Stainless Steel	-0.1	-0.2
Aluminum	1.0	3.8
Steel	8.4	31.0
Carbon Steel ePaint	0.5	1.7
EN Steel ePaint	0.5	1.7
Aluminum ePaint	1.5	5.5

Table 9 shows the average percent mass loss by weight and average apparent corrosion rate in mils per year (mpy) (1 mil = 0.001 in) of all of the samples of each material and coating. Three of the four EN steel samples fell from their respective test panel due to excessive corrosion at the mounting holes. It is shown that the one recovered EN steel sample performed poorly in comparison to untreated steel. It stands within reason that a galvanic cell was established between the plating and substrate in locations of weaker plating (e.g. sharp corners and holes). Stainless steel performed very well and little difference was discernible between aluminum and anodized aluminum. There is a marked decrease in corrosion rate for both steel and EN steel coated with ePaint. The relative mass loss of the aluminum coated in ePaint compared to uncoated aluminum may be explained by wear of the paint rather than corrosion of the substrate.

**Table 10. Comparison of the four steel samples.**

Steel		
Panel	Average Mass Loss [%]	Average Corrosion Rate [mpy]
A	10%	39
B	9%	33
C	7%	26
D	7%	27



Table 10 is a comparison of the four untreated steel samples indicating that corrosion rate increases with biomass and corrosion product removal frequency. Overall corrosion rates are higher than those published from a Woods Hole Oceanographic Institute study in 1972 in which a corrosion rate of 10 to 15 mpy for AISI 1020 steel in surface waters over the first year was reported (Dexter, 1972). This example highlights the value in testing specific materials at designated sites due to inherent differences in materials and water chemistry and the subsequent effects on corrosion rates.

A comparison between both ePaint products and uncoated coupons after one year of submersion is provided in Table 11. Some coupons included in this study were removed throughout the year and cleaned of biomass. Coupons were not weighed prior to coating therefore it is not possible to determine error introduced by changing mass due to paint wear and ablative effects versus mass loss of the substrate. Despite these unknowns, Table 11 clearly shows the effectiveness of using either Ecominder or EP-2000 to inhibit corrosion and shows a slightly better performance for the Ecominder coating. The exception is aluminum with EP-2000 which shows no visual sign of corrosion induced mass loss.

**Table 11. Comparison of bare material to ePaint coatings after one year of submersion.**

Material	Average Corrosion Rate [mpy]
Bare Steel	31.0
Steel & Ecominder	1.1
Steel & EP-2000	2.4
EN Steel	74.8
EN Steel & Ecominder	0.9
EN Steel & EP-2000	2.5
Aluminum	3.8
Aluminum & Ecominder	3.2
Aluminum & EP-2000	7.8

### 5.5.2 Qualitative Corrosion Results

Severe localized corrosion of the EN plated steel resulted in significantly more mass loss compared to the uniform corrosion in untreated steel as seen in Figure 49.

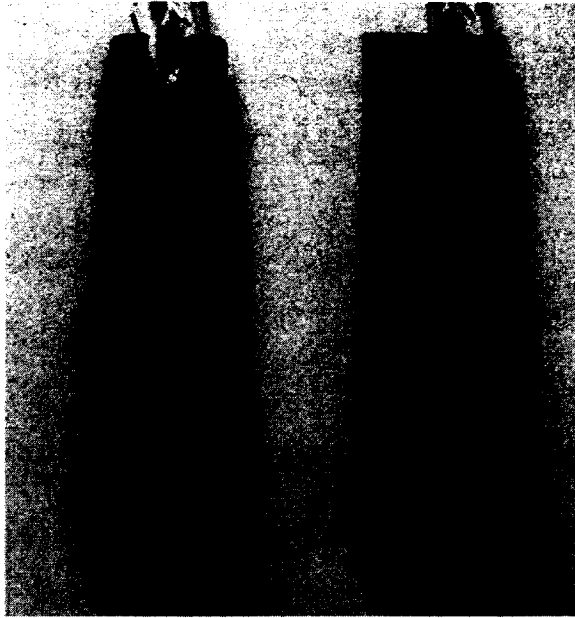


**Figure 49. Comparison of EN plated steel (left) to untreated steel (right) after one year of submerged exposure (from panel A).**

The comparison of corrosion rate by analysis of mass loss for aluminum resulted in no discernable difference when anodized. It is shown in Figure 50 that the anodizing does protect against localized corrosion, primarily pitting, and provides a cleaner, longer lasting surface finish.

Stainless steel performed well in the quantitative analysis by transferring none of its mass to the environment and is shown in Figure 51 to also maintain a very clean surface after one year of exposure.

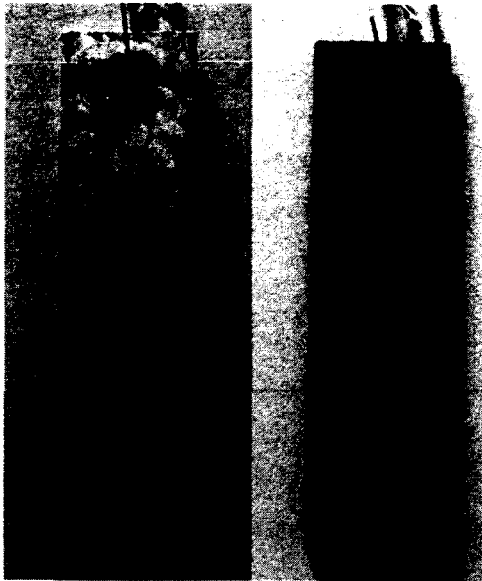


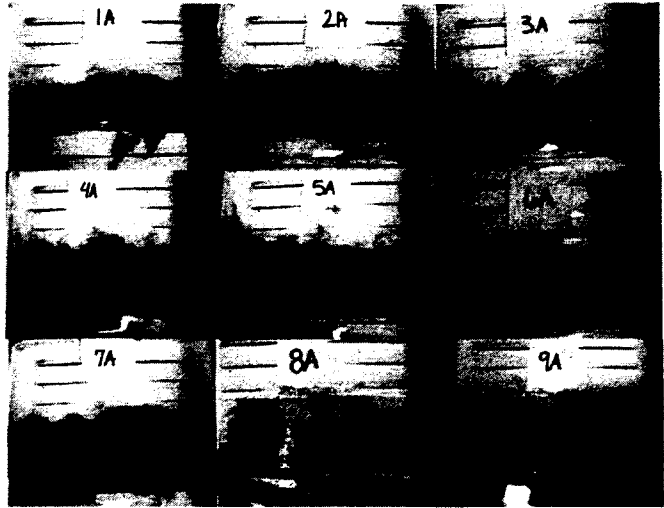
**Figure 50. Bare aluminum (left) and anodized aluminum (right) after one year of submerged exposure (from panel A).**



**Figure 51. Stainless steel coupons after one year of exposure (Panels A through D from left to right).**

### 5.5.3 Biofouling Results

Biomass seasonal accumulation is shown in the collection of images provided in Figure 52. The majority of the growth takes place during the summer months, and nearly no growth during the winter months. The seasonality is quantified by comparing measured mass of removed growth, shown in Figure 53. Panel A was cleaned of biomass every quarter so the measured mass is of only that which has grown over three months. To understand the compounding effect of biomass a cleaned panel is compared to an undisturbed panel the following quarter as shown in Figure 54. Since panel A is cleaned every quarter, it is compared to panel C in October and panel D in January. Figure 54 also indicates the natural reduction in biomass after the growing season by comparing panel C to panel D mass. Those panels are compared directly in Figure 55 showing that between 40 and 90 percent of the biomass falls or dies off naturally between October and January for uncoated samples.



1	(EN) Steel
2	Anodized Aluminum
3	Stainless Steel
4	Aluminum
5	Steel
6	Steel - ePaint
7	EN Steel - ePaint
8	Aluminum - ePaint
9	Cast Urethane



Figure 52. Panel A coupons after recovery, prior to cleaning, in July (top), October (middle) and January (bottom).

1	(EN) Steel
2	Anodized Aluminum
3	Stainless Steel
4	Aluminum
5	Steel
6	Steel - ePaint
7	EN Steel - ePaint
8	Aluminum - ePaint
9	Cast Urethane

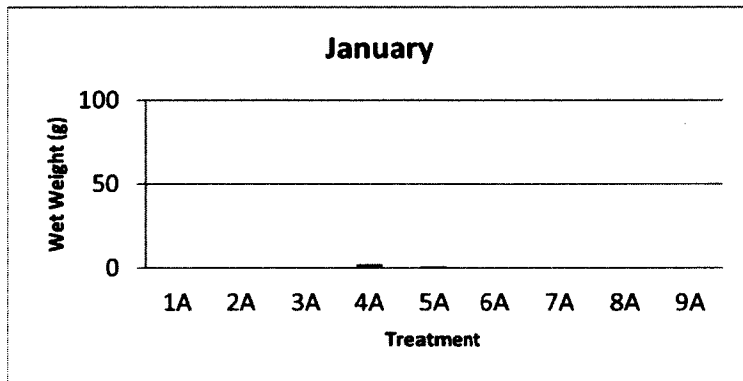
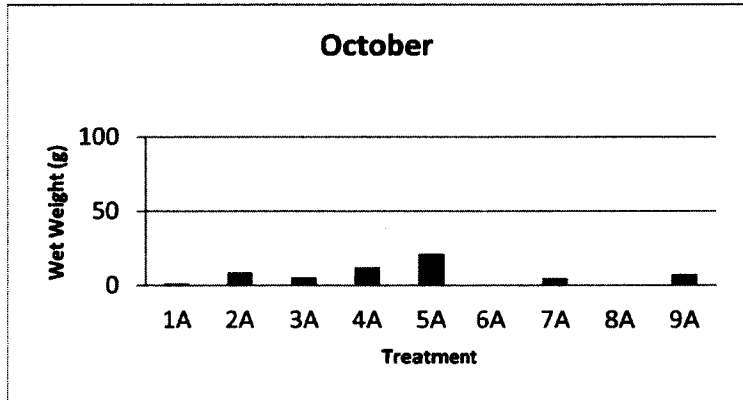
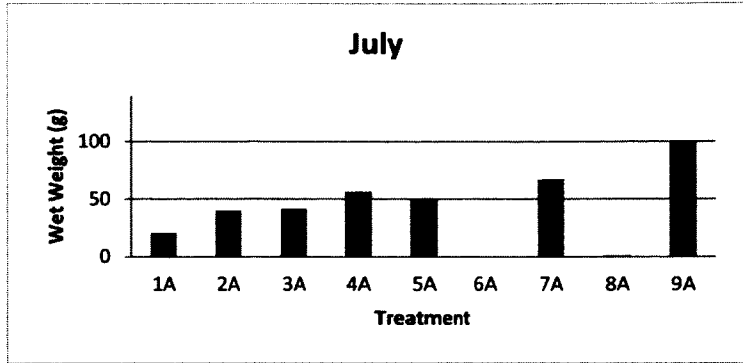


Figure 53. Panel A coupon biomass accumulation without sediment to show growth accumulation over each quarter.

1	(EN) Steel
2	Anodized Aluminum
3	Stainless Steel
4	Aluminum
5	Steel
6	Steel - ePaint
7	EN Steel - ePaint
8	Aluminum - ePaint
9	Cast Urethane

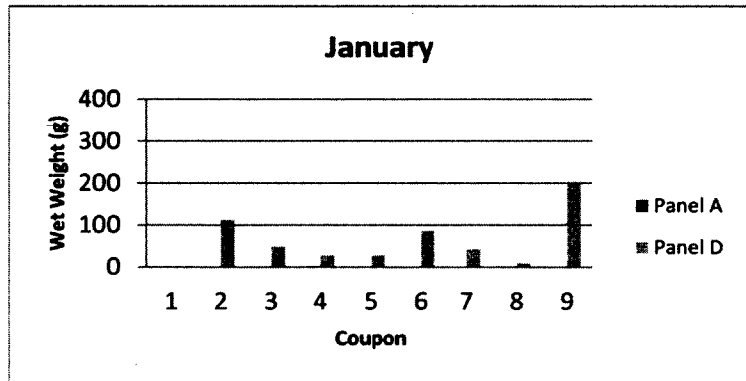
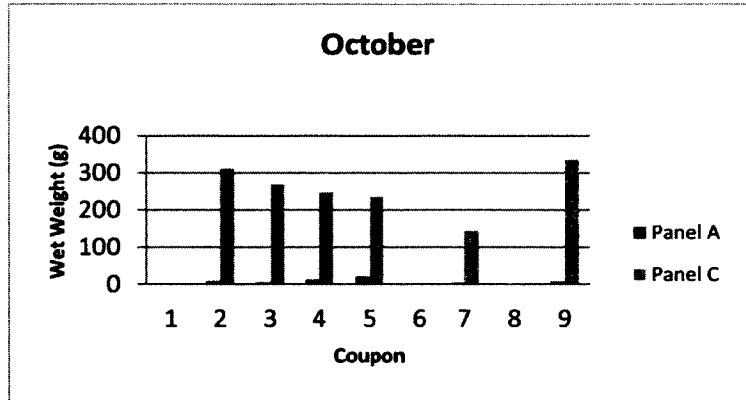
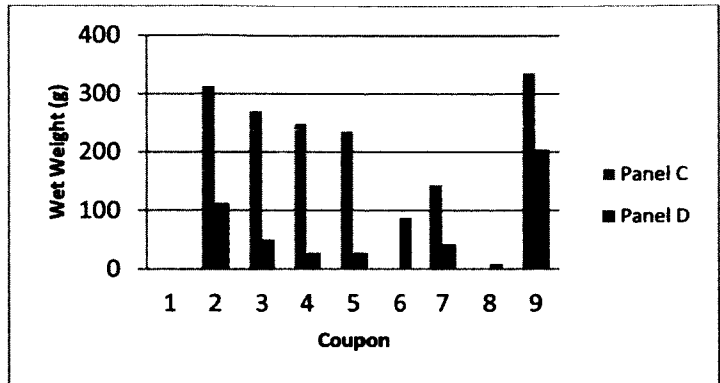


Figure 54. Compounding effects of biomass accumulation by comparison of panel A (cleaned quarterly) to undisturbed panels C in October and D in January.



1	(EN) Steel
2	Anodized Aluminum
3	Stainless Steel
4	Aluminum
5	Steel
6	Steel - ePaint
7	EN Steel - ePaint
8	Aluminum - ePaint
9	Cast Urethane



**Figure 55. Initial recovery of panel C (October) compared to initial recovery of panel D (January) showing natural reduction in biomass in colder months.**

Due to the limited number of coupons, the coupons coated in ePaint were split such that panels A and C received Ecominder and panels B and D received EP-2000. To determine relative performance of ePaint products the results are compared by panel. In Figure 56 coupons 6, 7, and 8 are materials coated in ePaint. It is shown that biomass accumulation on coupons with ePaint is significantly less in most situations. An anomaly lies with EN steel coated in Ecominder, coupon 7 on panels A and C. Yet Ecominder on steel and aluminum virtually inhibits all growth. Samples with EP-2000 accumulated an average of 8% of the mass that grew on uncoated samples after the first six months, and 14% after the following 3 months as seen on Panel B. After a year of submersion with no disturbance the average growth was 55% of that on uncoated samples. However, the accumulation on coupon 6D (steel with EP-2000) was influenced in large part by organisms that were attached to large mussels (byssal threads) which were attached directly to the panel.

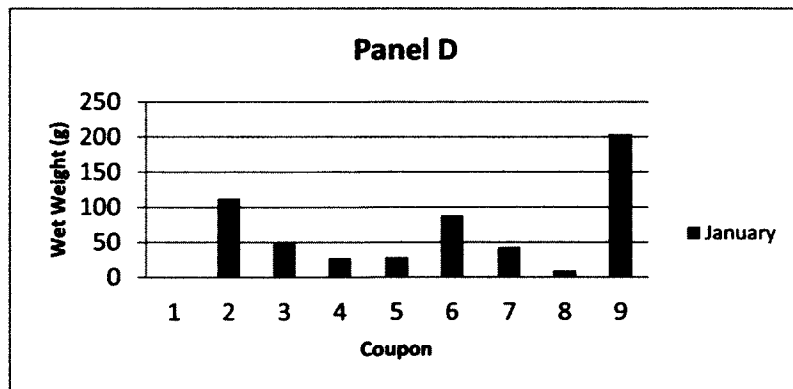
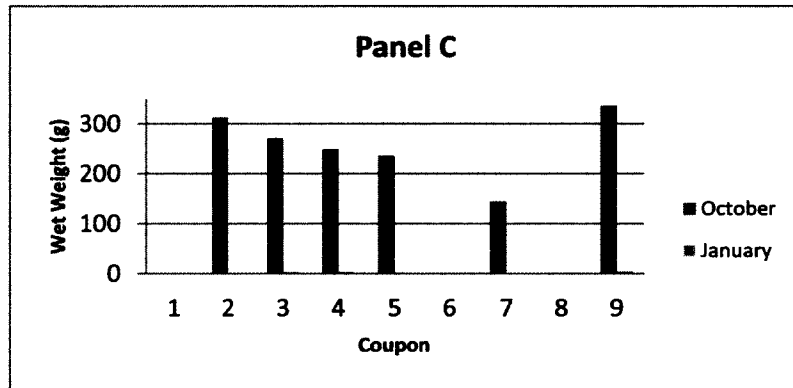
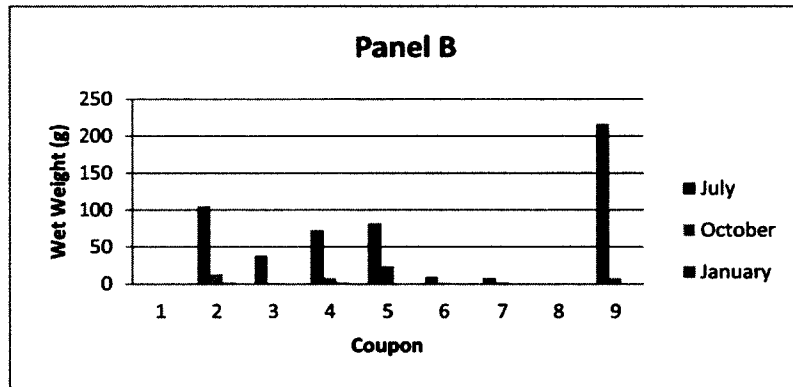
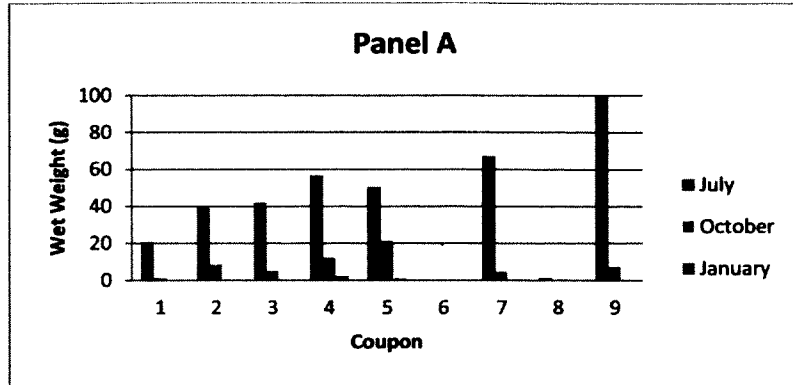


Figure 56. Biomass accumulation per panel for each recovery. (Scale changed per plot for clarity)

The cast urethane used in the MEHT shroud (coupon 9) showed no reaction resulting in mass loss, but accumulated more biological growth in all situations.

## **5.6 Conclusions for Materials Corrosion and Biofouling Study**

The materials corrosion study yields the following conclusions:

- Electroless nickel plated steel had twice the corrosion rate of untreated steel due to severe localized corrosion.
- Untreated steel loses approximately 10% of its mass due to corrosion after one year of exposure.
- Anodizing aluminum provides a longer lasting surface finish and inhibits localized corrosion.
- Samples susceptible to corrosion showed a significant increase in resistance when coated with either one of the two ePaint products tested.

The biofouling study yields the following conclusion:

- During the heavy growth summer season, biological growth covers nearly the entire surface area of coupons untreated with a growth inhibitor.
- Biomass is naturally reduced by 40% to 90% in the winter months.
- Both ePaint products effectively prevented adherence of biomass with a maximum effect of blocking 100% of growth during peak season while at the same time showing little to no resistance to growth on EN steel.

## **6 Project Summary and Conclusions**

A Mixer-Ejector Hydrokinetic Turbine (MEHT) designed by FloDesign Inc., working closely with FloDesign Wind Turbine Corp, was tested at two open water test sites and in a tow tank. Prior to testing, the University of New Hampshire Center for Ocean Renewable Energy (UNH-CORE) hydrokinetic turbine test platform V.1 was renovated and outfitted with state-of-the-art instrumentation. Tidal current predictions were generated for the UNH Tidal Energy Test Site and a mooring load numerical model (cf. Dewhurst, 2013) was generated for the Muskeget Channel test site.

The MEHT was tested during three flood tides at the UNH Tidal Energy Test Site in May, 2012. Results from the testing verified the tidal current predictions, established a baseline for turbine wake velocity deficit and turbulence intensity in open water, and enabled the calculation of the drag area of the test platform. Nominal MEHT power output and power coefficient results were reported.

The MEHT was tested during two ebb tides and one flood tide at the Muskeget Channel Test Site in July, 2012. Free stream velocity was characterized in terms of mean and turbulence and a rotor cut-in velocity was determined to be at 1 knot. Measured mooring loads verified the numerical model. MEHT wake velocity was measured and compared to previously measured profiles showing a more rapid decay at the more turbulent Muskeget Channel test site. Nominal power output and power coefficient results were reported for the MEHT.

The MEHT was tested in the UNH tow tank over two days in December, 2012. Detailed wake velocity profiles were measured and compared to open water testing. The MEHT drag coefficient was found experimentally for aligned and yawed conditions and an MEHT rudder was tested and found to contribute minimally to yaw torque.

A one-year corrosion and biofouling study was performed at the UNH Pier with materials used for MEHT fabrication. The study compared results obtained quarterly to results obtained from undisturbed samples over the course of the year. Corrosion rate was determined by measuring mass loss and accumulation of biomass was determined by measuring wet weight after removal from the coupon. The effect of two marine coatings on corrosion and biomass accumulation was investigated.

The MEHT was able to generate power from tidal currents over a wide range of conditions, with low-velocity start-up. The wake downstream of the turbine was found to recover more quickly with increasing levels of free stream turbulence, which has implications on array spacing. While analysis of some of the data from the two tidal energy test sites is ongoing, testing of the MEHT at this scale is complete. Future plans for the FloDesign MEHT include a scale up to a 4 to 7 ft rotor diameter turbine.

## **References**

- American Institute of Steel Construction, Inc. (1989). *Manual of Steel Construction* (9<sup>th</sup> ed.).
- ASTM G1-03 (2009). *Standard Practice for Preparing, Cleaning, and Evaluating Corrosion Test Specimens*. ASTM International
- Bachant, P. (2011). *Experimental Investigation of Helical Cross-Flow Axis Hydrokinetic Turbines, Including Effects of Waves and Turbulence*. Durham: University of New Hampshire.
- Bachant, P., & Wosnik, M., (2013). *Performance and Near-Wake Measurements for a Vertical Axis Turbine at Moderate Reynolds Number*. Proceedings of the ASME Fluids Engineering Division Summer Meeting, July, 2013 *In Press*
- Baia, S. & Carrier, C. (2011). *VFG Support Structure*. University of New Hampshire TECH 797 Final Project
- Bedard, R., & M. Previsic, B. Polagye, G. Hagerman, & A. Casavant. (2006). North American tidal in-stream energy conversion technology feasibility study. *Electric Power Research Institute, EPRI TP-008-NA*.
- Bedard, R., & Previsic, M., Hagerman, G. (2007). *North American Ocean Energy Status March 2007*. Electric Power Research Institute (EPRI) Tidal Power (TP), Volume 8, 2007.
- Bergey, K.H. (1979). *The Lanchester-Betz Limit*. *Journal of Energy*, 3, 382-384
- Betz (1920) Das Maximum der theoretisch möglichen Ausnutzung des Windes durch Windmotoren. *Zeitschrift für das gesamte Turbinenwesen*, 20. September 1920.
- Bilgili, A., & J.A. Proehl, D.R. Lynch, K.W. Smith and M.R. Swift (2005). *Estuary/Ocean Exchange and Tidal Mixing in a Gulf of Maine Estuary: a Lagrangian Modeling Study*, *Estuarine, Coastal and Shelf Science*, vol. 65/4, 607-624.
- Boon, J.D. (2004a). *Secrets of the Tide, Tide and Tidal Current Analysis and Prediction, Storm surges and Sea Level Trends*. Horwood
- Boon, J.D. (2004b). *Simply Currents*.  
<http://www.mathworks.com/matlabcentral/fileexchange/4450> [accessed March 2011]
- Byrne, J., (2013). *Design of a floating platform for testing hydrokinetic turbines*. M.S. Thesis. Durham: University of New Hampshire. *In press*.

- Cada, G., & Ahlgrimm, J., Bahleda, M., Bigford, T., Stavrakas, S., Hall, D., Moursund, R., Sale, M. (2007). *Potential Impacts of Hydrokinetic and Wave Energy Conversion Technologies on Aquatic Environments*, Fisheries, 32:4, 174-181
- Chambers, A., & Yetiv, S. (2011). *The Great Green Fleet*. Naval War College Review, Summer-2011.
- Darnell, L. (1996). *A Towing Carriage for the University of New Hampshire Towing and Wave Making Basin*. Master's Thesis.
- Darrieus, G. J. (1931). *Patent No. 1,835,018*. United States of America
- Davis, E. (2007). *Piscataqua River 2007 Current Survey*. PIR0710 – General Sullivan
- Dean, R., & Dalrymple, R. (1984). *Water Wave Mechanics for Engineers and Scientists*. Prentice Hall
- De Vries O. (1979). *Fluid dynamic aspects of wind energy conversion*. AGARDograph No. 243.
- Dewhurst, T. (2013). *Design of a Tidal Energy Test Platform in the Muskeget Channel*. Durham: University of New Hampshire. *In Press*
- Dewhurst, T., & Swift, M.R., Wosnik, M., Baldwin, K., DeCew, J., Rowell, M. (2013). *Dynamics of a Floating Platform Mounting a Hydrokinetic Turbine* Marine Technology Society, 2013 *In Press*
- Dexter, S. (1972). *Handbook of Oceanographic Engineering Materials*. Woods Hole Oceanographic Institution.
- Drach, A., & Tsukrov, I., Gross, T., Hofmann, U., Aufrecht, J., Grohbauer, A. (2012). *Corrosion Rates and Changes in Mechanical Properties of Copper Alloys Due to Seawater Exposure*. Proceedings of ASME 2012 International Mechanical Engineering Congress and Exposition.
- Durr, S., & Thomason, J. (2010). *Biofouling*. Chichester: John Wiley & Sons
- ePaint (2011). *Case Study: Heavy Metal Contaminants Detected in Storm Water Run-off and Boat Wash Water Effluent for ePaints vs. Traditional Copper-based Antifoulants*
- Erturk, S.N., & A. Bilgili, M.R. Swift, W.S. Brown, B. Celikkol, J.T.C. Ip and D.R. Lynch (2002). "Simulation of the Great Bay Estuarine System: Tides with Tidal Flats Wetting and Drying", *Journal of Geophysical Research: Oceans*, vol. 107, No. C5, 6-1 – 6-11.
- Gilbert, B. L., & Foreman, K. M. (1983). Experiments with a diffuser-augmented model wind turbine. *Journal of Energy Resources Technology*, 105, 46–53.

- Greene J., & Grizzle R., (2007). *Successional development of fouling communities on open ocean aquaculture fish cages in the western Gulf of Maine, USA*. *Aquaculture*, 262(2-4), pp. 289–301
- Haas, K., & Fritz, H., French, S., Smith, B., Neary, V., (2011). *Assessment of Energy Production Potential from Tidal Streams in the United States*. Georgia Tech Research Corporation
- Hanson, H.P., & S.H. Skemp, G.M. Alsenas, and C.E. Coley, (2010). *Power from the Florida Current: A new perspective on an old vision*. *Bulletin of the American Meteorological Society*, 91, 861-867.
- Hansen, M. (2008). *Aerodynamics of Wind Turbines*. Earthscan.
- Hansen, M., & Sørensen, N., Flay, R. (2000). Effect of Placing a Diffuser around a Wind Turbine. *Wind Energy*, 3, 207–213
- Hansen, R. (2007). *Water Wheels*.  
<http://www.waterhistory.org/histories/waterwheels/>[accessed 5 September 2012].
- Hardisty, J. (2009). *The Analysis of Tidal Stream Power*. Chichester: John Wiley & Sons
- Howes, B.L., et al. (2009). *Marine Renewable Energy Survey of Muskeget Channel, Massachusetts Technology Collaborative Report*, December 2009.
- Howes, B.L., & Samimy R., Schlezinger, D., Benson, J. (2011). *Environmental Effects of Sediment Transport Alteration and Impacts on Protected Species: Edgartown Tidal Project, Topic Area II: Marine Science and Hydrokinetic Site Specific Environmental Studies*, SMAST-CSP Report to US DOE, January 2011.
- Manwell, J., & McGowen, J., & Rogers, A. (2009). *Wind Energy Explained*. Hoboken: John Wiley & Sons.
- McCafferty, E. (2010). *Introduction to Corrosion Science*. New York: Springer
- McKay, D. (2009). *Sustainable Energy - Without the Hot Air*. UIT Cambridge.
- Muskeget Tidal Energy Project (2010).  
<http://www.mrec.umassd.edu/resourcecenter/muskegettidalproject/> [accessed September 10, 2012]
- Ocean Renewable Power Company (ORPC) (2012). *America's First Ocean Energy Delivered to the Grid*. September 13, 2012.
- Panton, R. (2005). *Incompressible Flow*. Hoboken: John Wiley & Sons.
- Polagye, B., & Epler, J., and Thomson, J. (2010). *Limits to the predictability of tidal current energy*, MTS/IEEE Oceans 2010, Seattle, WA September 20-23, 2010.



Polagye, B., & Copping, A., Kirkendall, K., Boehlert, G., Walker, S., Wainstein, M., Cleve, B. (2010). *Environmental Effects of Tidal Energy Development*. Northwest National Marine Renewable Energy Center (NNMREC) Workshop Briefing Paper.

Rourke, F., & Boyle, F., Reynolds, A. (2010). *Tidal Energy Update 2009*. Applied Energy, 87, 398-409

Savitzky, A., & Golay, M., (1964). *Smoothing and Differentiation of Data by Simplified Least Squares Procedures*. Analytical Chemistry, vol 36, No. 8.

Sorensen, J.N. (2011). *Aerodynamic Aspects of Wind Energy Conversion*. The Annual Review of Fluid Mechanics, 43, 427-448.

Survey Vessels - R/V First Light (2012).  
[http://www.crenvironmental.com/vessels\\_first\\_light.php](http://www.crenvironmental.com/vessels_first_light.php) [accessed July 3, 2012]

Swift, M.R. & W.B. Brown (1983). "Distribution of Bottom Stress and Tidal Energy Dissipation in a Well-Mixed Estuary", Estuarine, Coastal and Shelf Science, vol 17, 297-317.

Thomson, J., & Polagye, B., Durgesh, V., & Richmond, M. (2012). *Measurements of Turbulence at Two Tidal Energy Sites in Puget Sound, WA*. IEEE Journal of Oceanic Engineering, 37, 363-374.

United States Federal Energy Regulatory Commission (FERC) (2012). *Order Issuing Pilot Project License*. January 23, 2013

United States Department of Energy (2010a). DOE Technology Readiness Levels for Marine Energy, WWP-EERE.

United States Department of Energy. (2010b). *Annual Energy Review 2009*. Washington, DC.

United States Department of Energy. (2012). *Annual Energy Review 2011*. Washington, DC.

Vanek, F., & Albright, L. (2008). *Energy Systems Engineering*. New York: McGraw Hill.

Werle, M., & Presz, W. (2008). *Ducted Wind/Water Turbines and Propellers Revisited*. Journal of Propulsion and Power, 24, 1146-1150

Werle, M., & Presz, W. (2009). *Shroud and Ejector Augmenters for Subsonic Propulsion and Power Systems*. Journal of Propulsion and Power, 25, 228-236

Werle, M. (2011). *Passing Through the Wind Turbine Thrust Singularity*. Journal of Propulsion and Power, 27, 908-912

Woods Hole Oceanographic Institute (WHOI) (1952). *The History of the Prevention of Fouling*. Marine Fouling and Its Prevention, US Naval Institute.

## **Appendix A**

### **A.1 Detailed Renovations of UNH-CORE Tidal Energy Test Platform V.1.**

The UNH-CORE Tidal Energy Test Platform version 1 is a 35 ft long, 10 ft wide pontoon boat owned by the UNH Center for Ocean Renewable Energy (CORE) and is dedicated to hydrokinetic turbine testing. The motivation and the process for redesigning the turbine deployment system are described here. Engineering analysis, outsourced fabrication details, prices and detailed descriptions are included as a reference for future maintenance and modifications. Drawings are provided in another appendix.

The original design, first assembled in 2008 and shown in Figure 57, included a 5' x 5' moon pool in the deck slightly aft of centerline used as the turbine frame mounting location. The remainder of the deck was a flat plywood surface. Several turbine deployments were performed with this system of both cross stream and axial devices between 2009-2011 (summarized by Baia & Carrier 2011). The pre-renovation deployment process required the turbine and the tripod frame to be lowered into the water with flotation so that the moon-pool on the platform could be positioned over the frame so that it could then be hoisted into position. If turbine dimensions permitted, an adaptation to that process was to lower the turbine and tripod frame directly through the moon-pool from the pier avoiding the need to provide temporary flotation while positioning



**Figure 57. UNH-CORE Tidal Energy Test Platform v1 prior to modifications.**

the platform over the frame.

The described mechanism for deploying the turbine was executed successfully on a few occasions. However, relative motion between the pier and the platform, as well as the existence of several pinch points made this a dangerous operation. Furthermore, upon leaving the pier, it was not possible to transit without the turbine deployed, or extract the turbine in an emergency. Several new designs were considered with the attempt to maintain as much of the existing infrastructure as possible. The final design, shown in Figure 58, required significant enlarging of the opening in the deck to allow for a design that rotates the frame and turbine into and out of the water. This system enables turbine deployment and extraction to take place away from pier facilities and substantially reduces the risk to personnel.

#### Turbine deployment mechanism design

The new design utilized the deck frame and tripod built by a 2010-2011 TECH 797 senior project design team to test an un-ducted in-stream hydrokinetic turbine with a direct-drive generator (Baia & Carrier, 2011). The frame was modified to allow for on-site turbine deployment and turbine extraction under load

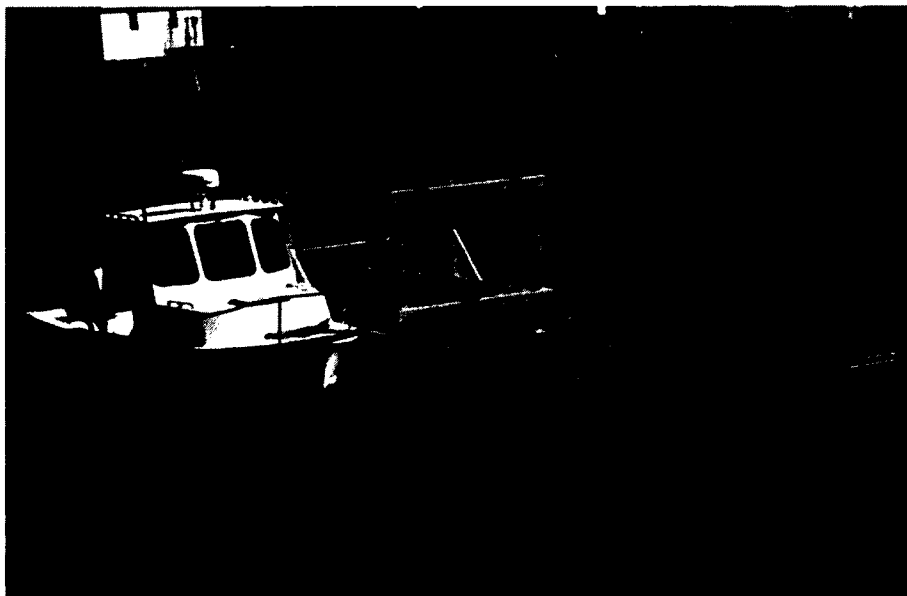


**Figure 58. UNH-CORE Tidal Energy Test Platform v1 and support vessel after modifications.**

by adding a pivot mechanism. A new stationary frame was added to the platform that distributes the weight and drag loads directly over each pontoon and incorporates a fixed gantry crane to support a hoist that is used to rotate the tripod frame. The CAD rendering of the turbine support system is shown in Figure 59.

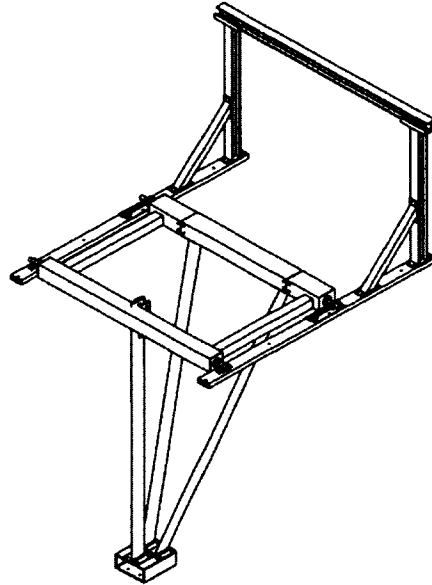


**Figure 59. Turbine deployment structure.**

Several modifications were necessary to accomplish this new deployment mechanism. The existing box beam frame had to be supported by a shaft (round bar) in the front to enable rotation and be designed to quickly lock in the deployed position. Also, a feature to rapidly extract the turbine in the event of an emergency or equipment casualty had to be implemented. Loading analysis was performed to validate choosing a 1.5 inch diameter steel rod spanning the width between load bearing members in front and rear. A  $\frac{1}{4}$  inch thick steel plate was welded onto the end faces of each box beam with a centered hole and bolt pattern to accept a flanged shaft collar and the support bar. This was done on both the fore and aft box beams. The forward shaft rotates in a flanged split bearing mounted to each load distributing rectangular box beam and the aft shaft

drops into a fabricated clasp on each side in the deployed position. To prevent lateral motion of the rotating bar, a shaft collar was added to the end of each shaft, outboard of the bearings.

To enable a rapid lock and release of the aft shaft, special clasps were designed and manufactured, shown in Figure 60. Engineering analysis was performed to determine the handle length such that under maximum turbine drag loading, a greased hitch pin could be removed with 20 pounds of force. The open clasp accepts the aft shaft as the system is rotated into the water. When fully deployed the handle is closed over the shaft and a hitch pin inserted to keep the handle down. To extract, the hitch pin is removed, the handle lifted and the turbine and frame can be rotated out of the water.

The forward bearings and the aft clasps are mounted to a load distributing steel rectangular box beam that is bolted to struts that are bolted to the pontoons. The box beam is centered over the pontoon to evenly distribute the loads. The box beam continues aft past the clasp and provides support and distributes loads from the steel frame that is the base of the gantry crane.

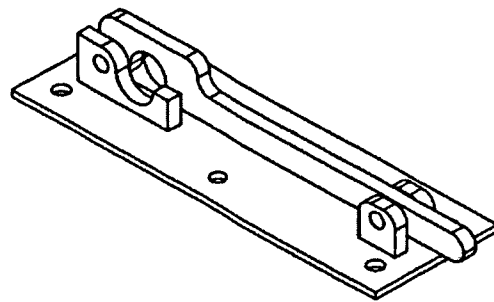


**Figure 60. Clasp to lock the turbine and frame in the deployed position.**

Hand calculations and SolidWorks finite element analysis were performed to determine the size and shape of beam for the gantry crane. W4x13 A-36 steel I-beams were chosen for their strength to weight ratio, compact nature and the ability to coat all surfaces with rust inhibiting paint. Each column has a plate welded to the bottom to allow easy bolting to the box beam, and a c-channel welded to the top to accept the horizontal member of the gantry. The C-channel provides easy alignment, gusseted support and easy bolt up to the cross member. Each column is also supported by a 3 foot box beam 45 degree member to brace it in the vertical position. The brace was designed as a split I-

beam, but during fabrication, cost was reduced by utilizing a more available square tube. Since a plate is welded to each end the interior is air and water tight so internal corrosion concerns are tolerable. The plates on each end of the brace enable quick bolt together assembly to the vertical column I-beam and the horizontal box beam frame.

Grade 8 nuts, bolts, ( $\frac{1}{2}$ -13), and washers were chosen to secure the crane and frame assemblies to save cost over 316 stainless steel fasteners. While the strength of the bolts has proven sufficient over the past year of testing, the unsightly surface corrosion of the grade 8 nuts, which, unlike the bolts do not have a zinc yellow-chromate coating, may justify replacement with stainless fasteners. All steel surfaces were primed with one rolled coat of Rustoleum primer followed by one rolled coat of yellow Rustoleum enamel paint.

A 2000 pound capacity electric hoist was selected to drive the rotation of tripod frame. The hoist is not designed for prolonged outdoor exposure so a removable mount was designed to provide quick secure installation and easy removal. Four 5 inch threaded rods are bolted into the manufacturers mounting plate and secured with a lockdown bolt. Two pieces of angle iron were machined with a hole in one side and a slot in the other. Two threaded rods are bolted loosely through the hole in the angle iron and as the hoist is positioned in place the angle iron is swung across the top of the horizontal I-beam on the gantry such that the notches accept the other two threaded rods. Nuts and washers can then be inserted from the top of the threaded rod and tightened so that the two sections of angle iron support the hoist from the top face of the crane I-beam. An image of the installed hoist is shown in Figure 61.

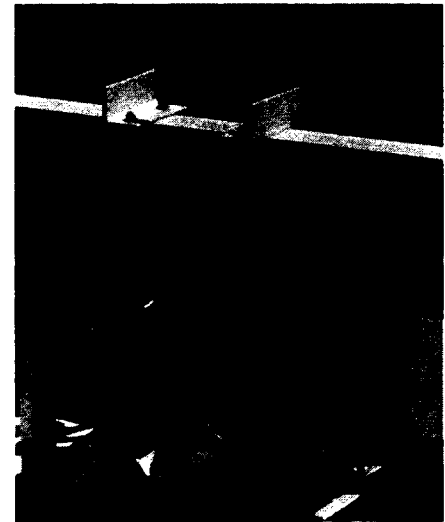


Figure 61. Hoist mounted on gantry crane.

### A.3.2 Aft platform design

The aft portion of the platform was modified to enable detailed wake measurements of the turbine while deployed using an acoustic Doppler velocimeter (ADV) deployed on a sting attached to a traversing system. To accomplish this, the instrument would need to be inserted into the water very close to the exit plane of the turbine, submerged to the turbine centerline, traversed in the cross-stream direction and then be incrementally positioned further downstream. To allow for continuous movement downstream to the desired downstream positions, all the stringers connecting the pontoons aft of the moon pool needed to be removed. To ensure structural stability of the vessel, an elevated platform was designed that rigidly connects the pontoons, but leaves the deck level open to allow full stream-wise positioning of the instrument via a traversing system. Measuring and estimating all loadings and motion of a vessel at sea is challenging, thus designing a pontoon coupling that is structurally sufficient is also challenging. The method chosen to ensure no compromise in

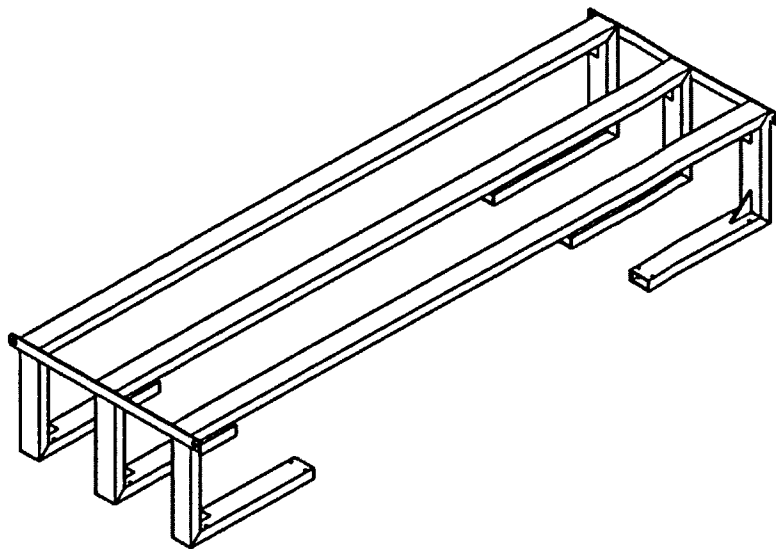


Figure 62. Aft platform model.

seaworthiness was to calculate deflections and stresses of the existing design and make the new design perform within those calculated parameters for equivalent loading.

The existing cross members were modeled in SolidWorks and analyzed with the built in simulation package. Finite Element Analysis (FEA) was used to measure stresses and deflections given expected loadings. The members were analyzed in shear, as in towing on one side, and bending, as in taking a wave on the beam. Those same loads were applied to the new design and the stresses and deflections were compared.

The chosen material for the platform was 6061-T6 aluminum box beam tubing due to the cost, accessibility, corrosion resistance, and machinability. Three sections of 2x4 rectangular box tubing with gusseted corners, shown in Figure 62, were designed and analyzed with hand calculations and SolidWorks FEA. Final design criteria were that the frame had to allow for an open deck with adequate height for the traversing mechanism and that deflections and stresses not exceed the previous design for equal loading configurations. Once those criteria were met the design was sent out for fabrication.

The aft frame was designed to bolt directly to the channels welded along the length of each pontoon. The box thickness is the same as the height of the existing stringers so the future installation of decking required no design work. The three sections of framing are connected on the top outboard edge with a strip of aluminum that hold the frames together but could also serve as a support for the instrument traverse rail that extends off the back of the platform, discussed below. The fasteners to secure the frame to the platform are 5/16-18 stainless steel with nylon locknuts.

The stringers that were removed to expand the moon pool and necessitate the aft platform were relocated forward, with the exception of two which were cut into sections to provide a base for securing the plywood deck. The repositioned stringers were centered between the existing stringers, working in from the centerline and the bow to locate them where the highest loads are expected as shown in Figure 63.



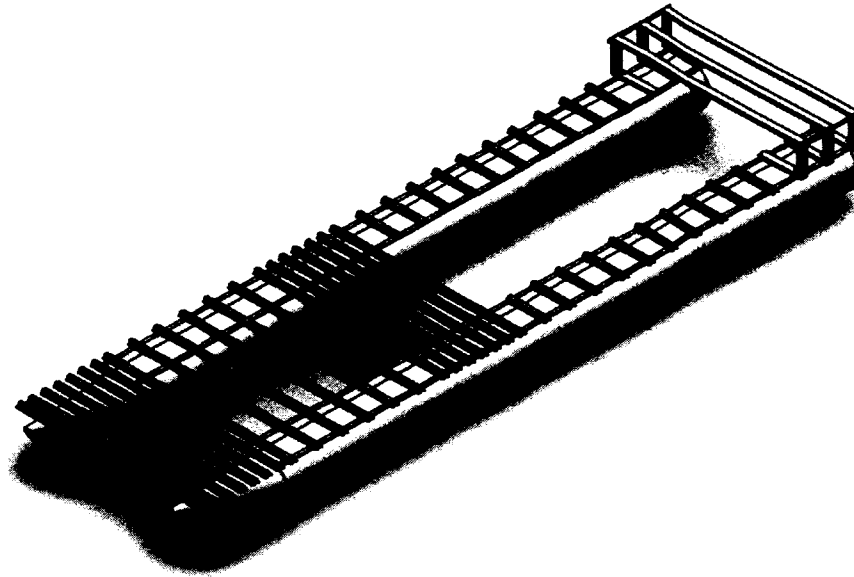


Figure 63. Pontoon stringer layout post overhaul.

### A.3.3 Platform decking design

Two different types of decking were chosen to replace the (now water logged) plywood that had been installed since on the platform from 2008-2011. A grated decking was chosen for the forward half of the platform since open water deployments at Muskeget Channel anticipated in the future. The likelihood of experiencing potentially damaging wave action, which could cause the bow to dive or a wave to strike the underside of the deck, is far greater at open water sites. In the event of the bow of the platform being driven into a wave, a solid deck would have the tendency to cause the vessel to plow under the water. By installing a grated decking the likelihood of plowing is greatly reduced. If a wave were to strike the platform the grated decking would dissipate the energy reducing the shock loading to the vessel. The aft half of the boat was chosen to be covered with marine plywood. The plywood is thinner and denser and more convenient to mate with the turbine support frame and gantry crane support beam. More labor is involved in preparing plywood for installation, but it is also less costly than the grating.

After researching several alternatives to grated decking, a fiberglass reinforced polymer product called ThruFlow Decking was chosen. This is a lightweight yet rigid product that is sold in panels that interlock and are easy to secure to the stringers. The top surface is non-skid yet not as sharp as some metal grated decking so that it provides sure footing but doesn't cut knees and hands when working at deck level. It is 1.2 inches thick resulting in a slight lip where it meets the 3/4" plywood, which turned out to be a non-issue. The ThruFlow decking does not provide the same structural support as the 3/4 marine plywood but this was offset by the increased number of stringers on the bow.

The plywood panel dimensions required to cover the aft were determined in SolidWorks and then inserted into Cutlist Plus software to optimize the cut layout and minimize waste. The plywood sections cover the pontoons from centerline aft, the aft platform and a removable work platform to assist in mounting and working on the turbine.

The plywood sheets were cut to dimension using a circular saw and straight edge. Each piece was sealed using Interlux 1026 Interprime Wood Sealer with special attention paid to the edges. Each piece was then primed with Interlux 4279 Pre-Kote white primer. The underside and edges of each panel were coated with Interlux white Brightside polyurethane paint. The topside and exposed edges were covered with Interlux Brightside grey polyurethane paint with Interlux Intergrip Non-skid Additive mixed in. Every coat was rolled on and brushed into tight corners and the non-skid coat is the only one that received two coats.

The section of plywood designed as the removable work platform over the moon pool was reinforced with two pressure treated 2x4's on edge on the underside of the plywood. They were installed with 3M 5200 Marine Adhesive Sealant along the interface and wood screws from the top surface of the plywood. The 2x4's were installed after all but the last coat of non-skid paint to ensure the plywood was treated but also to cover the screw heads with the final coat of paint. The 2x4 supports had to be tapered at each end so that the work platform would sit level with the rest of the deck and they were spaced off the

centerline so that the work platform could be stowed by a friction fit on the aft platform while underway. Flush mount handles were inserted into each end of the platform by routing out the necessary material and installed with provided mounting screws. Dolphinite bedding compound was applied to the inset prior to mounting the handles to prevent water from collecting in any open space under the handle.

#### A.3.4 Design implementation

Several logistical issues needed to be addressed prior to starting work on the platform. The first of which was determining where to conduct the overhaul. The available options were: while in the water, on the beach at the UNH pier, or on the UNH pier. The option of performing the overhaul while in the water was eliminated since stringers needed to be moved and the alignment of the pontoons could be jeopardized. This option of doing it on the beach was not chosen due to slope of the beach. The chosen option was to hire a boom truck to lift the platform onto the pier.

On the scheduled day, the boom truck drove down the pier just past the bend. The platform was brought alongside the pier and two slings were positioned under the platform leading up to the hook on the crane. Although spreader bars would have made the haul a little more comfortable, they were deemed unnecessary by the crane operator and the entire process took less than an hour. The platform was placed on pallets and blocks to allow pressure washing of the pontoons while also distributing the weight.

Once out of the water, all existing hardware and plywood were removed. The deck hardware was saved for reuse and the old plywood decking was cut into manageable sizes and discarded in a dumpster. The stringers aft of the moon pool were removed and repositioned forward. Two stringers were cut into sections and installed in the same location as the removed stringers to provide a base for the decking along the pontoons. The hole pattern for the aft platform was drilled into the rails on the pontoons and the aft platform was mounted. The plywood decking was installed by clamping the piece in place, pre-drilling holes

in the wood and through the aluminum stringers and then secured with stainless steel square drive fasteners.

With the plywood decking installed and extra stringers installed forward, the grated decking was installed. The panels measure 1'x4' and were installed 10 across in 4 rows from center to the bow. Each row was laid in place, interlocking across, centered, clamped and then fastened using stainless steel pan head self-drilling screws and an 18v DeWalt cordless hammer drill. Once one row was installed the next was laid in place and the process repeated.

The steel frame and gantry crane were transported to the pier and installed next. The rectangular box beam was positioned and secured with grade 8, ½" -13 bolts and nuts. Bolts at each end and in the middle were secured directly to the stringers that are bolted to the pontoons. With the box beam in place the rest of the equipment was mounted to it including the split bearings, the clasps and the framing for the gantry crane. Where appropriate, those bolts would also go through aluminum stringers, but otherwise they went through the box beam and plywood decking and were bolted against the plywood. Fender washers were chosen to distribute the load from the fasteners onto the plywood.

Finally, hardware was installed including deck cleats and a rubber fender on the starboard side. A total of 4 deck cleats per side were installed. The two forward deck cleats were installed with two bolts, the aft one through an aluminum stringer and the forward one through the grated decking with a fender washer on the underside. The two aft deck cleats were bolted to the plywood deck with fender washers on the underside. A 14' section of rubber fender was installed on the starboard side of the platform with wood screws and fender washers to provide protection to a support vessel, the Galen J, when towing from the hip.

The last step prior to launch was to pressure wash the pontoons. Much of the growth had died and fallen off during the overhaul process but the remainder was pressure washed using a machine owned by the pier facilities in New Castle.

The platform was launched using the opposite procedure of the haul. Shortly thereafter the modified tripod frame, with end plates and bars installed, was transported to the pier and lowered into place using the crane on the pier. At that time the system was operationally tested satisfactory and left on the mooring ball in the harbor in New Castle.



**Figure 64. Platform after overhaul prior to launch.**

## **A.2 Detailed Instrumentation on the UNH-CORE Tidal Energy Test Platform**

### **Generators**

Two generators were used on board of the test platform. One Honda EU2000 2kW owned by the Center for Coastal and Ocean Mapping (CCOM) on loan to the project and one EU1000 1kW provided by FloDesign. Both gasoline generators generate AC, convert it to DC and then back to AC using a clean sine wave inverter. This is an important feature given all the sensitive instrumentation being powered. The EU1000 was dedicated to instrumentation and computers and the EU2000 was dedicated to the turbine deployment hoist.

### **Computer**

A Panasonic CF-53 Toughbook was used to configure and operate all UNH instrumentation, the NREL ADV and the ADCPs onboard. It uses the Windows 7 64-bit operating system and has a 2.5GHz quad core Pentium i5 processor. It has 6 GB of RAM and 320 GB of storage on a 7200 RPM hard disc. The ports used during testing include the single serial port and 4 USB ports. The computer was powered from the 1kW generator.

### **Acoustic Doppler Velocimeters (ADV)**

Two ADVs were implemented on the test platform. One Nortek Vectrino, owned by UNH, and one Nortek Vector, provided by the National Renewable Energy Laboratory (NREL). The principle of operation for both is the same. The instrument emits an acoustic pulse from the transmitter, the pulse travels through a common focal point for several receivers which each measure the echo of the transmitted pulse. The Doppler shift is measured by each receiver, corrected for the density of the fluid, and processed into a velocity vector which is recorded either on the instrument, on the controlling computer, or both. The maximum sample rates were 32 Hz for the Vector, and 200 Hz for the Vectrino.

The Vector was located on the starboard bow with the probe 7 feet below the deck so that it was submerged approximately 5 feet. It was powered from the

1kW generator and was configured using the Toughbook laptop. Data was recorded both to the device and to the computer. It was configured to operate at 32Hz with a nominal velocity range of  $\pm 4.00\text{m/s}$  recording in the XYZ coordinate system. For testing at the UNH site the salinity was measured by refractometer and input at a value of 22 parts per thousand (ppt) and measured to be 33 ppt for the Muskeget test site. Between the GSB and Muskeget channel testing a wiring harness was installed that was intended to provide an analog signal of velocity for FloDesign to input into their LabView virtual instrument (VI). The analog signal was intended to provide an input to the resistor bank to keep the turbine performing at the optimal point on its power curve based on inlet flow velocity. Unfortunately, the analog signal was not obtained.

The Vectrino was located in the wake of the turbine and connected to a mechanism that allowed controlled motion in the stream wise and cross stream directions and fixed in depth at the centerline of the turbine, approximately 9 feet below the waterline. The instrument was powered by the 1kW generator and configured and operated by the Toughbook laptop. The Vectrino does not have the option to record to the instrument so all data was recorded to the computer. The instrument was configured to operate at 200Hz. For tests at GSB the nominal velocity range was selected to 2.50m/s, however, in post processing the scatter made processing more difficult so a value of 4.00m/s was chosen for the Muskeget Channel test with good results. Salinity values were set to 22ppt at GSB and 33ppt at Muskeget Channel and it always recorded in the XYZ coordinate system.

#### Acoustic Doppler Current Profilers (ADCP)

The Center for Ocean Renewable Energy owns an RDI 1200kHz Sentinel Workhorse ADCP that was on loan to another project during the testing at the UNH Test Site so RDI lent a 983kHz Sentinel V. Both operate on a principle similar to the ADV utilizing pulsed acoustic waves that scatter off particles in the water back to a receiver which measures the Doppler shift of the sound wave and processes a velocity vector. An ADCP temporally “gates” the returned signal

to determine from which region of the water column in front of the instrument the scattered sound came from. In this way, "measurement bins" (volumes) are established. The ADCP can thus measure velocity at many locations (volumes) over a much larger distance than the ADV, up to 200m in the case of the Sentinel V, but with less resolution and higher uncertainty than the ADV. The ADCP was mounted just below the waterline off the bow of the platform centered along the width of the platform. Therefore, the data collected is in the water column directly upstream from the turbine.

The Sentinel V operates independently of a computer after initial setup and initiation of recording. The instrument was configured to collect 60 bins of 0.1m with a 0.4m blanking distance. All data is recorded on the instrument. When the test is over the instrument is removed and accessed wirelessly to download to a computer for viewing and processing.

The Sentinel Workhorse was used for the testing at Muskeget Channel and configured to 64 bins of 0.2m. The Sentinel requires computer connection to start recording but records all data to an internal PCMCIA card and is powered from an internal battery. Upon completion of testing the data can be transferred by connecting the computer to the Instrument via USB, or the PCMCIA card can be removed from the instrument and inserted into a computer for data retrieval.

#### Electromagnetic Current Meter

A UNH owned Marsh-McBirney Flo-Mate 2000 electromagnetic flow meter was installed off the port bow of the test platform to serve as a backup velocity indicator. This is a standalone battery powered digital meter that can provide velocity measurements in ft/s or m/s with a programmable averaging interval. The probe was installed about a foot below the waterline to a rod with a fin that was allowed to rotate freely so that it would always be pointing in the direction of oncoming flow. A 20 foot cord connects the probe to the instrument housing where the signal is processed and displayed. The instrument served as a verification for real time analysis of ADV output and was used by FloDesign to



manually input free stream velocity to set resistor bank loading to optimize turbine performance.

### Wave Staff

An Ocean Sensor Systems, Inc. (OSSSI) water level sensor, or wave staff OSSSI-010-002E, was mounted off the bow to the starboard of centerline. The wave staff was outfitted with a 1.5m staff and configured to record at 10Hz. The Toughbook was used to configure and log data from the wave staff and power was provided from the 1kW generator.

The data obtained with the wave staff were used in combination with the Teledyne DMS IMU described below to assess platform motion. For details see Dewhurst 2013.

### National Renewable Energy Laboratory (NREL) Contributions

The testing timeline fortunately aligned with instrumentation availability at NREL. They developed a hydrokinetic turbine instrumentation test package and offered to install it on the UNH test platform for the GSB and Muskeget Channel tests. The aforementioned Nortek Vector ADV is part of the package as well as: a Teledyne DMS-05 Inertial Measurement Unit (IMU), 3 Meggitt Model 745 accelerometers, strain gauges, 2 twenty thousand pound load cells and swivels, a Programmable Sonar Altimeter, and a Hemisphere V101 GPS Heading Unit. All instrumentation, with the exception of the ADV, is wired into a weatherproof box that houses two Vicor VIPAC power supplies and a National Instruments Compact RIO (cRIO) that enables independent data collection and storage. The cRIO receives an input from an additional National Instruments GPS unit to assign a common timestamp to all data based on GPS time.

Once assembled, operation of the instrumentation package required providing 10-36 volts DC power and waiting for the green light indicating the GPS acquired a signal. The cRIO was programmed to record data files every 10 minutes to minimize data loss in the event of power interruptions. Data was

written to a USB drive so upon completion of testing the drive was inserted into the Toughbook for download.

The waterproof box into which the cables from all the instrumentation led was mounted to a wooden frame strapped to the deck of the platform, shown in Figure 65. The receiver for the small GPS that provides the timestamp to all the data is mounted on the top of the waterproof box so care had to be taken not to block its signal. The Hemisphere GPS was mounted to the top of the wooden frame as well. All wires to instrumentation left the box from bottom mounted water resistant fittings. The IMU was mounted to the tripod frame close to the turbine to record turbine motion as accurately as possible. The Meggitt accelerometers were also mounted near the turbine. The accelerometers were intended as a backup for the higher-quality IMU. The strain gauges were bed into the forward foil of the tripod with the intention of enabling turbine loading measurements after calibration. Since the tripod was designed to withstand turbine thrust forces up to 2,400 lbf with a considerable factor of safety (Baia and Carrier, 2011), the deformation of the tripod was insufficient to record strain with the strain gages. Shackles were used to connect the load cells to the forward eye on each pontoon and the swivel was put outboard of the load cell with a shackle to connect to the mooring line.

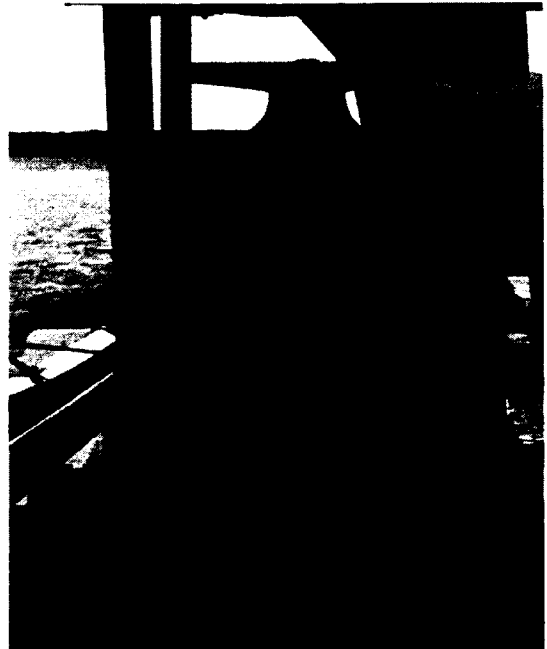


**Figure 65 NREL instrumentation enclosure and Hemisphere GPS.**

### Power Takeoff

All turbine power takeoff and performance evaluation was performed by FloDesign with equipment they supplied. The permanent magnet rim generator design generates a 3 phase AC output. Each phase voltage and current was

independently monitored using a WT 3000 Yokogawa power analyzer after which it was converted to DC in a 3 phase bridge rectifier. The power was dissipated in a 5kW DC Kepco electronic load bank which also provided a signal for monitoring via the Yokogawa power analyzer. An Ethernet output from both the power analyzer and load bank was directed to a router to allow wireless communication with both systems from an external computer. The load bank, power analyzer, router, and associated fuses, capacitors and wiring were installed in a weatherproof enclosure on castors and strapped down to the deck of the platform. LabView software was used to monitor, control, and record all settings on a laptop external to the weatherproof enclosure.

### Video

Two systems were used to capture video during the deployments, SeaView and GoPro. The SeaView cameras stream live video through a digital video recorder which enabled virtually unlimited continuous recording as well as real time monitoring. The GoPro cameras provide much higher resolution video but are not viewable in real time and are limited by battery life.

Three SeaView cameras were recording on each deployment. One was mounted on a sting out in front of the turbine which provided continuous viewing and recording of the turbine inlet. Another camera was mounted on the tripod frame with a downward view onto the top of the turbine and the last was mounted to a telescoping pole that allowed recording of topside activities and the ability to position it in the water around the platform. Fixed camera positions are shown in Figure 66. Each camera has nearly 100' of cable to an RCA output that was plugged into a 4 channel DVR with a 1TB hard drive via an RCA to BNC adapter. The DVR has a VGA out to provide real time viewing of each camera independently or up to four simultaneously. Each camera requires 12V DC power supply which was acquired by converting the 110V AC from the 1kW generator.

Two GoPro Hero 2's were used for each deployment as well. One was positioned on the same sting as the aforementioned SeaView camera to provide an inlet view of the turbine. For testing at GSB the second was located on the

ADV traversing sting to provide a view of the exit of the turbine. This video was poor due to lighting so the camera was used with a head strap for the testing at Muskeget Channel to provide a high definition video of topside activities. Each camera had a 16GB memory card which provided a little less than 4 hours of recording at a resolution setting of r3 which is 1280 x 720 pixels.

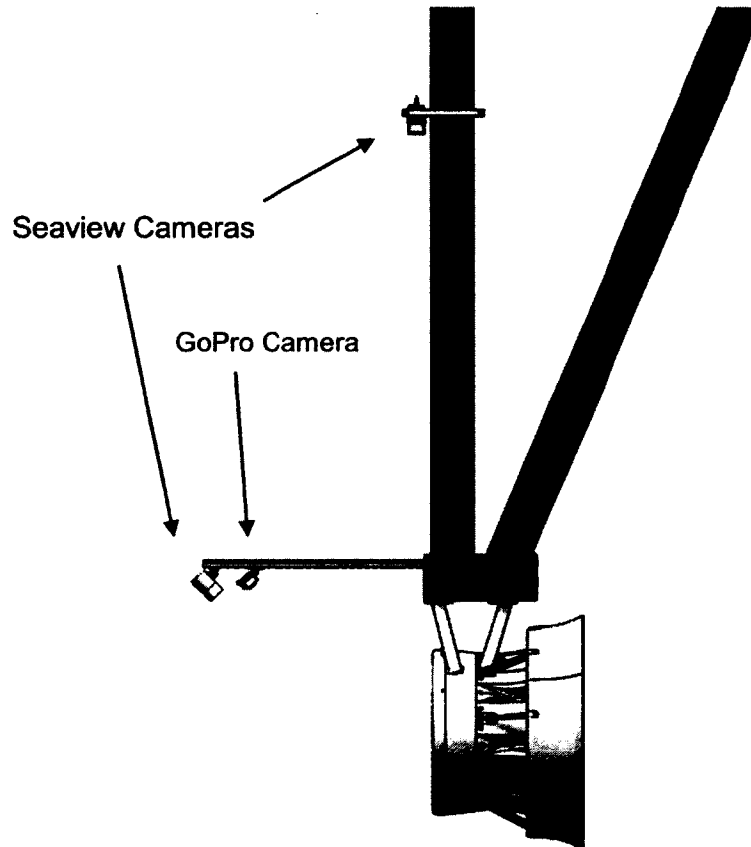


**Figure 66 Camera mounting locations for MEHT monitoring during testing.**

### **A.3 Detailed Instrumentation Mounting**

#### **ADV traverse: The submerged sting**

The wake traversing ADV and probe were mounted on a sting that was inserted into the water to a depth that aligned the probe sample volume at the centerline of the turbine. The Vectrino ADV has a remote probe with 3 feet of cable leading to the instrument housing and 60 feet of cable from the housing to the computer. The first submerged sting design, shown in Figure 67, utilized a 9 foot section of NACA 0020 aluminum extrusion (1) bolted to a 4 foot section of 1530 t-slotted aluminum extrusion (2). The probe was mounted to the bottom of the foil with a fabricated ultra-high molecular weight polyethylene (UHMW) mount and the body was attached to the front of the foil with straps. All cable was zip tied to the leading edge of the foil. The foil was mounted to the 1530 by two fabricated mounting plates (not shown) with 5/16 inch through bolts and spacers. The top section of 1530 extrusion was inserted into two linear bearings (3) that allowed some of the mechanism to be slid out of the water before removal from the traversing mechanism. Once deployed, a brake would secure the sting at the

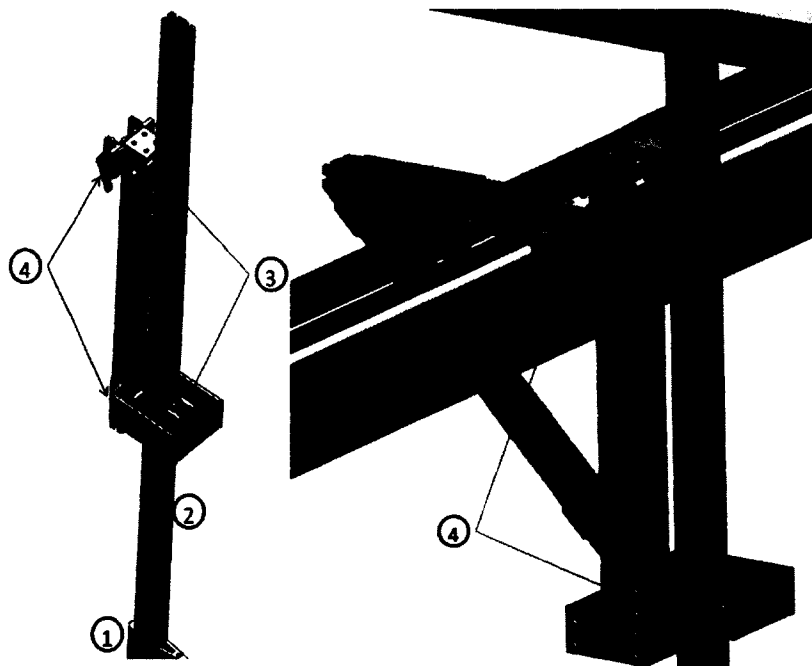


**Figure 67. Version 1 of the traversing ADV sting design.**

appropriate depth. The sting was mounted to the traverse with the use of two more linear bearings (4), one located on the sting frame and one on the traverse. A major fault with this design was that any off axis flows would create lift on the fixed airfoil causing a bending moment that could not be counteracted by the traverse mechanism. After learning the weaknesses during tidal cycle testing at the UNH Tidal Energy Test site in May of 2012 a new design was brought to Muskeget Channel in July of 2012.

The new design for the sting to mount the ADV aimed to maintain a streamlined shape to minimize drag, reduce mass, minimize lift effects caused by off axis flows and maintain or improve ease of installation. This was accomplished to some degree by using a 12 foot piece of aluminum pipe with aluminum sheet metal formed around the pipe in the shape of a foil and mounted to the pipe in such a way that would allow the foil to rotate 180 degrees to align itself with the flow. This design is shown in Figure 68. The schedule 40 aluminum pipe was cut to length from a 20 foot piece, and the sections of sheet aluminum were cut to size by the supplier. The only aluminum sheet available was 6061-T6 which is not a formable alloy, but was made to work by bending the sheet around the pipe and zip tying the trailing edges together every 12 inches. Before bending, a 5/16 inch wide slot as long as half the circumference of the pipe was cut near the top of the sheet. A 1/4-20 thread was tapped into the pipe in the appropriate location and the folded sheet metal foil slid over the pipe so that a stainless steel shoulder bolt with a 1/4-20 thread and 5/16 shoulder could be inserted. The shoulder bolt held the

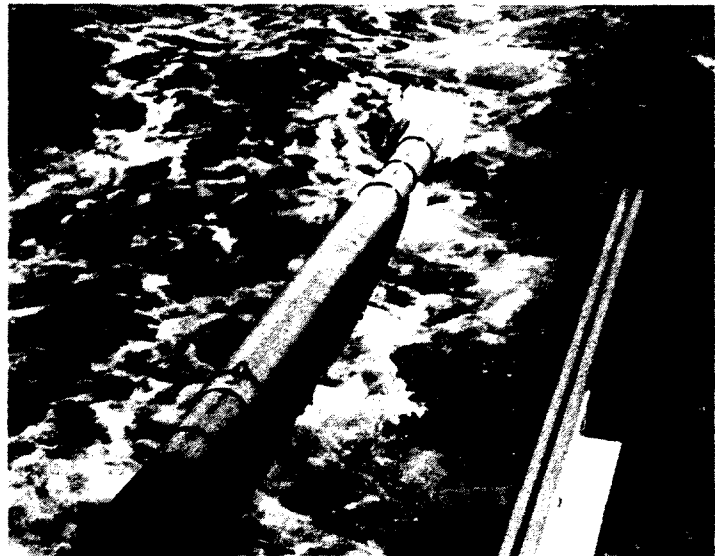


**Figure 68. Rotating streamlined foil prepared for deployment.**

vertical load of the sheet but since the sheet rode on the shoulder it was allowed to rotate. A zip tie was installed on the bottom of the foil to prevent the bottom leading edge of the foil from separating from the pipe. Silicone spray was also applied to the inside of the leading edge of the foil to try to reduce friction. The probe was secured with another UHMW mount, shown in Figure 68, and the instrument body was secured with straps. To streamline the ADV body, a neoprene sheet was wrapped around it and zipped tied in the shape of a foil. All instrument cables were zip tied to the pipe and run inside of the rotating foils. As in the original design, two linear bearings were mounted to the top of the pipe so that the sting could be inserted in the water, the bearings slid over two blocks, and a brake could be applied to lock it in place. The revised submerged sting mounting and locking configuration is shown in Figure 69. The new design worked better than the first, but did not resolve the limitation that the sting had to be installed during slack water. With even a minimal flow, the drag acting on the sting and platform motion made it very difficult to align the bearings.

A second design also included a more robust load bearing frame to accept a rapid connection of the submerged sting and distribute the mass and moment loads off of the Bislade traverse, discussed in more detail below. The original design utilized only one additional cross stream support and nylon linear bearings which, although effective, put an excessive load on the stepper motor. An additional member was positioned to distribute the drag loads more evenly on all the bearings. The nylon bearings offered by 8020 easily bind when any off axis load is applied, and even in an aligned loading situation the coefficient of friction was higher than expected. The improved design, shown in Figure 70 utilized two cross stream support

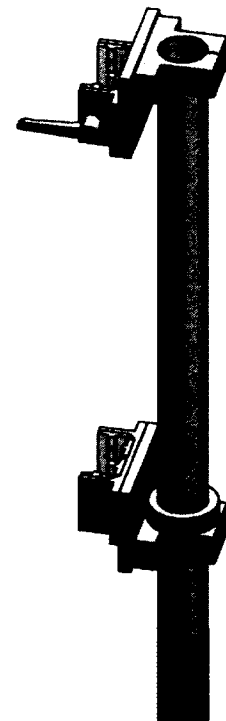


**Figure 69. The version 2 ADV sting mounting design.**

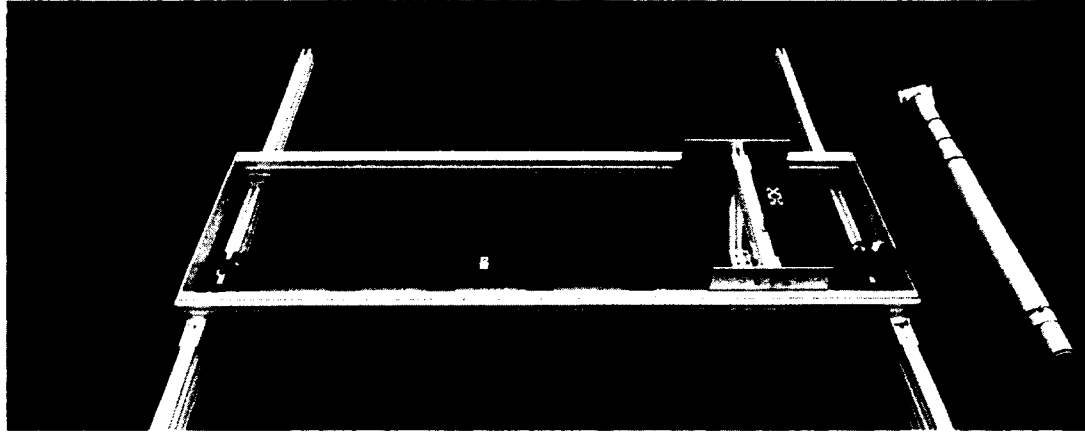


**Figure 70. Version 2 ADV traversing assembly.**

members and implemented Accuride linear roller bearings to reduce the cross stream friction load.

The cross stream support members were positioned on either side of the Bislid and were continuous sections of 1530 extrusion. The ends of each member mounted to linear bearings that rode on the streamwise rail, described below. The Accuride bearing track mounted to the inside face of each support. Two bearings rode in each track and a mounting plate was fabricated that provided a rigid connection to the bearings and improved support to counter rotation caused by cross stream forces, (as was seen in the lift scenario on the previous version). The bolt pattern on the mounting plate enabled joining the frame that supports the submerged sting to the cross stream linear bearings.

The mounting frame for the submerged sting was made of 8020 extrusions and mounting plates and blocks that easily accepted the sting and distributed the load to the cross members and streamwise rail without applying it to the Bislid.

### Cross Stream Positioning

A Velmex Bislid was used to position the ADV in the cross stream direction. The Bislid is a fully assembled drive screw positioning system with a NEMA 23 Vexta type 23T2 stepper motor. It was purchased with a one axis stepper motor driver, two pre-mounted limit switches, Computer Operated



Stepper Motor Operating System (COSMOS) driver software, mounting cleats and a USB to RS-232 adaptor. Velmex sells the slides in several lengths but due to dimensional limitations on the test platform, the slide with 60 inches of travel was chosen. The drive screw pitch is such that the slide moves 0.4 inches per revolution and provides resolution to 0.001 inches with a max speed of 4 inches per second. Velmex sells specially designed cleats for mounting the slide to a surface and in this case 10 cleats were purchased with mounting screws. Much of the vertical load and moment loads from the ADV sting were designed to be supported from other hardware. Loading specifications on the slide include a maximum vertical and horizontal loading of 300 pounds, a cantilever load of 500 in-lb and a holding force of 40 pounds. Since the slide had to be positioned up to 8 diameters downstream, an additional 30 feet of cable was purchased to connect the slide to the driver so that the driver could stay near the on board workstation.

The Bislide was mounted to two sections of 1530 extrusions, one under each line of mounting cleats as shown in Figure 70. The extrusions were spaced appropriately and connected with three blocks along their length, one on each end and one in the middle. The outboard ends of each extrusion were tapped to allow mounting two roller style linear bearings that ride on the rail allowing manual stream wise positioning.

The ADV sting mounted to a support frame, described above, in such a way that the drag loading was transmitted to the Accuride linear bearings, not the Bislide. The stainless steel Accuride bearings worked very well at transmitting all the static and dynamics loads while still sliding with ease. The rails were designed with 1/16 of an inch clearance between the Bislide carriage and the frame member that mounts to the carriage so that some deflections were allowed before the Bislide would have to counteract and support the load. Since stepper motor steps were lost due to excessive friction during the testing at General Sullivan Bridge, these extra details were applied to minimize the loading on the Bislide for the Muskeget Channel testing.

### Stream wise Positioning

The stream wise positioning was performed manually utilizing linear bearings on t-slotted extrusion. There was desire to automate this motion but insufficient time was dedicated to the design so it was not implemented. The supplier, 8020, provides several options for linear motion and positioning. For this design, the rails were made out of 1530 aluminum extrusion mounted to A36 steel angle iron that was bolted to the deck of the platform shown in Figure 71. The traveling distance of 20 feet required that 3 sections of extrusion needed to be joined. This was accomplished with butt joints and specialized fasteners to keep the joints tight. The aluminum extrusions were installed to the angle iron by appropriately positioned holes in the angle with bolts into t-nuts in the extrusion. Once the rail was assembled it was bolted onto the deck by through bolts and studs as necessary. In order to get the instrument 8 diameters downstream, the railing had to be cantilevered off the back of the boat 7 feet. Analysis was performed to ensure the angle iron could support the cantilevered load, but in the event higher loadings were necessary the aft platform has a bar with a hole on either end to run a support cable from the top outside edge of the platform out to the end of the rail. None of the testing for this thesis required the cable connection.



**Figure 71 Stream wise rail and traversing mechanism cantilevered off the stern of the test platform.**

The sled that supported the instrumentation and cross stream positioning equipment was built with linear bearings on each end that mounted to the rail. Due to the distance between each rail, a single cross member would easily bind so the design evolved into three different cross member sections all rigidly connected. Nylon sliding bearings were mounted on the ends of the two outside sections, and roller bearings on the ends of the middle section. The forward cross member had a living hinge installed on each end to connect a 9 foot section of 1515 extrusion that acted as the handle to position the sled.

The downstream distances were calculated from the CAD model and measured once the system was installed. The positions were marked on the rail with a permanent marker and labeled by shroud diameters downstream. System friction was adequate to hold the system in place for much of the testing, but in high velocity flows and for safety, vise grip clamps were used to clamp the 1515 handle to the 1530 rail. Furthermore, bolts were inserted into t-nuts at the aft end of the rail to ensure the system could not slide off the back.

#### ADCP Mount

The ADCP was mounted off the bow of the platform centered along the width and positioned so that the body of the instrument was fully submerged. This location allowed collection of flow data directly upstream of the turbine without disturbing the upstream flow. The primary goals in the design of the instrument mount were to enable rapid deployment and extraction of the instrument while maintaining structural integrity for the security of the instrument.

There have been several methods implemented at the University to mount ADCPs. Clamps around the body of the instrument, and mounting plates that attach to the top of the instrument are common. In this case, the threaded inserts on the top plate of the instrument did not induce confidence for the environment we were going to and without having clamps available a new design was made. The main body of the instrument has a flange on the top to mount a plate with the cable fitting, and the bottom to mount the sensors and processor for the instrument. The bolts connecting the sensor end to the main body of the

instrument were replaced with longer ones so that a fabricated piece of fiberglass angle could be bolted to them. The other face of the fiberglass angle had a tube fitting installed so that it could then be connected to the rest of the mount as shown in Figure 72.

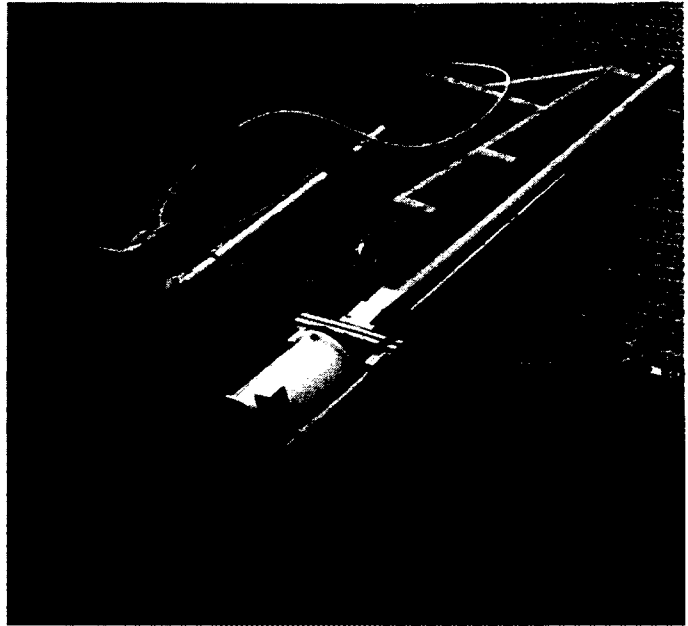


Figure 72. ADCP mount on bow of test platform.

Aluminum tube and blocks which were chosen to mount the ADCP due to the expected ease of linear and

rotary motion. The design scheme of motion was that the instrument would rest on the deck of the platform protruding slightly off the bow. To deploy, the system would rotate from horizontal to vertical, and then the ADCP would slide vertically to the desired depth. The apparatus was designed to be locked in any position with handles mounted on the blocks that clamp the tube. The assembly was mounted to a section of T-slotted extrusion that was then bolted through the deck to the stringers spanning the width of the platform.

Despite consultation with hardware suppliers, this design performed poorly, mainly due the low quality of the clamps. The clamps are sold with hex bolts that are installed two per tube cutout. Upon consultation, these were replaced with handles with the intent to allow a tool-less deployment and extraction. To achieve even a moderate holding force, the clamping bolts required far more torque than the handles could withstand. The handles were then replaced with the bolts provided and even with a hex key it was not possible to achieve a high enough holding force. Since this was discovered at the test site, the field fix was to drill a hole through the block and tube when it was at the desired position and insert a bolt through the block at each fitting.

Another obstacle was the deck connection. Originally, the mount was secured to the deck with U-bolts and a fastening plate to the grated decking. The dynamic loading and the flexibility of the decking allowed too much play in the system so holes were drilled to allow bolting directly to the pontoon stringers.

### Vector Mount

The Vector ADV was positioned off the starboard bow so that the probe was submerged approximately 5 feet. The original mount for this instrument, used at the UNH-CORE test site, utilized a rigidly mounted section of an extruded aluminum NACA 0020 foil. The foil was bolted to two 4x4's that were then bolted to the deck with U-bolts. This system performed fine at the sheltered UNH-CORE test site but was cumbersome and inefficient for instrument removal and deployment. Furthermore, as discussed with the downstream ADV, any flow not directly in line with the foil created lift that caused high loads that were difficult to counteract.

The second design implemented a schedule 40 aluminum pipe of the same length as the original foil. This pipe was connected with speed rail fittings to a piece of plywood that was bolted to the stringers connecting the pontoons. As with the ADCP mount, the pipe fittings were not sufficient to counteract the high and variable loads. The pipe fittings utilize set screws to secure the pipe in place and had to be replaced with bolts. Even with the bolts, the top end of the pipe needed to be strapped back to the deck to provide additional rigidity.

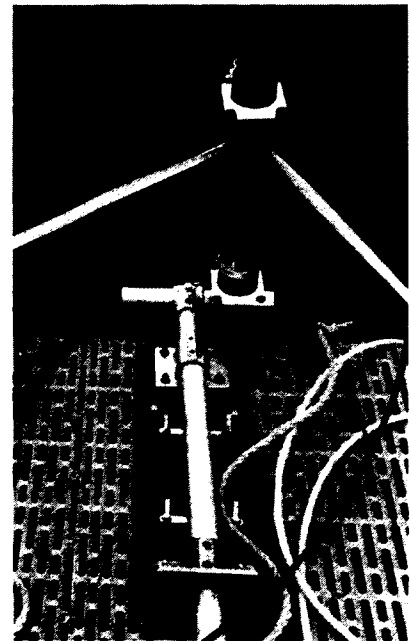


**Figure 73. Vector mounted to bow of test platform.**

The Vector body was mounted to the pipe using two fabricated UHMW clamps. The main part of the clamp bolted to two short sections of 1515 extruded aluminum that were bolted to the top of the pipe. The other piece of the clamp bolted to the first sandwiching the ADV between them. The cable to the probe head ran down,

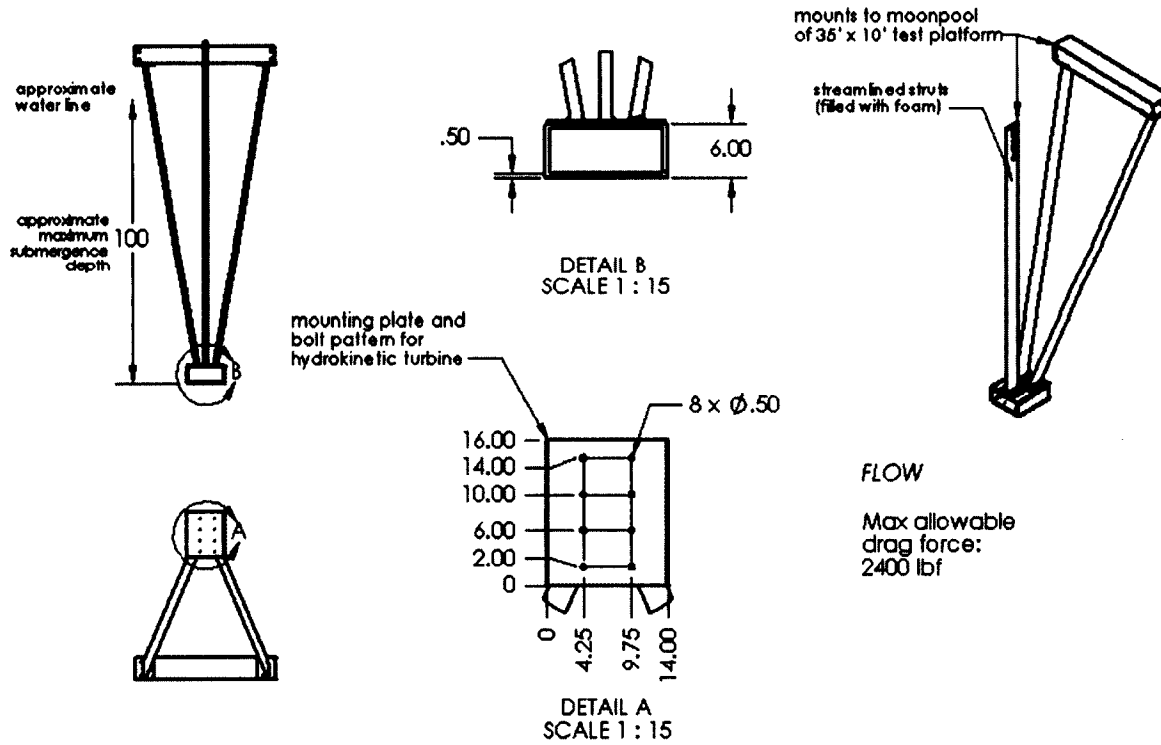


**Figure 74 Vector and other instruments mounted to the bow of the test platform.**

and was zip tied to, the pipe. The probe head was mounted at the bottom of the pipe with a fabricated UHMW clamp.

The original design left the pipe uncovered and it was allowed to slide up and down in the deck fitting so that the instrument could be easily deployed and recovered. After one day of testing it was determined that the asymmetric vortex shedding off the pipe was causing excessive induced motion at the probe. This was an expected outcome, so after the first day of testing a rotating foil was installed over the pipe. Similar to the Vectrino ADV sting, the foil was made by bending sheet aluminum around the pipe, zip tying the trailing edges together and securing it at the top with a shoulder bolt. Prior to bending, a strip was cut out from the sheet that was half the circumference of the pipe and as wide as the shoulder so that a total of 180 degrees of rotation were possible. This drastically reduced the vibrations caused by the vortex shedding but removed the ability to slide and rotate the instrument out of the water adding complexity to instrument deployment and extraction.

**A.4 Selected Test Platform Drawings**



NO PORTION AND COMMERCIAL  
INFORMATION CONTAINED IN THE  
DRAWING IS THE SOLE PROPERTY OF  
UNH. REPRODUCTION IN PART OR AS A WHOLE  
WITHOUT THE WRITTEN PERMISSION OF  
UNH IS PROHIBITED.

5

NEED ANY

APPLICATION

4

USE ON

UNLESS OTHERWISE SPECIFIED:

DIMENSIONS ARE IN INCHES  
TOLERANCES: ± 1/32  
FRACTIONAL ±  
ANGULAR: MACH ± .030 ±  
TWO PLACE DECIMAL ±  
THREE PLACE DECIMAL ±

MATERIAL SPECIFICATION:  
ID: 16A-MCMC-F17:  
MATERIAL:  
AISI 1010 STEEL

NOTE SCALE DRAWING

3

DRAWN  
CHECKED  
ENG APPR.  
MFG APPR.

Matthew Rowell  
mfr36@unh.edu

NAME DATE  
MR 3/15/11  
MW 3/21/11

TITLE:

**UNH - CORE**  
Hydrokinetic Turbine  
Support Structure  
(for Tidal Energy Test Platform v1)

SIZE DWG. NO.

**A**

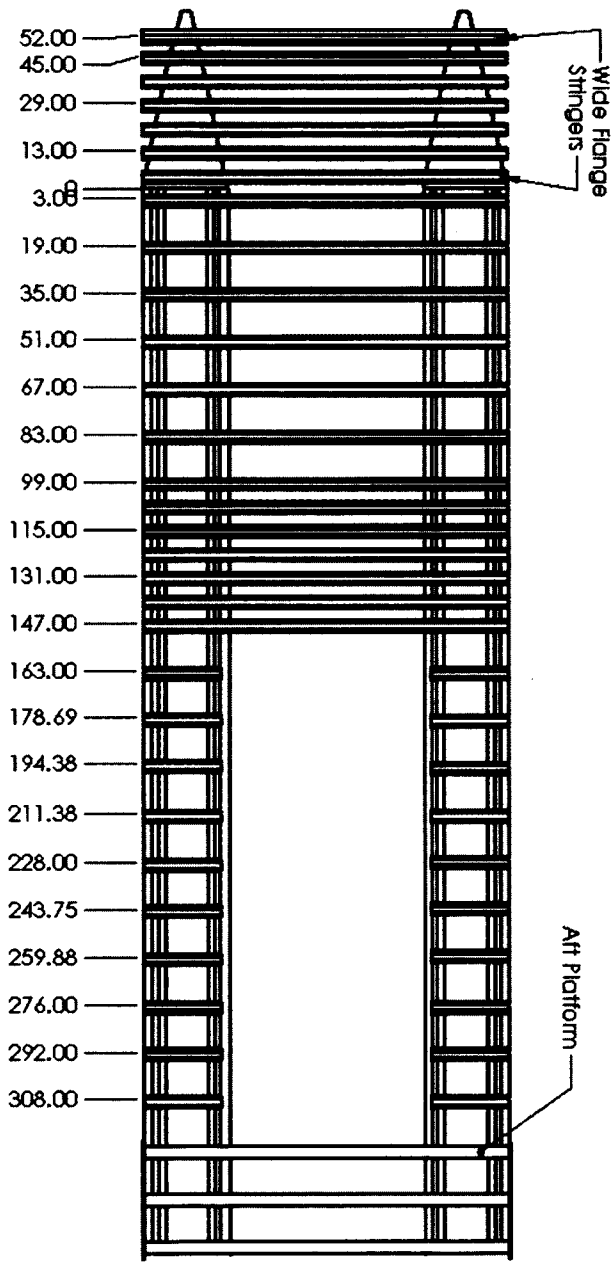
SCALE: 1:48 WEIGHT:

2

REV

SHEET 1 OF 1

1



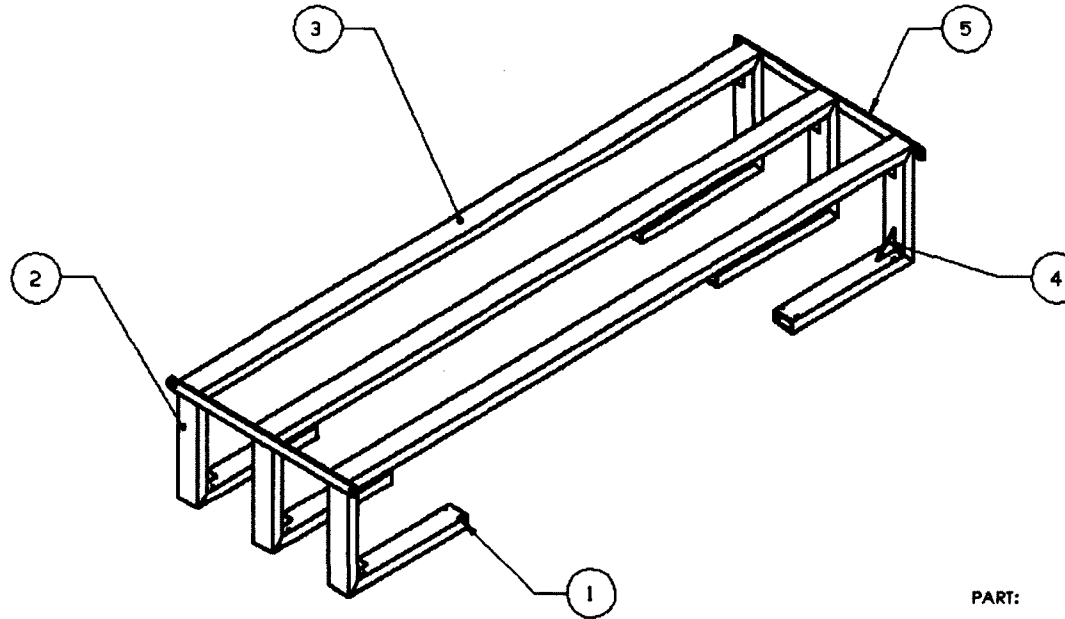
TITLE:  
**Test Platform Stringer Layout**

QTY: Part  
**A**  
 SCALE: 1/4" WEIGHT:  
 2 SHEET 1 OF 1

5 4 3 2 1



ITEM NO.	PART NUMBER	DESCRIPTION	QTY.
1	Bottom Box	2x4x0.25 Al Box 25.5" Long	6
2	Side Box	2x4x0.25 Al Box 20.75" Long	6
3	Top Box	2x4x0.25 Al Box 120" Long	3
4	Gusset	4x4 Triangle 0.25" Thick Al Plate	12
5	Top Brace	40" x 2" x 0.25" Al Plate	2



PART:

## Aft Frame Overview

QTY: PROJECT: REV

**1** UNH - CORE

SCALE: 1:20 WEIGHT: SHEET 1 OF 1

5

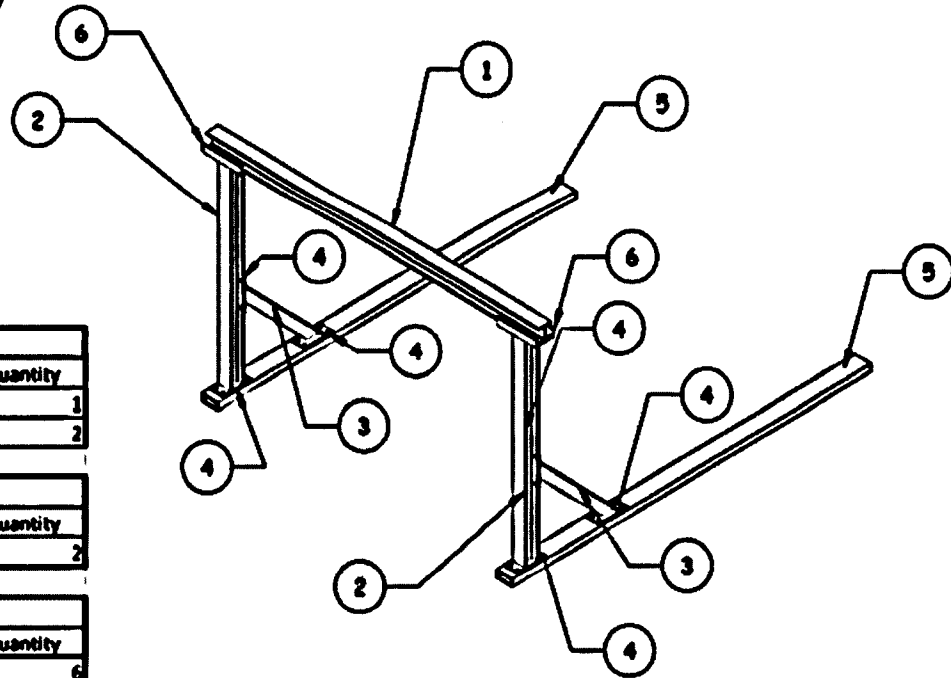
4

3

2

1

Matthew Rowell  
 University of New Hampshire  
 Center for Ocean Renewable Energy  
 (603) 397-7717  
 mfk36@unh.edu



Wide Flange Beams			
Number	Type	Length (in)	Quantity
1	W 4x13	204	1
2	W 4x13	60	2

Structural T's			
Number	Type	Length (in)	Quantity
3	WT 3x6	36	2

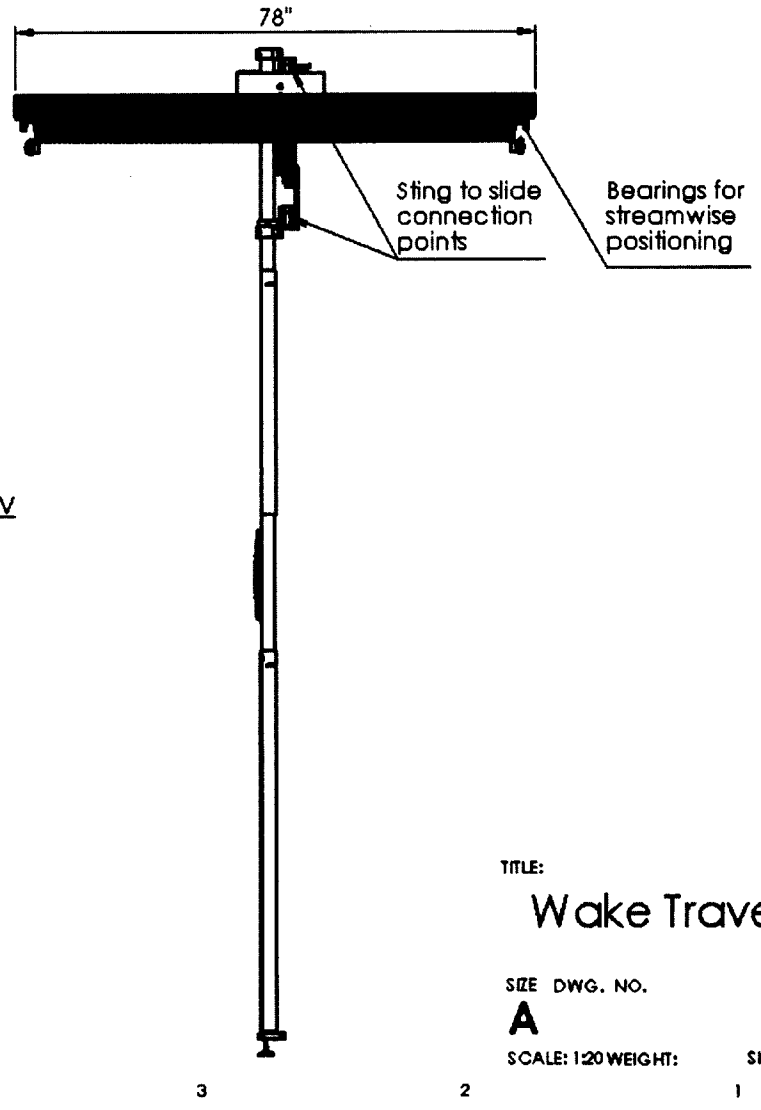
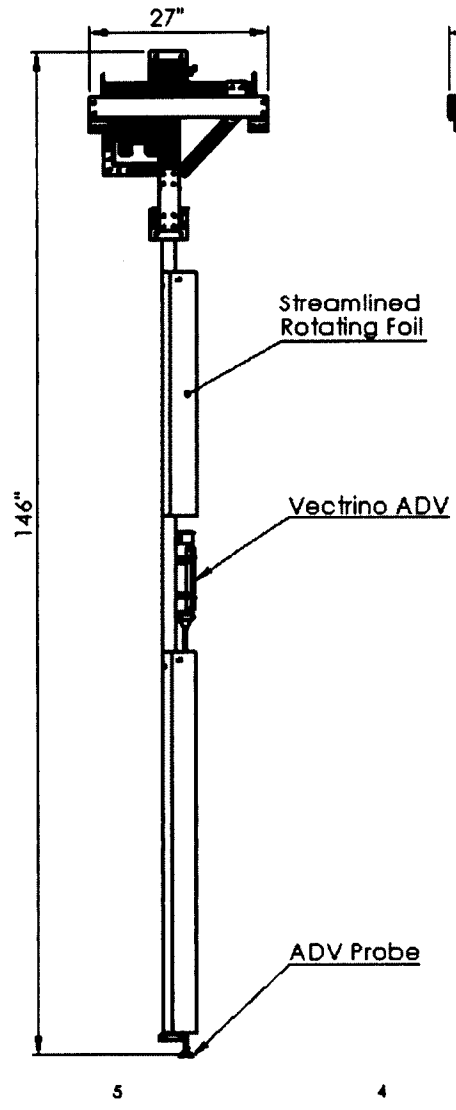
Hot Rolled Flat			
Number	Type	Length (in)	Quantity
4	1/4 x 4	9	6

Rectangular Structural Steel			
Number	Size	Thick (in)	Length (in)
5	Sx2	0.188	112

C-Channel			
Number	Type	Length (in)	Quantity
6	C 6x10.5	12	2

COMMENT:	PART:	
	<b>Hoisting Frame DWG</b>	
SCALE: 1:30 WBOHR:	QTY:	PROJECT:
	1	UNH - CORE
	REV	
	SHEET 1 OF 1	

8 4 3 2 1

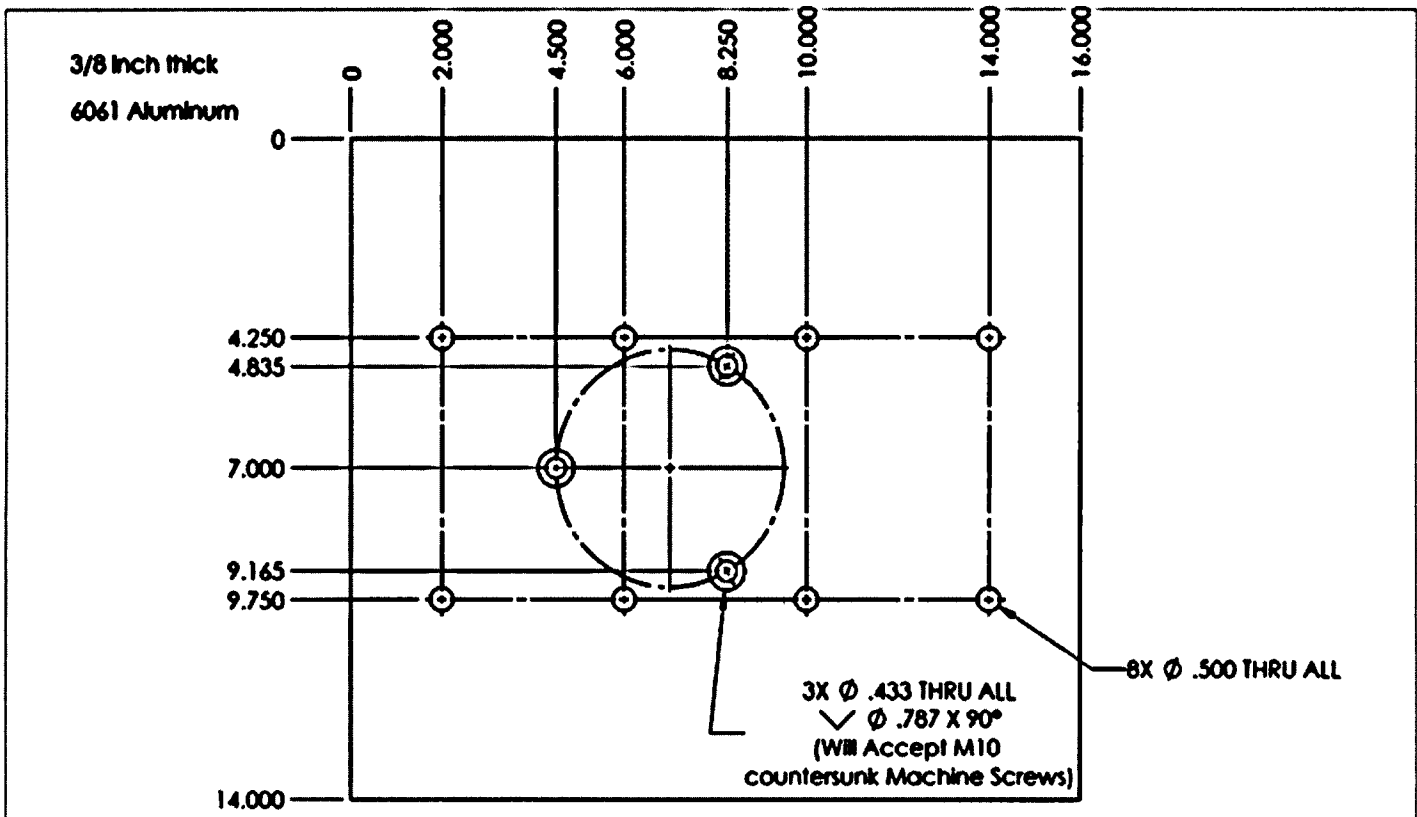


TITLE:  
**Wake Traverse**

SIZE DWG. NO. REV

**A**

SCALE: 1:20 WEIGHT: SHEET 1 OF 1



PROPORTION AND CONSTRUCTION  
 THE INFORMATION CONTAINED IN THIS  
 DRAWING IS THE SOLE PROPERTY OF  
 THE COMPANY AND IS NOT TO BE  
 REPRODUCED OR USED IN ANY MANNER  
 WITHOUT THE WRITTEN PERMISSION OF  
 THE COMPANY UNLESS OTHERWISE  
 PROVIDED

UNLESS OTHERWISE SPECIFIED:		NAME	DATE
DIMENSIONS ARE IN INCHES		DESIGN	
TOLERANCES		CHECKED	
FRAC TIONALS		DWG APPR.	
ANGULARS		APP APPR.	
TWO PLACE DECIMALS		C.A.	
THREE PLACE DECIMALS		CONTR'G	
INFERRED GEOMETRIC TOLERANCES PER AS Y14.5			
FINISH			
DO NOT SCALE DRAWING			

TITLE:	
MEHT_Tow Tank Mating Plate	
SIZE DWG. NO.	REV
A	
SCALE: 1:3	WEIGHT: SHEET 1 OF 1

## A.5 Product and Service Providers

The following suppliers, fabricators and service providers were contracted for work covered in this thesis.

<u>Supplier</u>	<u>Product</u>
Action Automation	Distributor of 80/20 extrusions and hardware.
Air Inc.	Distributor of 80/20 extrusions and hardware.
Amazon	Lab coat and butyl rubber gloves.
Cohen Steel	Raw metal stock, beams and pipes.
Enterprise	Pickup truck rental.
Generator Connection	Generator DC cable.
Granite State Marine	ThruFlow decking for platform.
Jackson Hardware	Marine products for treatment to marine plywood.
Lowe's	Paint, tools, and hardware.
Mast Road Lumber	Marine plywood for platform.
McMaster Carr	Hardware for platform renovations.
Merrimac Sheet Metal	Sheet metal to streamline instrument stings.
New England Marine	Cordage and fenders.
Northern Tool	Turbine deployment and extraction hoist.
PCS Mobile	Toughbook laptop.
Sears	Hand tools.
Velmex	BiSlide positioning system.
<u>Service Provider</u>	<u>Service</u>
CR Environmental	R/V First Light contractor.
Custom Welding	Fabrication of aft platform and clasps and modifications to turbine deployment mechanism.
Fairhaven Shipyard	Platform launch and slippage.
Great Bay Marine	Rental slip for testing at General Sullivan Bridge.
Jocelyn Marine Services	Platform hauling from NH to MA.
Pepperell Cove Marina	Hoisting the platform to and from the pier.
U-Fab Boats	Pontoon boat technical support.

## **Appendix B**

### **B.1 Safety Procedures for Open Water Testing**

The importance of applying safety measures cannot be overstated, and it goes without saying that the primary goal in the open water testing was to keep all personnel unharmed. The safety measures implemented for both rounds of open water testing should be referenced and repeated or improved upon for all future tests.

Each person must dress appropriately for the environment, understanding that it is always colder on the water. Therefore, dressing in layers regardless of the forecast is essential. The work platform should be considered an industrial environment, thereby requiring work boots and gloves. Safety glasses shall be on site and worn for specific tasks that warrant their use. While underway, each person shall wear a type III, or better, personal flotation device, and while offshore, a life raft should be present. The platform shall also be outfitted with an emergency throw ring with at least 150 feet of line. If operating at or near dusk or dawn, appropriate lighting shall be temporarily installed on the platform and each person should have a flashlight at the ready. Chemical lights should be attached to life jackets and cracked, causing them to glow, while operating in dark or low light settings. The work platform is not equipped with life lines so they should be considered in future modifications. Jacklines and harnesses may also be considered for implementation if rough conditions are expected. Since gasoline is used to operate onboard generators, a minimum of a class B fire extinguisher shall be onboard. All equipment needs to be tied down or secured to the deck prior to getting underway. Ratchet straps are useful to strap equipment to the grated decking. Respecting the work environment and staying alert goes a long way to prevent accidents.